Ph.D. Dissertation

Doctoral Program in Chemistry

New Development on Graphene-Contacted Single Molecular Junctions

Qian Zhang

2019/03/28

A DISSERTATION SUBMITTED TO THE DEPARTMENT OF CHEMISTRY AND THE COMMITTEE ON GRADUATE STUDIES OF UNIVERSITY OF LIVERPOOL IN PARTIAL FULFILLMENT OF THE REQUIREMENTS FOR THE DEGREE OF DOCTOR OF PHILOSOPHY

CONTENTS

Acknowledgements

Firstly, I would like to express my sincere appreciation and special thanks to my supervisors, Dr. Li Yang and Prof. Richard J. Nichols, I was fortunate to have my PhD study under their constructive support and guidance throughout the project. This is also extended to my co-supervisor Prof. Cezhou Zhao for his useful advices and supports. I am also grateful to receive the help from the rest of the research group both in XJTLU and UoL, with special mentions going to Mrs. Shuhui. Tao, Mr. Chenguang. Liu, Mr. Chunhui. He, Mr. Ruowei. Yi, Dr. Andrea Vezzoli, Dr. David Costa Milan and Mr. Inco Planje. It has been a wonderful experience to work with them. Thanks to all the staff at the department of chemistry for their help and support in any respect. I would like to thank Dr. Eric Amigues for helping the synthesis of molecules, Mrs. Jianfang Wu and Mrs. Peipei Wang for their technical supports.

Much appreciation also goes to our collaborators, Dr. Yannick J. Dappe and Dr. César González, of SPEC, CEA, CNRS, France for their excellent work on theoretical simulations. I also want to express my gratitude to Dr. Yannick J. Dappe for teaching me lots of theoretical background in physics.

Finally, I would like to thank my parents and sister for their encouragement and support during the study.

List of Abbreviations

MMM	Metal-molecule-metal
STM	Scanning tunnelling microscope
AFM	Atomic force microscope
MCBJs	Mechanically-controllable break junctions
CP-AFM	Conducting-probe atomic force microscopy
SAM	Self-assembled monolayer
ITO	Indium tin oxide
CMOS	Complementary metal-oxide semiconductor
1D	One dimensional
2D	Two dimensional
MOSFETs	Metal-oxide-semiconductor field effect transistors
HOMO	Highest occupied molecular orbital
LUMO	Lowest unoccupied molecular orbital
DL	Donor level
AL	Affinity level
DFT	Density functional theory
CH_3CN	Acetonitrile
DCM	Dichloromethane
KsAc	Potassium thioacetate
DMF	Dimethyl formamide
MeOH	Methanol
NaOMe	Sodium methoxide
NMR	Nuclear magnetic resonance spectroscopy
$CDCl_3$	Deuterated chloroform
DOS	Density of states
JFPs	Junction formation possibilities
BW	Bin width
PDBC	Plateaus-determining bin counts
MJs	Single-molecule junctions
LC	Low conductance
HC	High conductance
CVD	Chemical vapour deposition

List of Figures

List of Tables

Abstract

Molecular electronics holds great promise to realize the ultimate miniaturization of electronic devices and the investigation of charge transport properties through molecules tethered between pairs of electrode contacts is one of the most active areas of contemporary molecular electronics. To date, metallic materials have been widely used as the electrodes to construct molecular junctions, where desired characteristics are outstanding stability, conductivity, and fabricability. However, there is an increasing realization that new single molecule electrical junction functionality can be achieved through the use of non-metallic electrodes. Fundamental studies suggest that carbon based materials have the potential to be valuable alternative electrode materials for molecular electronics in the next generation of nanostructured devices.

In light of the discussion above, we symmetrically investigate the possibility of constructing non-metallic molecular junctions and the corresponding charge transport properties through such junctions by replacing the common gold electrodes with graphene electrodes. We have measured the electrical conductance of a molecular junction based on alkanedithiol/alkanediamine chains sandwiched between a gold and a graphene electrode and compared the effects of anchoring groups in graphene based junctions. We also studied the technical effects of molecule-electrode contacts by comparing methods for capturing and measuring the electrical properties of single molecules in gold−graphene contact gaps. The decay obtained by STM based $I(s)$ and CP-AFM BJ techniques, which is much lower than the one obtained for symmetric gold junctions, is related to the weak coupling at the molecule−graphene interface and the electronic structure of graphene. This asymmetric coupling induces higher conductance for alkanediamine chains than that in the same hybrid metal−graphene molecular junction using thiol anchoring groups. Moreover, we introduce an efficient data sorting algorithm and demonstrate its capacity on real experimental data sets.

As a consequence, we suggest that novel 2D materials could sever as promising electrodes to construct nonsymmetric junctions and the use of appropriate anchoring groups/techniques may lead to a much lower decay constant and more conductive molecular junctions at longer lengths.

1 Chapter 1: Background

1.1 History of molecular electronics

Motivated by practical applications, the advanced silicon technology continues to undergo a rapid development of miniaturizing the electronic devices over the past decades [1]. However, the increasing difficulties and fundamental limitations of the current technology cannot meet the requirements of the further downscaling, the higher performance and stable properties any more. The design rules for silicon-based integrated circuits were proposed by Gordon E. Moore in 1965 and guide the commercial products until about 2008 [2]. Although the commercial 7-nm manufacturing technology has been released by the TSMC Corp., it is impossible to shrink the distance between adjacent components forever due to the quantum tunnelling and heat problems [3]. Based on this, single organic molecules have been considered as a building block of electronic devices and were connected to two metal electrons by building a metal-molecule-metal (MMM) junction [4]. This creative idea is called molecular electronics and it is supposed to lead the dimensions of electronic devices to 1 to 3 nm [5].

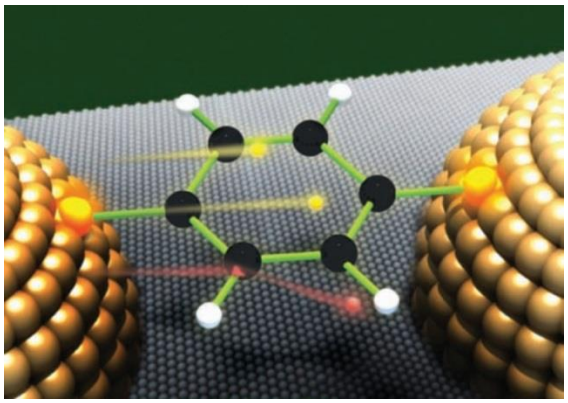

Figure 1. Schematic model of a metal-molecule-metal junction. Reproduced with permission. [4] Copyright 2011, John Wiley and Sons.

Since then, the field of molecular electronics has attracted a great interest amongst researchers as it can not only realize the ultimate miniaturization of electronic devices, but also offers a unique way to understand the charge transport at molecular level. The early studies can be dated back to 1970s. Particularly, Mann and Kuhn reported the

conductivity measurement though organic monolayers and suggested the electron tunnelling though the monolayer of molecules in 1971 [6]. In 1974, Aviram and Rater proposed the first theoretical suggestion of applying single molecule circuit to server as the building block in between of two electrodes [7]. The proposed electrical rectification or diode have been confirmed experimentally nowadays [8-9]. At that time, the most important problem is the way of attaching molecules to electrodes and making defined electrical measurement through such molecular junctions. The first significant work to investigate the charge transport properties through single molecular junction is proposed by Mark Reed and James Tour in 1997 [10]. They studied a gold-sulfur-aryl-sulfur-gold system using a mechanically controllable break junction with benzene-1,4-dithiol molecules self-assembled onto gold electrodes. This study with their later works provide the understanding of how to perform such measurements and how electrons transport through the junction. Since the development of scanning tunnelling microscope (STM) and atomic force microscope (AFM) by IBM in Zurich, it has been clear that these tools are valuable in conductance measurement of single molecules. Then, several techniques have been developed based on STM and AFM, for example, the conducting probe atomic force microscopy (CP-AFM), scanning tunnelling microscopy break junctions (STM BJ) and STM based $I(s)$ techniques in early 2000s [11-13]. The success of these measurements ignited the great interests from the research community and this time was considered as the true beginning of molecular electronics [14].

1.2 Principles of the charge transport

Understanding the theoretical background of metal-molecule-metal junctions plays a crucial role in designing and controlling of the molecular charge transport. For a bare metallic junction (metal-metal), with the thinning of the junction, a single atom wire is formed before the cleavage of the metallic junction and characteristic curves can be observed as a stepwise decrease of the conductance to zero. The conductance of the junction can be modelled by the Landauer expression $G = 2e^2/h\Sigma T_i$ since the size of metallic single-atom contracts is comparable to the Fermi wavelength [1]. Here, G is conductance, T_i is the transmission probabilities for conductance channels. This expression gives contact conductance of 1 G_0 in monovalent metal single-atom contacts (Au, Pt, Ag and Cu) because of the fully opened transmission channel. The conductance quantum, G_0, is equal to $G_0 = 2e^2/h$ and a contact with $G = nG_0$ is composed of n atoms. For a molecular junction (metal-molecule-metal), the measured conductance is observed in a staircase manner at the level of $G < 1\ G_0$ (e.g., the STM-BJ measurement), which indicates the successive forming of molecular junctions [11]. After forming the conductance histograms from the conductance traces, several peaks were then observed at $G = nG_{SMC}$ (n= 1, 2, 3 and so on, SMC=single molecular conductance), where n is the number of molecules connected in the molecular junctions.

Before we continue to discover the charge transport properties of the junction, it is important to clarity some key concepts. In a bulk inorganic metal material, the first important concept to understand the metal-organic interface is the work function Φ_B, defined as the energy needed to pull an electron out of the solid metal and move it in vacuum to an infinite distance away [15]. Another concept is the Fermi level E_F(metal), which describes the collection of electron energy levels, it is placed at the topmost filled (at 0 K) or half-filled (at finite T) energy level within the metal conduction band [15]. In terms of the semiconductor, the Fermi level is statistically located halfway between the valence band and conduction band (Figure 2). The concept of Fermi energy is related to the Fermi level at 0 K. The work function is the energy difference between the E_F and the vacuum level at infinity and the band gap is the energy difference between the bottom of the conduction band and the top of the valence band [15].

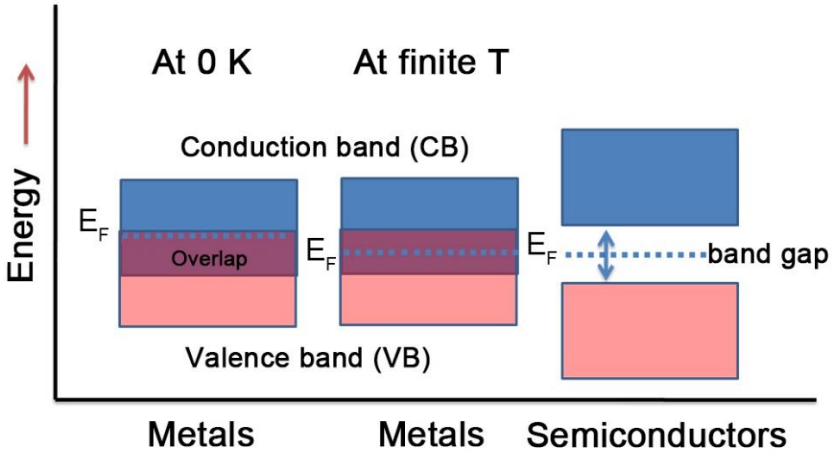

Figure 2. The Fermi level of the metals and semiconductors.

The position of the frontier orbital of a molecule is also an important consideration when it is attached to another molecule or to a metal. The shifted highest occupied molecular orbital (HOMO) is referred to as the donor level (DL) and the shifted lowest unoccupied molecular orbital (LUMO) is referred to as the affinity level (AL) [16]. Both HOMO and LUMO can be broadened by the Gaussian envelopes combined with its vibronic sublevels. The envelopes of the molecules can be broader or narrower depend on its properties, e.g., tetrapyrroles, fullerenes or polyacenes are much narrower [15, 17].

The alignment between the Fermi level of the electrodes and the HOMO/LUMO of the molecules is one of the most important properties of the molecule-electrode interaction [18]. When a single molecule, or an organic monolayer interacts with the electrodes, then two main possible levels of interaction exist: zero interaction and significant interaction. For zero interaction, there is no or negligible interaction and energy alignment between the molecule and electrodes. For significant interaction, there are three different regimes according to the coupling strength: the weak coupling, the intermediate coupling and the strong coupling. To better illustrate the coupling strength, the coupling parameter (Γ) and the addition energy (U) are induced which are defined as the broadening of the molecular energy level and the difference between the energy to take one electron from the HOMO and the energy obtained by injecting one electron to the LUMO respectively [19].

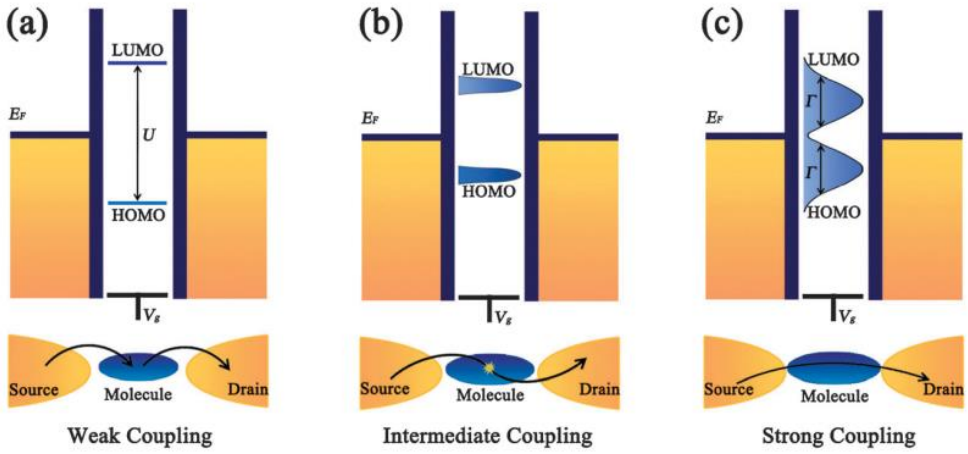

Figure 3. The schematic diagram of the charge transport mechanisms with different coupling strength of molecules and electrodes. (a) In the weak coupling, the electron transport follows a two-step process. (b) In the intermediate coupling, the electron transport through the molecules interacting with the electrons on the molecules. (c) In the strong coupling, the electron transport from the source to the drain by a one-step process. Reproduced from Ref. 19 with permission from The Royal Society of Chemistry.

For electrons transfer in the weak coupling regime ($\Gamma \leq U$), the wavefunctions of the HOMO and LUMO have negligible mixing with the electronic states of electrodes. It follows a two-step process which the electrons firstly hop from one electrode to the middle molecule at an energy level preferred position and then hop to another electrode (Figure 3a). In the case of the intermediate coupling, the transferred electrons can be affected by the electrons on the molecules, for example, when there is an unpaired electron on the molecules, the spin state can be reversed by the electrons passing through and the new transport channels can open as well. In the strong coupling regime ($\Gamma \geq U$), the wavefunctions of the molecules have a significant overlap with the electronic states of electrodes, which leads to an efficient transport of the electrons. The electron could transfer almost freely across the interface by a one-step coherent process [19].

Based on the charge transport mechanism discussed above, it is possible to quantify the current flow though molecules by the appropriate theoretical language [20]. Quantum-mechanical tunnelling is a very important concept and can be the dominant process in vacuum or in short molecular thin films (working length shorter than 2nm). Tunnelling implies an energy barrier, of width d (nm), and the quantum-mechanical wave function. The wave function amplitude rapidly approaches to zero as the distance increase. It can also be considered as a wave coming from one side to another side, partially reflected to the original side and partially transmitted to the other side. Elastic (ballistic) transport happens if the electron in a materials medium does not interact with phonons or excitons, while inelastic transfer (scattering) occurs if the electron interacts with phonons or excisions [15]. Coherent transport happens if the phase of the wave is conserved, while for incoherent hopping electrons spend time localized in intermediate state. To a first approximation, the transport through short molecules connected between electrodes is generally by coherent tunnelling [21]. It is worth noting that coherent tunnelling is not effective over longer distance (> 2.5 nm). Electron transport is usually more complex for such longer distances, for example, by incoherent tunnelling or ohmic hopping conduction [22]. Such coherent tunnelling regime can be described by the single-channel Landauer formula:

$$G = I/V = 2e^2/\hbar\, T_L T_R T_{mol},$$

where I is the current through the molecular junction, V is the applied bias, e is the elementary charge, $\hbar$ is the plank's constant and $T_L T_R T_{mol}$ are transmission coefficients of electrons through the left contact, the right contact and the molecule, respectively. The quantum of the conductance is the maximum conductance per conductance channel, with the $G_o = 2e^2/h = 77480.9$ nS (nanoSiemens). If we treat G_o as the prefactor and combine with the transmission coefficients of the contacts, then the $G_{contact} = G_o T_L T_R$. The transmission efficiency of the molecule, T_{mol} can be expressed as $T_{mol} = \exp(-\beta_n N)$ approximately for a coherent, non-resonant tunnelling regime, where β_n is the tunneling decay constant and the N is the length of the molecule. The decay constant β_n can be given by $\beta_n = 2\frac{\sqrt{2m^*\alpha(\phi-(eV/2))}}{\hbar^2}$, simplified as $\beta_n = 2d_0\sqrt{(2m\phi)/\hbar}$ [23], where m, v, $\hbar$

and a are the effective electron mass ($m^* = 0.16m_0$), the applied bias and the reduced Planck constant and the junction asymmetric parameter ($\alpha = 1$ for symmetric coupling) respectively [21]. ϕ is the barrier height between the Fermi level of the electrode and the LUMO and HOMO levels of the molecules ($\phi = (E_F - E_{LUMO})$ or $(E_{HOMO} - E_F)$). For non-resonant (tunnelling transport), the Fermi level of the electrodes is located in between of the HOMO and LUMO gap and the conductance is influenced by both the interfacial coupling strength and the energy level offset. While for the resonant transport, the Fermi levels of the electrodes are resonant with the molecular energy levels and the conductance only depends on the coupling strength during the contacts. From the above equations, the weak coupling at the interface results in a decrease in $T_{contacts}$ and therefore reduce the junction conductance. If there are physical contacts (no chemical bonding) and T_{mol} is sufficiently high, then $T_{contacts}$ will dominate the charge transport. It is thus important to both consider the coupling strength and energy level alignments at the interface when investigating the charge transport efficiency between the junctions.

It is now possible to investigate the theoretical electrical properties of single molecule junction by a combination of density functional theory (DFT) and a Keldysh-Green formalism for nonequilibrium systems. Despite the limitations of standard density functional theory (DFT), for example, the difficulties in accurately calculating the level alignment due to the HOMO-LUMO gap underestimation and the oversimplified model of the real molecule-electrode geometry [20], the first-principles theoretical methods have been developed as the important approach in combination with experiments to understand and study the mechanisms of the charge transport through the molecular junctions.

1.3 Techniques for measuring single molecule conductance

Constructing reliable break junctions provides an effective platform for fabricating and measuring the electrical properties of the nanogap junction with adjustable design of the molecule and electrode systems. There are several techniques to form such junctions which can be categorized into mechanically formed junctions, in situ break junctions based on STM and AFM and other large scale/multi molecular arrays (e.g., lithography and EGaIn techniques) [24-25]. To date, the most widely used techniques for probing the electrical properties of single molecule junctions include the MCBJs [10], STM BJ, the *I*(*s*) technique [11,13] and CP-AFM [12,26] which are described in detail below.

1.3.1 The mechanically-controllable break junctions (MCBJs)

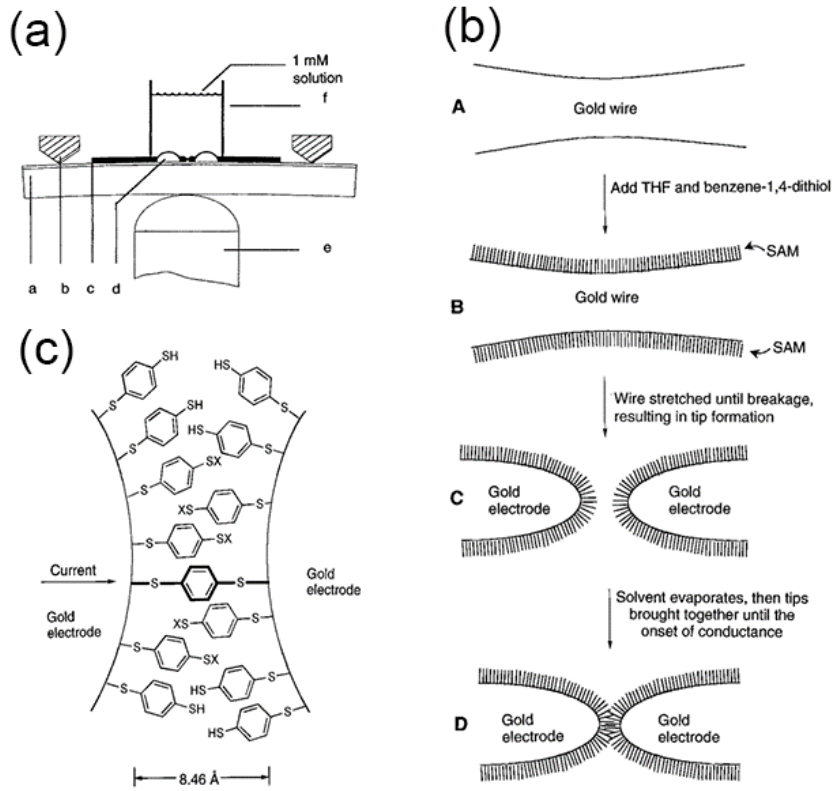

Figure 4. (a) A schematic of the MCBJs junction. (b) The measurement process of the MCBJs. (c) An illustration of a benezene-1,4-dithiolate SAM formed on gold electrodes and the configuration of the molecular junction. Reproduced with permission. [10] Copyright 1997, AAAS.

The MCBJs method was firstly demonstrated by Reed et al. in 1997 as shown in Figure 4 [10]. Benzene-1,4-dithiol molecules were coated onto the gold electrode with a self-assembled monolayer (SAM), the gold-sulfur-aryl-sulfur-gold system was then formed, allowing for the investigation of the electrical properties within the junction. In the experiment, a gold wire was fractured by bending in the molecular solution, then an adjustable tunnelling gap can be formed with a SAM in place. After the evaporation of solvent, the gold contacts were brought together until the onset of a current flow. The measurement can be achieved when a small number or ideally one molecule bridges the gap, then the current can be recorded with the bias voltage applied. As the cleavage of wire is controlled mechanically, the contact size can be adjusted continuously. Lithography technique is another useful way to generate MCBJs which proposed by Kergueris et al. in 1999 [27]. The 2,2':5'2''-terthiophene-5,5''-dithiol molecular bridge was formed in between of the gold electrode pairs in their study.

The advantage of the MCBJs technique lies on the high resolution and controllable forces to the junction. However, MCBJs is a dynamic break junction process, which may potentially cause issues in the stability of molecular junctions. In addition, the definitive proof of how many molecules included, the exact shape and the configuration of junctions are hardly known, although the theoretical modelling may help here.

1.3.2 The scanning tunnelling microscopy break junctions (STM BJ) technique

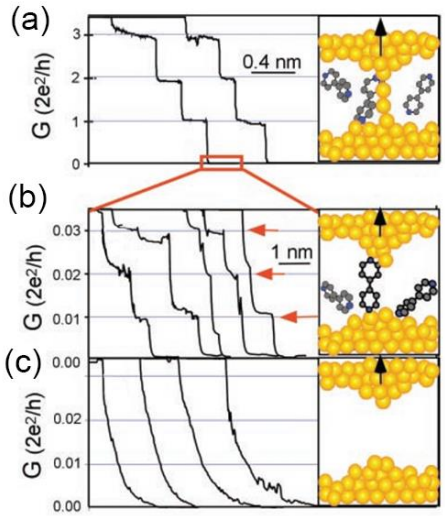

Figure 5. The procedure of forming STM break junctions with the conductance traces shown. (a) The gold tip is pulled away from the substrate and conductance of a contact between two gold electrodes revealed quantum steps near multiples of the conductance quantum ($1G_0$, $2G_0$, $3G_0$ and so on). (b) After the breakage of metallic contact in (a), a new series of conductance steps appear owing to the formation of the stable molecular junction between two electrodes. (c) No such steps or peaks in (b) were observed without the formation of molecular junctions. Reproduced with permission. [11] Copyright 2003, AAAS.

Since the development of the STM in 1980s by the IBM Corp. in Zurich, it has been considered as the useful tools to construct MMM junctions and measure the conductance of tens to single molecules. The STM-BJ method was introduced by Xu et al. in 2003 as shown in Figure 5 [11]. In this method, more than thousands of metal-molecule-metal junctions are formed repeatedly and quickly by moving the STM tip into and out of contact with the metal substrate, with a low-coverage monolayer coated on it. The molecular target can either be pre-adsorbed onto the metal substrate or be dissolved in a solution (e.g., the mesitylene or toluene). During the process, single or a collection of molecules can bridge the gap between the tip and substrate, meanwhile, the current signals as a function of the tip moving distance are recorded simultaneously at a preset bias. Because of the inevitable fluctuations in the experimental data, a robust statistical analysis of the conductance data such as through the recording of histograms is generally required to provide the evidence of the successful formation of molecular junctions [4].

1.3.3 The scanning tunnelling microscopy *I*(*s*) technique

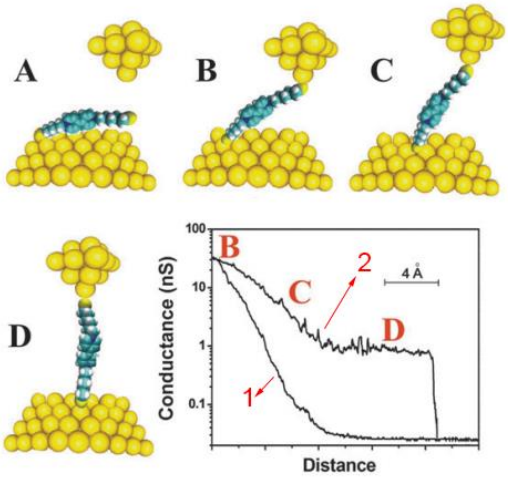

Figure 6. Schematic diagram of the *I*(*s*) method. Molecules with dithiol anchoring group were linked between two electrodes during the STM tip was brought close to the Au substrate. The conductance and distance curves recorded during this procedure showed two kinds of typical curves. Curve 1 is the baseline for a bare Au substrate without any molecular bridge formed while curve 2 indicates the *I*(*s*) curve recorded corresponding to the procedures of B, C and D. Reproduced from Ref. 28 with permission from The Royal Society of Chemistry.

The *I*(*s*) technique is another method based on the STM which introduced by Haiss et al. in 2003. Since the molecular junctions can be formed without the need of making direct metallic contact between the STM tip and the substrate [13]. This technique is also referred as the "non-contact" implementation of the BJ method [28]. By adjusting the set-point conditions, the STM tip is brought close to the Au substrate but avoiding the physical contact (as shown in Figure 6-A, B). Then, the gold tip is retracted to its original position at a pre-set moving speed until the molecular junction is cleaved (as shown in Figure 6-C, D) while collecting the current-distance (*I(s)*) traces (*I* = current, *s* = relative tip-sample distance). Two typical sets of *I(s)* curves are normally observed, one is a fast exponential decay of direct tunnelling between the tip and a metal substrate (marked as 1 in Figure 6), another one is a characteristic current plateau related to conduction through molecular junction (marked as 2 in Figure 6). Many of these *I(s)* curves are then analysed statistically to produce a conductance histogram. Since there is no contact between the STM tip and the substrate, the STM tip does not damage the substrate and vice versa.

It is also worth to mention the STM "Touch-to-Contact" method described by Martin et al., in which the STM tip is positioned just in contact with the top of the molecular monolayer film. The gesture of the STM tip is at the middle stage of the STM-BJ and the *I*(*s*) technique by controlling the STM set-point parameter to an absolute tip-substrate separation [29]. The STM "Touch-to-Contact" avoids both incursion of the tip into the molecular monolayer film or a gap between the top of the monolayer and the STM tip.

1.3.4 The conducting-probe atomic force microscope (CP-AFM) technique

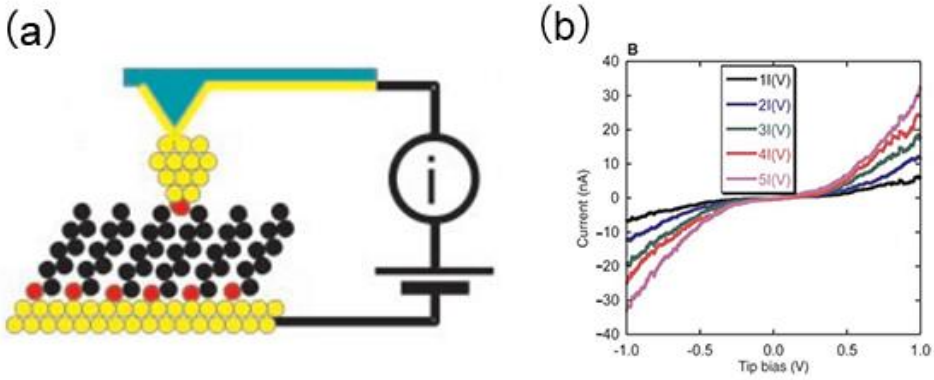

Figure 7. (a) The experimental illustration of the CP-AFM technique. Sulfur atoms (red dots) of octanedithiol molecules were bonded to gold atoms (yellow dots) of the gold tip and substrate. (b) *I(V)* curves measured by the apparatus shown in (a). The five curves are representative of distinct family, *NI(V)*, that are integer multiples of fundamental curves, *I(V)* (*N*= 1,2,3,4 and 5). Reproduced with permission. [12] Copyright 2001, AAAS.

Atomic force microscopy (AFM) is another very useful tool to probe the structural characterization of the sample and construct the AFM tip-molecule-bottom sample junctions. Cui et al. reported a reliable conducting-probe atomic force microscope (CP-AFM) method to measure the current-voltage *I(V)* characteristics of this MMM junctions in 2001 as shown in Figure 7 [12]. A metal-coated AFM tip, acts as the top electrode, is brought into contact with the bottom gold electrode with the surface covered by a low concentration of the dithiol SAM. The AFM feedback loop was used to control the forces loaded onto the surface, while current−voltage (*I*−*V*) relationship of the molecular layer sandwiched between the tip and surface is recorded. Normally,

such junctions may contain tens or hundreds of molecules ascribed to the relatively large area of the tip geometry, the contacting force and the deformation properties of the SAMs. By introducing the gold nanoparticles, CP-AFM may also be used to investigate the electrical properties of the single molecule junctions. In the method developed by Cui and Lindsay [30-31], the gold nanoparticles are adsorbed on-top of SAMs of monothiols, which electrically wire the nanoparticle to the surface. Touching the top of such gold nanoparticles with the CP-AFM tip then enables $I-V$ characteristics of the molecular junction to be recorded.

All of these techniques rely on the capability of capturing single or small groups of molecules while recording the electrical signals. Despite the similar basis of forming molecular junctions, measurements with the STM BJ technique tend to form "rougher" contacts because of the gold contact breaking, while the $I(s)$ technique can be applied to flat surface areas if desired. In this respect, these techniques can be seen as complementary, and the application of both to the same molecular system could be expected to broaden the view of the molecular junction properties and the spread of favoured junction conductance values. CP-AFM, on the other hand, conveys the advantage of being able to record the force and current signals simultaneously offering the possibility to correlate electrical and mechanical properties of junctions [32-33]. However, a potential disadvantage can arise with the use of AFM tips with higher radii of curvature, where there could be ambiguity about forming truly single-molecule junctions when CP-AFM is used to form break junctions. In any case, measurements of molecular conductance with several different techniques should be seen as advantageous [33].

1.4 The analysis of the charge transport data

1.4.1 Typical *I-V* and *I-s* curves

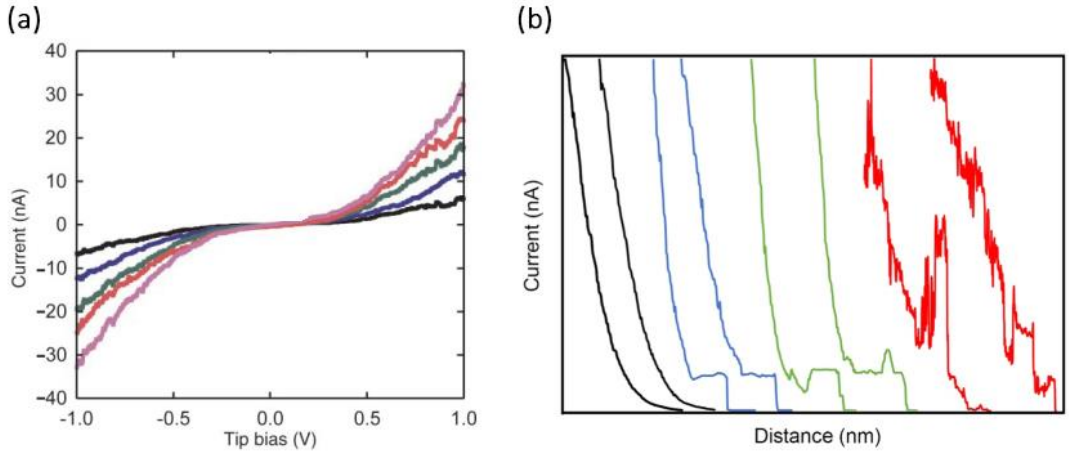

Figure 8. (a) Typical *I-V* curves and (b) *I-s* Curves. Reproduced with permission. [12] Copyright 2001, AAAS.

For all the techniques used to explore the electrical properties, it generally produces large variability in any given conductance determination due to the factors influencing the stability of the junction, for example, the surface binding geometry between the molecule and contact, the stochastic nature of the junction formation/breaking process, the external environment and the noise [34]. It is then necessary to repeatedly record many traces and then statistically represent this data recorded for the making and breaking of many molecular junctions.

Two typical electrical signals are collected during the measuring process, they are *I-V* (*I*=current, *V*=tip bias) curves and *I-s* (*I*=current, *s*=distance) curves. *I-V* curves are commonly used in the CP-AFM study, the conductance information is obtained from the slope of the current and bias relationship. There are five distinct *I-V* curves are observed in Figure 8a, corresponding to multiples of a fundamental curve. Figure 8b shows the *I-s* curves collected in the STM based *I*(*s*) experiments, such curves can be further categorised into pure decay (black), ideal plateau-featuring curves (blue), plateaus with noise spikes (green) and highly noisy curves (red). The preferred traces, taken as characteristic of stable molecular junction formation, are those featuring with the plateaus (blue), which signify defined formation of molecular junctions followed by their breaking.

1.4.2 Data analysis methods

In the simplest case, electrical data can be used to plot the 1D conductance histograms to represent the most probable conductance value of the junction. Such a statistical analysis has been underpinning for achieving reliable electrical data for single molecule junctions. There are then two broad approaches which can be applied to perform the data analysis, each of them has its advantages and disadvantages. The first approach is to simply use all the raw data without any treatment and the advantage here is that there is no preselection of the data. However, such analysis may include a lot of traces where no or poorly formed junctions are present. It can also be problematic to generate the conductance histograms if the junction formation possibilities (JFPs) are low. As an alternative to using a non-selective approach, the second approach is to try to select out traces where there is clear evidence for stable molecular junction formation [35]. The advantage for such approach lies on the removing of irrelevant traces to the junction formation and the molecular data is retained. The disadvantage is possible to the conscious or unconscious bias introduced during the data selection.

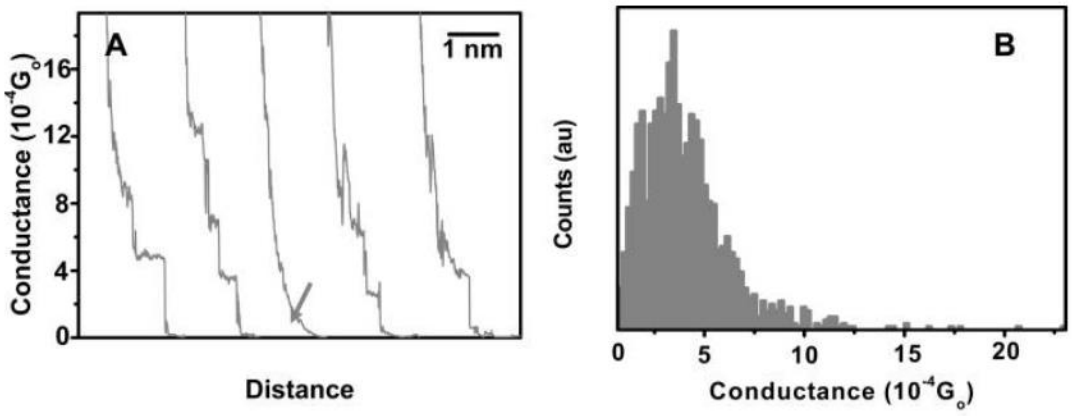

Figure 9. (a) The representative conductance traces of Au-1,6-hexanedithiol-Au junctions, the arrow indicates conductance traces which show only tunneling current without the formation of the molecular junctions, the rest are traces featuring steps in conductance. (b) The corresponding conductance histogram of the trances by the last step analysis. Reproduced with permission. [36] Copyright 2006, American Chemical Society.

Early work used hand-selected data with rational selection criteria to reduce any bias introduced during the process. Jang et al. introduced a last-step analysis (LSA), motivated by the fact that the last conductance drop is only related to the breakage of the last molecular bridge. In this method, only traces featuring a rapid conductance drop in the last step are treated as the valuable data and used to construct the conductance histograms [36]. Gonzalez et al. presented an alternative method using all the conductance traces without the background traces (arrow trace in Figure 9a) to construct the conductance histograms. They extract the background traces which fail to show any information of the junction formation and use all the rest of the traces irrespective of their shape [37].

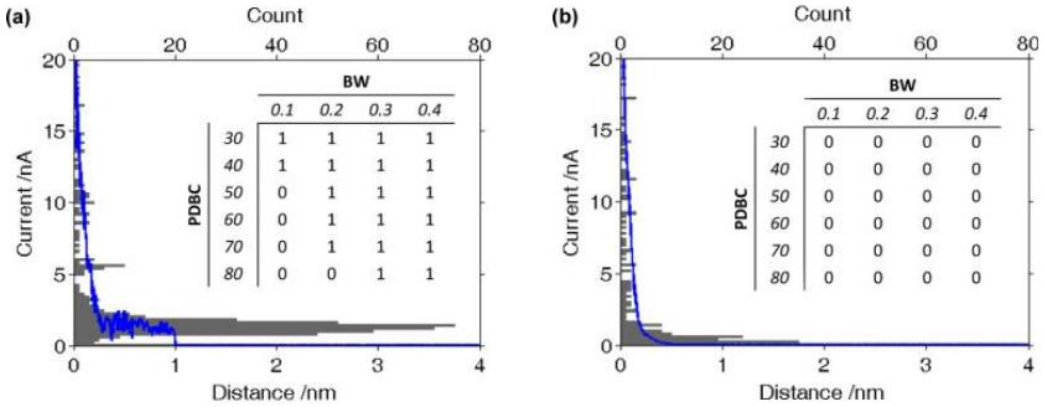

Figure 10. Single trace histograms of the plateau featured curve (a) and the pure decay curve. The inset table is the data sorting parameters to separate the plateau featured curves. Reproduced with permission from ref. 38. Copyright 2015, American Chemical Society.
Direct link: https://pubs.acs.org/doi/abs/10.1021/jacs.5b05693.

More recently, the automatic data sorting algorithms have been developed to analyse the conductance traces in single molecule junctions. The Albrecht group introduced two algorithms based on MATLAB programs to separate the plateau featured traces from the dataset [38-39]. In the first case for each exported current-distance trace the current signal is divided into many bins with a selected bin width (BW). Each bin will have a value for the number of plateaus-determining bin counts (PDBC). The combination of the BW and PDBC defines the sensitivity of the selection process and indicates the traces containing (1) or not containing (0) a plateau as shown in Figure 10. Bins containing plateaus will exhibit a higher bin count, while the bin counts for a clean exponential curve are much lower. With a sorting algorithm which recognizes plateau-containing traces based on the bin counts, the traces containing plateau (molecular) features can be separated from both exponential traces and those primarily related to experimental noise [38]. Algorithms have been also applied here to remove noisy traces and traces exhibiting unusual current-distance decay characteristics. This method has been successfully used for the analysis of very large number of traces (up to 100 000) of octanedithiol molecular junctions with gold electrodes.

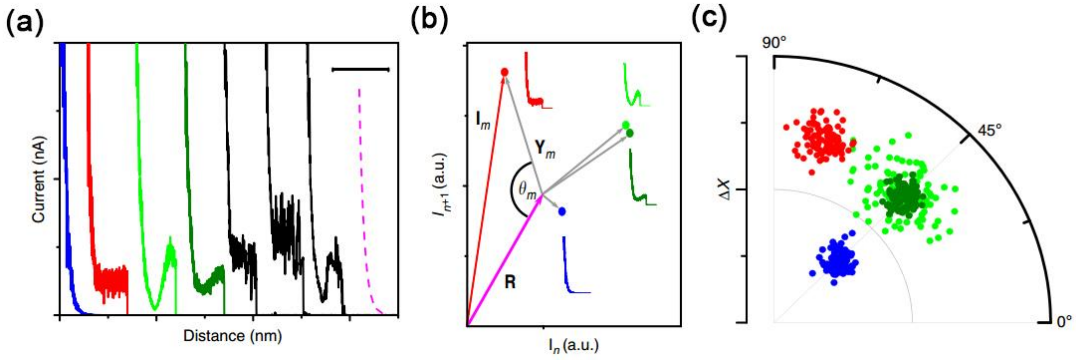

Figure 11. (a) Typical *I*(*s*) curves featuring a with plateau, without plateau and non-linear plateau with low and high amplitude. (b) The representation of the vector transformation of the curves in (a). (c) The representation of the vector-based traces in cylindrical coordinates. The red, blue and green clusters indicate the different conductance groups separated by the vector-based classification method. Reproduced with permission. [39], Open Access, Copyright 2016, Springer Nature.

The second algorithm is a vector-based classification process that is used to identify and extract the conductance traces into different groups or clusters [39]. This method is inspired by the widespread applications of vector-based classification method in genetics, robotics and neuroscience [40-41]. The vector characteristic of the experimental *I*(*s*) traces (X_m, m is the number of data sets) are compared to a standard pure exponential decay reference trace (R). Each trace is defined in terms of three parameters, namely, the Euclidean distance $|\Delta X_m|$, the angle θ_m, and the reduced Hamming distance $h_{r,m}$ (see the detailed algorithm in Ref. 39). These parameter are then used to represent the data in a three-dimensional plot (ΔX_m, θ_m, $h_{r,m}$) in cylindrical coordinates. The data is then clustered into a chosen number of groups, with clusters possessing common features between traces, for example shape or plateau height.

The unsupervised classification of single molecule charge transport data is suited for very large data sets and does not make a priori assumptions with respect to features of the current-distance traces, such as their shape or magnitude of any plateau features. A particularly attractive feature of this method is the ability to recognize sub-populations in the data and garner statistical information for their occurrence.

1.5 The previous studied metal/molecule/metal systems

Metal-molecule-metal (MMM) junctions are formed by trapping typically organic or organo-metallic compounds between of two electrodes, thereby providing a platform for studying the electrical properties of molecules. Selected previous studies of MMM junctions for a variety of molecular compounds and electrodes are shown as table 1.

Table 1. Previous studied metal/molecule/metal systems.

Molecules	Anchoring group	Substrate	Tip	Method	Reference
Benzene-1,4-dithiol	-SH	Gold	Gold	MCBJs	Reed *et al.*, 1997 [14]
4,4-bipyridine	$-NC_5H_4$	Gold	Gold	MCBJs	Quek, 2009 [42]
N-alkanedithiols 4,4-bipyridine	-SH $-NC_5H_4$	Gold	Gold	STM-BJs	Xu and Tao, 2003 [11]
Oligo(phenylene ethynylene)	-SAr	Gold	Gold	STM-BJs	Xiao *et al.*, 2005 [43]
Dicarboxylic-acid butane Octanedithiol Diamine butane	-COOH -SH $-NH_2$	Gold	Gold	STM-BJs	Chen *et al.*, 2006 [44]
1,4-diaminobeneze	$-NH_2$	Gold	Gold	STM-BJs	Quinn, 2007 [45]
Dimethyl phosphine, methyl sulfides terminated alkanes	$-PMe_2$ -SMe	Gold	Gold	STM-BJs	Park, 2007 [47]
α,ω-bis(acetylthio) terthiophene α,ω-bis(acetylseleno) terthiophene	-TS -TSe	Gold	Gold	STM-BJs	Yasuda *et al.*, 2006 [47]
6-[1′-(6-mercapto-hexyl)-[4,4′] bipyridinium]-hexane-1-thiol iodide	-SH	Gold	Gold	*I(s)*	Haiss *et al.*, 2003 [13]
Thiol-terminated ether	-SH	Gold	Gold	*I(s)*	Scullion *et al.*, 2011[34]
1,8-octanedithiol	-SH	Gold	Gold	CP-AFM	Cui, 2001 [12]
N-alkanedithiols	-SH	Gold	Gold	CP-AFM	Morita, 2007 [30]
1,4-benzenediamine	$-NH_2$	Platinum	Platinum	STM-BJs	Kiguchi, 2008 [48]
Carboxylic acid	-COOH	Silver/ Copper	Silver/ Copper	STM-BJs	Peng *et al.*, 2012 [49]
3-(pyridine-4-yl) propionic acid Pophyrin	-COOH $-NC_5H_4$	ITO	Gold	STM-BJs	Battacharyya, 2011 [50]

From the table above, STM-BJs and its analogous *I(s)* technique, are the most widely used techniques to investigate the conductance of single molecular junctions. CP-AFM and MCBJs techniques are also very powerful platform for such study with the specific advantages of the controllable forces loaded on the surface and the precisely mechanical driven. Gold has been extensively used to construct molecular junctions, while other metallic materials such as Ag, Cu and Pt were also reported. For anchoring groups of the molecules, thiol (-SH), amine ($-NH_2$) and carboxylic acid (-COOH) are the most commonly studied head groups, other functional groups have also been selected as the binding component, such as, isocyanide (-NC), dimethyl phosphines (PMe_2), methyl sulfides (SMe) and so on [48].

So far, gold-alkanedithiol/diamine-gold molecular junctions are very well studied due to the solid chemical bonding between the dithiol/diamine anchoring groups and the gold electrodes. The contact resistance to gold of them varies in the order of amine ($-NH_2$) > thiolate ($-SH$), attributed to different electronic coupling efficiencies between the molecule and electrodes. Also, the bonding patterns of them are different: thiolate forms a strong covalent bond with gold (Au-S), while the binding for gold and amine-terminated alkane is significantly weaker (Au-NH_2) since the bonding regime between the Au and NH_2 is a simple delocalization of the lone pair of electrons from the nitrogen to gold atoms and the bond is relatively insensitive to the local structure. [51]. More recently, studies from the Venkataraman group strongly suggested that the gold-sulfur bond in SAMs prepared from the solution deposition of dithiol is not predominate by the chemisorbed character and the hydrogen is retained. The chemisorbed bonds are consistently formed in the solution environment (liquid cell) in STM-BJ measurement. Such findings open the new mind of understanding the interaction between molecules and electrodes [143].

Many literature studies have been performed to measure the single-molecule conductance and investigate the decay constant of gold−alkanedithiol−gold systems. For example, Marita and Lindsay measured the conductance of 1,n-alkanedithiol (n = 8, 10, 12) compounds using CP-AFM, with conductance values of 16.1 ± 1, 1.37 ± 0.35, and 0.35 ± 0.04 nS found, respectively [30]. Based on STM-BJ measurements, Li et al.

and Tao et al. have reported conductance values for 1,n-alkanedithiols of 19.4 (n = 8) and 1.6 nS (n = 10) [11, 52]. They also found the resistance of the N-alkanedithiol increases exponentially with the chain length with a decay constant (β_n) of 1.0 ± 0.05. Haiss et al. obtained a value of 1 nS by the analogous STM technique for gold-octanedithiol-gold junctions [53]. It is clear that apparent discrepancies between conductance values have been reported between different laboratories even using the similar techniques. This was later rationalized as arising from different ways in which these alkanedithiols can bind to the gold contacts through the thiol end groups, with the differing techniques favouring different anchoring configurations [28,52,54,55].

Gold-alkanediamine-gold systems are also well studied until now. Chen et al. measured the conductance of N-alkanes terminated with diamine anchoring groups as a function of the chain length by the STM-BJ technique [44]. Following the similar procedure as the alkanedithiol experiment, the conductance values of n-alkanediamine molecules are 42 (n=2), 7.3 (n=4) and 1.2 nS (n=6). It is also observed that the conductance decreases exponentially with the number of methylene units. Such charge transport behaviour is now well predicted by the superexchange mechanism (nonresonant tunneling regime) that $G = A_n \exp(-\beta_n N)$, where G is the conductance, A is related to the nature of molecule−electrode interaction, reflecting the contact resistance, β_n is the decay constant, which describes the efficiency of electron transport through the molecules, and N is the number of methylene groups. The decay constant (β_n = 0.81) is then obtained from the logarithmic plot of the measured conductance values and the chain length.

1.6 Molecular design concept

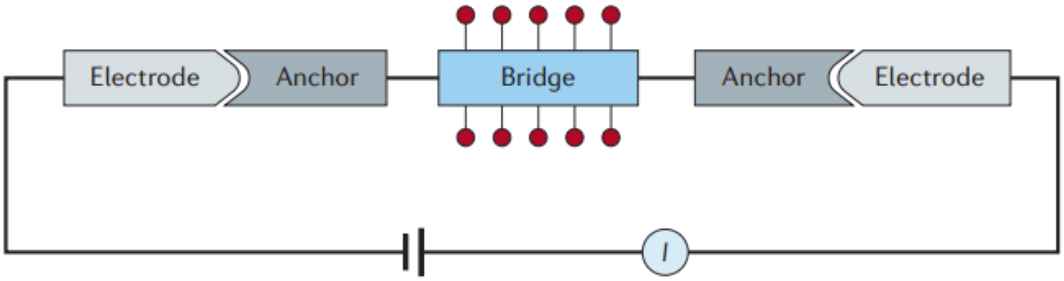

Figure 12. Schematic diagram of a single molecule junction with electrode, anchor and bridge components. Reproduced with permission. [56] Open Access, Copyright 2016, Springer Nature.

To further investigate the electrical properties within a molecular junction, it is helpful to approximately divide the junction into three parts: the intrinsic properties of the electrodes, the intrinsic properties of molecules (the bridge and anchor), and the molecule-electrode interaction as shown in Figure 12 [56]. Each of these parts can be considered as the key concept to understand the electrical properties of the junction and the molecular junction design.

1.6.1 Anchor groups

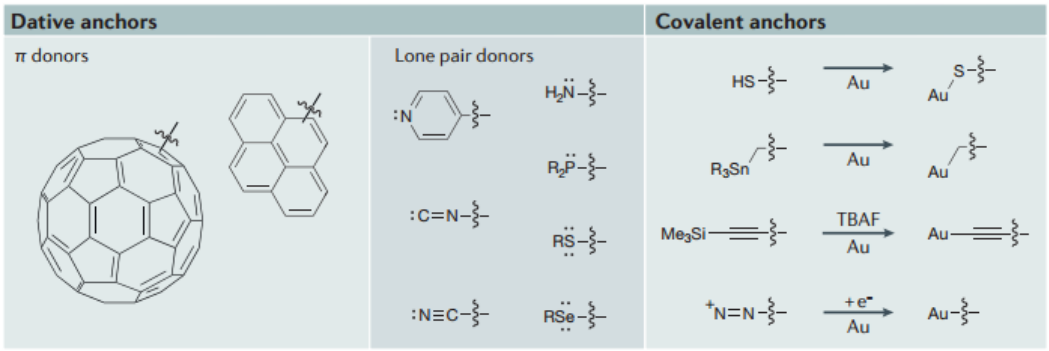

Figure 13. Molecular structures of common anchors. Dative anchors can be classified as π donating or lone pair donating. Covalent anchors commonly used to generate direct Au–S and Au–C contacts. Reproduced with permission. [56] Open Access, Copyright 2016, Springer Nature.

The anchor (linker or contact) groups serves as the connective point between the molecular wire and electrodes in molecular junctions. As shown in Figure 13, such anchoring groups can be divided into dative anchors (donor-acceptor interaction) or covalent anchors (in situ covalent contact). For the dative anchors, electrons donated

from the molecules to the gold atoms through π donors or lone pair donors, for example, fullerenes and some other π-conjugated hydrocarbon are common π donor molecules [57-62], while the amines are commonly lone pair donor (σ-donor) ligands with relatively narrow contact geometry to the gold. In such interaction, the gold electrode is considered as the Lewis acid to accept the lone pairs from the molecules. For the covalent anchors, the resulted covalent bonding is physically robust and stable which is formed between the molecular radicals and the electrode. The most widely studied covalent bonding is the Au-S linkage, it is ascribed to the strong chemical bonding between the thiol terminated molecules and the gold electrode. However, thiols can be also problematic in the air condition since its oxidization to disulfides and further polymerized to insoluble polydisulfides when used as molecular wires. Thus, thiol-based junctions have shown variability in the measured conductance values due to the different molecule-electrode geometry.

1.6.2 Backbones or bridges

The backbone of molecules is the main channel for the charge flows, it holds great potential to tune and manipulate the electrical or functional properties of the molecular junction. One of the most important parameter to describe the backbone properties is the decay constant value (β) which indicates the behaviour of charge transport decays with the increase of the oligomer length. For short molecular junctions, the general conductance behavior is now well described as nonresonant tunneling (see the conductance formula in section 1.5). This regime predicts an exponential decrease of the conductance with the molecular length, while a weaker length dependence for longer molecular lengths is generally attributed to hopping-type mechanisms [63].

Due to the absence of strong conjugated bonds to carry electrons, molecules structured with alkane backbones ($[CH_2]_n$) have shown high decay constant value in molecular junction (e.g., β = 0.84 $Å^{-1}$ for alkanedithiol). While, backbones with strongly conjugated properties (([benzene]$_n$), π-conjugated) have shown more capability in charge transportation, which thus has a relatively low conductance decay value (e.g., β = 0.43 $Å^{-1}$ for diaminobenzene). For conjugated backbones but non-

aromatic systems ($[C_2H_2]_n$), a lower decay constant value has been observed than these purely aromatic structures (e.g., β = 0.22 $Å^{-1}$ for alkene). For permethyloligosilanes ($[SiMe_2]_n$) molecules with structural similarity to alkane backbones, it has a comparable decay value to conjugated systems (0.39 $Å^{-1}$) which is ascribed to the effective charge transport properties of Si-Si σ bonds.

With the basis of the molecular design from the aspects of anchor groups and backbones, it is possible to manipulate the properties of molecular wires and realize the structure of functional molecular junctions. By inserting a methylene (CH_2) group between the thiol atom and the phenyl rings, the electrode and molecule interaction is disrupted. Such reduction of the junction conductance can reach to three orders of magnitude compared to the originally conjugated structure which makes it valuable to produce potential molecular switches. Single molecule rectifier can be also made by creating a molecular structure with a weak bonding at one side and a strong coupling at the another side. A -SPh group is used to replace the one of the two SH groups to create the misalignment of the junction symmetry. The charge flows are much more favoured to transport through S-Au (strong) side to the SPhR-Au (week) side. More detailed examples of molecular devices will be discussed further below.

1.6.3 Molecular devices

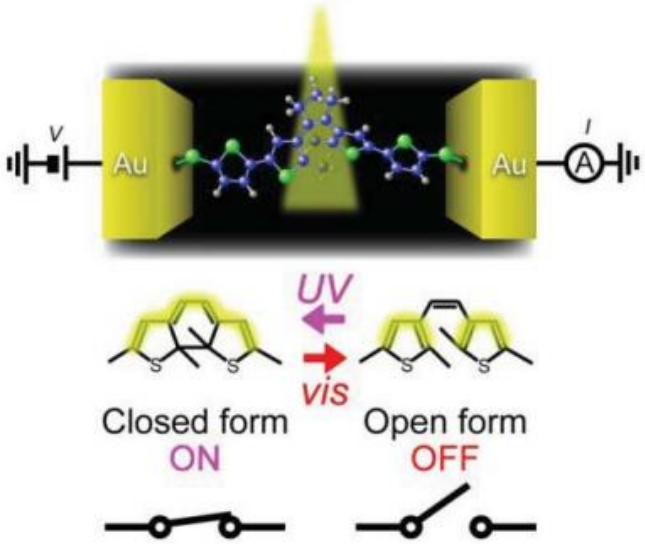

Figure 14. Schematic of a single molecule junction controlled by lights. Reproduced with permission. [1] Open Access, Copyright 2012, MDPI.

Binary switching in molecular junctions allows the current flows transferred or interrupted from one electrode to another one, it can be achieved by stochastically forming and breaking the molecular junctions or controlling the molecular conformations and metal-molecule contact configurations [64-65]. Molecular conformations can be controlled by electric field, mechanical forces and illumination. For example, photochromic switches are created by transforming the molecular conformation from non-conjugated open form to the conjugated closed form [66]. 1,2-diarylethene is a photochromic molecule and possesses a reversible ring opening and closing behaviour upon irradiating with visible and UV light (Figure 14).

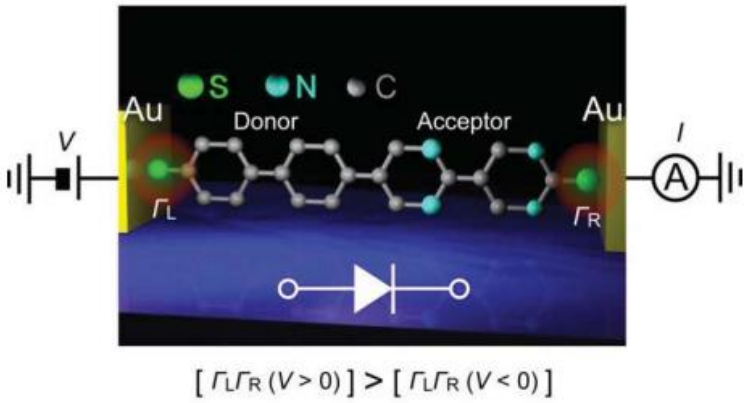

Figure 15. An illustration of the dipyrimidinyl-diphenyldithiol single molecule junction with a donor-acceptor molecular structure. The suppression of electron flow from the left to the right was observed. Reproduced with permission. [1] Open Access, Copyright 2012, MDPI.

A diode can facilitate current flow in one (forward) bias direction while suppressing the other (reverse) bias direction. The configuration of single-molecule diodes is similar to the p-n junction that consists of donor (D) and acceptor (A) moieties connected via a σ bond (as seen in Figure 15). The first single-molecule diode was made using a MCBJs technique [67]. A phenyl group was functionalized with four fluorine atoms to form the donor-acceptor structure, as a result, a behaviour of rectification was observed.

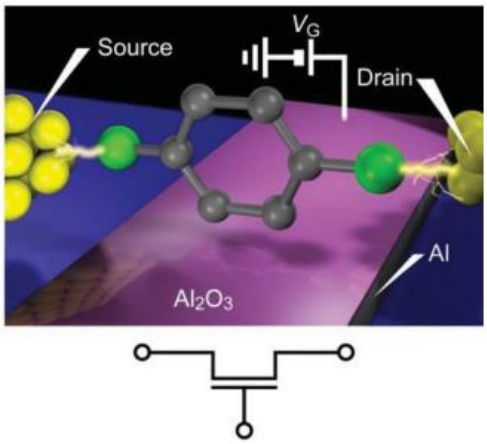

Figure 16. A schematic illustration of the single-molecule FET. Reproduced with permission. [1] Open Access, Copyright 2012, MDPI.

Single molecule junctions possess the possibility to downscale the field–effect transistor to the sub-10 nm scale, offering a potential solution for the size limitation of current metal-oxide-semiconductor field effect transistors (MOSFETs). The challenge to build a single molecule FETs is the placement of a gate electrode very close to the molecule since the distance in between requires a nanometer scale to get the strong coupling. Single-molecule FETs were first demonstrated by Song et al. [68]. In their study, benzenedithiol molecules were linked between source and drain metallic nanogap electrodes, and an Al_2O_3/Al electrode was used as a back gate to investigate the current flowing through the molecule.

1.6.4 Electrodes

To date, metallic gold is the most widely used electrode in molecular junctions owing to its good stability, high conductivity, good fabricability and the absence of surface oxides in air. Moreover, gold could form strong covalent bond with some particular anchoring groups (e.g., the Au-S bond). However, the non-compatibility with current complementary metal-oxide semiconductor (CMOS) technology, the mobility of surface atoms, non-transparency in optical devices and the expensive price limit the further applications of gold electrodes [50].

There is an increasing realization that new single-molecule electrical junction functionality can be achieved through the use of non-gold metals (Pt, Ag and Cu), non-metals (Indium-tin oxide) [48-50] and even novel two-dimensional (2D) materials (graphene, carbon nanotubes, h-BN, MoS_2, $MoSe_2$, WS_2 and WSe_2). Kim et al. have formed graphite−molecules−Au molecular junctions by the use of the STM-BJ technique and measured the conductance of amine-terminated oligophenyl compounds [69]. Ullmann et al. presented a reliable fabrication of graphene molecular junctions with C60 endcapped molecular wires [70]. Dappe et al. combined carbon tips with graphene as a counter electrode to construct all-carbon molecular junctions [71]. Cao et al. have used graphene electrodes to create “robust and identical molecular transport junctions” using a lithographic method [72]. To further prove the effectiveness of their junctions, they capped molecules with amino groups to construct graphene−molecule−graphene symmetric junctions, which showed excellent reproducibility and stability. These fundamental studies suggest that carbon based materials have the potential to be valuable alternative electrode materials for molecular electronics in the next generation of nanostructured devices.

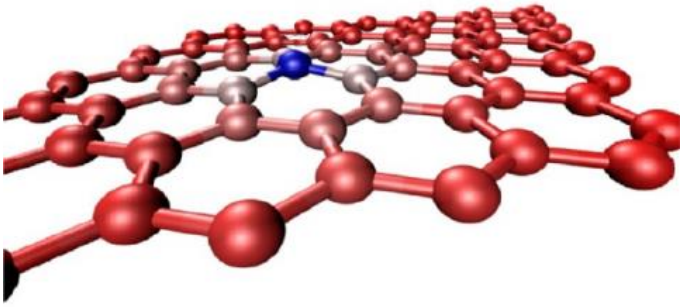

Figure 17. The structure of graphene with honeycomb lattice. Reproduced from Ref. 78 with permission from The Royal Society of Chemistry.

Graphene is a flat monolayer of carbon atoms arranged in a 2D honeycomb lattice structure, since its experimental discovery in 2004, it has already been foreseen as an important future technology and applications of this material are gaining momentum [73-74]. Because of its zero-bandgap, flat and super thin structure, graphene has exhibited remarkable electronic, thermal, mechanical and optical properties [75]. The high mobility of charge carriers and excellent thermal conductivity make graphene a very promising electrode. With its high optical transmittance (97.7%), graphene can be applied in optical devices, overcoming the drawback of metallic electrodes. Graphene also has outstanding stability during the fabrication because of its high Young's modules (~1.1 TPa) [76], fracture strength (125 GPa) [76], specific surface area (2630 m^2g^{-1}) [77] and chemical stability. There are many important applications in different fields of the graphene material such as ultra-strong lightweight components used in space shuttles, transparent electrodes in solar cells and photoelectric devices [77-78]. Fabricating carbon-based electrode such as graphene into molecular junctions can take the advantage of its remarkable properties, giving it possibilities to furnish high quality, robust and reliable molecular electronics [79-81].

1.7 Aim of the study and further challenges

One of the most important purposes of this study is the possibility of constructing non-metallic molecular junctions and the investigation of the corresponding charge transport properties through such junctions. As a first step toward realizing the potential of using carbon based materials as electrodes, we demonstrate the use of graphene as a bottom electrode in place of the more commonly used gold. The well-studied systems of thiol-terminated 1,n-alkane molecular bridges were selected as a test-bed to investigate the possibility to use graphene electrodes to form single molecule junctions. With the successful formation of graphene based junctions, we change the molecular wire from alkanedithiol to alkanediamine to compare the effects of anchoring groups in such junctions. We also studied the technical effects of molecule-electrode contacts by comparing methods (STM-BJ, STM $I(s)$ and CP-AFM BJ) for capturing and measuring the electrical properties of single molecules in gold−graphene contact gaps. In order to reduce the conscious or unconscious bias during the selection of the conductance data, we introduce an efficient data sorting algorithm and demonstrate its capacity on real experimental data sets.

Based on the discussion above, the biggest challenge in molecular electronics is the reducing of device variabilities while retaining the molecular functionalities themselves [82]. Statistical analysis may reduce the data fluctuations but it cannot solve all the reproducible problems. Another challenge is the intrinsic misalignment between the metal states of electrodes and discrete molecular energy levels. Other challenges include the problems of power dissipation, integration capability, CMOS-compatibility, efficiency and the cost when molecular components are used in current computing systems. In addition, the current solid-state technology cannot meet the requirement for molecular design with a high degree of control. Fortunately, with the development of carbon-based 2D materials, the use of such materials as the electrode might reduce the electronic mismatch at molecule/electrode interfaces and this could create more robust and reproducible systems for future nanoelectronics.

2 Chapter 2: Experimental section

2.1 Chemicals and sample preparation

Graphene substrates (1 cm × 1 cm) were purchased from The Graphene Supermarket and consist of a few layer graphene layers on top of a nickel substrate. Raman spectroscopy (HORIBA Scientific) and STM (Bruker, EC-STM) were used to check the quality of each substrate. The gold substrate (1 cm × 1 cm) was annealed under a butane flame to generate an Au (111)-microstructured surface before its use in the experiments. In general, the substrate was placed into the butane flame by a tweezer until the dark red glowing was observed, keep flaming for another 10 seconds and then remove the gold substrate from the butane flame. Finally, the gold substrate was cooled down on a flat base for 30 seconds. This annealing process was repeated for three to four times to generate the Au (111) terraces. Take care not to overheat the sample since the gold was coated on the glass substrate.

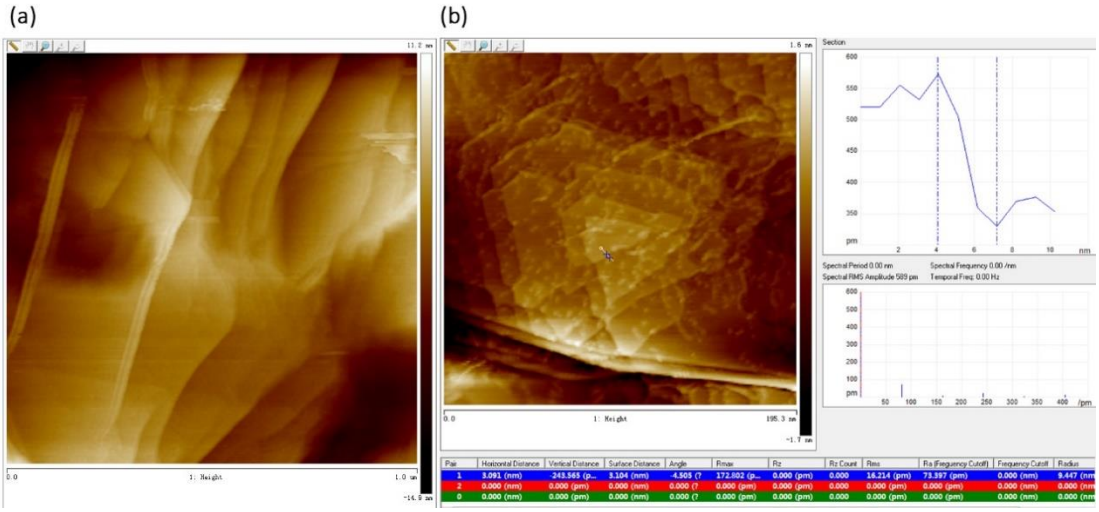

Figure 18. (a) The structure of graphene with honeycomb lattice. (b) The height analysis of the single layer graphene

Figure 18a is the STM spectrum (1 μm × 1 μm) of the graphene substrate, it is clear to see multilayers of the graphene from the spectrum. By further scaling the scanning region to about 100 nm, significant steps are observed with the height analysis to be 0.3 nm for a single layer graphene (Figure 18b). It is also worth to note that the geographical

situation of each sample point may be varied due to the chemical vapour deposition (CVD) conditions. It is thus necessary to locate many points on the surface to find the suitable junction forming positions.

1,n-alkanedithiols (n = 4, 6, 8, 10) and 1,n-alkanediamines (n=2, 4, 6, 8, 10) were purchased from Alfa Aesar and TCI chemicals respectively and used as received. 1,12-dodecanedithiol was synthesized in our lab and then characterized by nuclear magnetic resonance (see the detailed synthesis route and spectra below). Distilled water used in this experiment was supplied by an in-house purification system. Molecular adsorption to graphene substrate was generally achieved by immersing the qualified graphene substrate into molecular solutions (alkanedithiols−methanol, 1:20, v/v) for 90 s.

Synthesis of 1,12-dodecandithiol

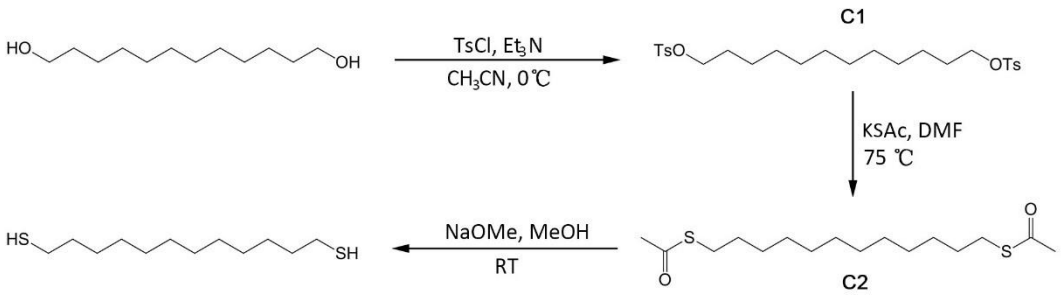

Figure 19. Synthesis route of 1, 12-dodecanedithiol.

Compound 1 (C1)

1,12-dodecanedithiol was prepared from the staring material of 1,12-dodecanediol. We firstly dissolve the alcohol (15mmol, 2.82g), 4-methylbenzenesulfonyl chloride (52.5mmol, 10g), and trimethylamine (52.5mmol, 7.32ml) in 100 ml dry acetonitrile (CH_3CN) for 2.5 hours at 0℃ and then diluted with 100 ml distilled water. The mixture was then extracted with 50 ml dichloromethane (DCM) three times. The organic layer was then washed with 100 ml saturated NH_4Cl, 100 ml brine and dried with $MgSO_4$. A column was used to purify the compound 1 (3.32 g).

Compound 2 (C2)

The compound 1 was dissolved in 20 ml dry dimethyl formamide (DMF) with 2.28g potassium thioacetate (KSAc) added. The colour changed to brown at this point. The reaction was keep stirring at 75℃ overnight and then remove the DMF under the conditions of 15 mbar and 55℃. The mixture was then diluted with 100 ml DI water and extracted with 100 ml ethyl acetate three times. The separated organic layer was then washed and dried with 100 ml brine and $MgSO_4$. A column was also set to purify the compound 2 (0.5 g).

1,12-dodecanedithiol

Compound 2 was dissolved in 50 ml degassed, dry methanol (MeOH) under argon atmosphere followed by the addition of sodium methoxide (NaOMe, 15mmol, 0.81g). The reaction was stirred for an hour at room temperature and then quenched with 60 ml, 1M HCl. The organic layer was then extracted with 25 ml DCM three times and dried with 25 ml brine and $MgSO_4$. The 1,12-dodecanedithiol was obtained by the column chromatography as the white solid (0.1g, 20%).

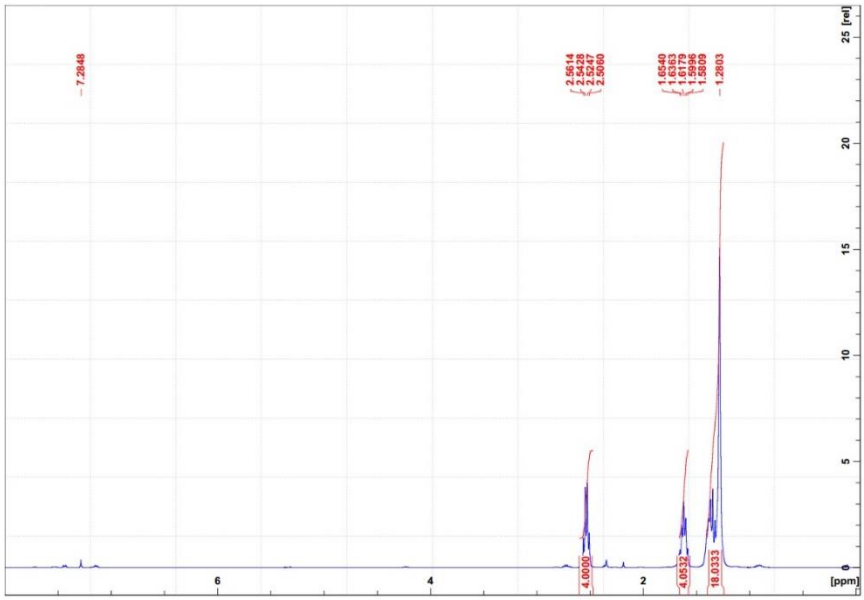

Figure 20. ^{1}H NMR of 1, 12-dodecanedithiol. ^{1}H NMR (400 MHz, $CDCl_3$) δ 2.54 (quart, J = 7.48 Hz, 4H), 1.61 (quint, J = 7.88 Hz, 4H), 1.43-1.28 (m, 18H).

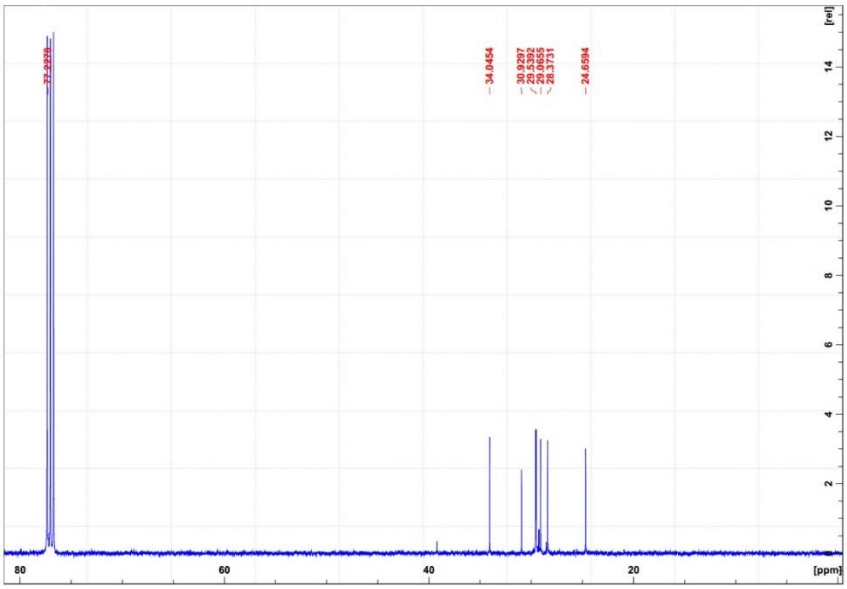

Figure 21. ^{13}C NMR of 1, 12-dodecanedithiol. ^{13}C NMR (100 MHz, $CDCl_3$) δ 34.0, 30.9, 29.5. 29.1, 28.4, 24.6.

The product was sent for nuclear magnetic resonance spectroscopy (NMR) to check the structure. The spectra are shown as Figure 20 and 21 which agree well with the literatures [77-78]. ^{1}H NMR (400 MHz, $CDCl_3$) δ 2.54 (quartet, J = 7.48 Hz, 4H), 1.61 (quintet, J = 7.88 Hz, 4H), 1.43-1.28 (m, 18H). ^{13}C NMR of 1, 12-dodecanedithiol. ^{13}C NMR (100 MHz, $CDCl_3$) δ 34.0, 30.9, 29.5. 29.1, 28.4, 24.6.

2.2 Formation of the self-assembly monolayers (SAMs)

The self-assembled monolayers can be either formed by simply immerse the substrate into the molecular solution or generated in the liquid cell. In CP-AFM BJ measurement, it was conducted in the air environment with the SAMs formed by immersing the substrates (both gold and graphene) into the diluted alkanedithiol solution (5%, w/w or 1mM) for 90 seconds. For example, 1,6-hexanedithiol was diluted to 5% in methanol by dissolving 1 ml of 1,6-hexanedithiol in 25 ml methanol. For STM-BJ and STM $I(s)$ techniques, such measurements on the gold were performed in the liquid cell. The diluted molecular solution in mesitylene (1 mM) was injected to the liquid cell after the well setting of the experiment. The cell was cleaned in an ultrasonic bath with piranha solution for 5 min, followed by 5 min in an ultrasonic bath with ethanol/acetone solution. In order to prepare the ideal SAMs, it is also necessary to prepare several solutions with different concertation of the target molecule and check the junction formation possibility in the measurement.

2.3 Preparation of the tips

The gold-coated AFM tips were purchased from the Budget Sensors (Multi75GB-G) and used after calibration of the force constant and resonance frequency on the sapphire substrate. The basic parameters of the AFM tip, for example, the radius of the tip, shape, force constant, resonance frequency and dimensions of the cantilever were provided from the manufacturer. These values may be varying for each specific tip due to the manufacturing diversity. The determination of the resonance frequency is achieved by the thermal tune function of the AFM while the force constant is examined on the hard contact of the sapphire substrate. See section 2.4.3 below for the conversion of the voltage and forces in the AFM technique.

STM tips with good spatial resolution and image quality are quite important for the STM based experiments. Over the past three decades, more than ten methods have been developed to obtain the ideal tip with single atom at the apex [68]. Among these methods, mechanical cutting is the easiest way but it will produce multiple atoms of tips with low reproducibility, while the electrochemical etching method is good for

producing relatively reliable and reproducible STM tips. In our experiment, the tips for the STM BJ were cut mechanically before use (with scissors), whereas the tips for the *I*(*s*) technique were made by electrochemical etching of gold wires (0.25 mm, Tianjing Lucheng Metal company, 99.99%).

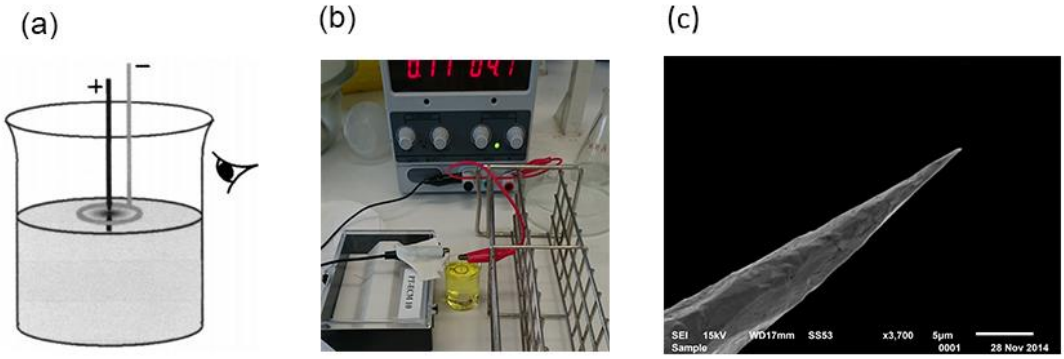

Figure 22. (a) Schematic diagram of the electrochemical etching. (b) A photo of the experimental setup. (c) A typical SEM image of the as-prepared tip.

Reported by Ren et al. in 2004 [83], the setup of the method is shown as Figure 22. A gold ring with 8 mm in diameter was placed on the surface of the solution, then a gold wire of 0.25 mm diameter was immersed in the centre of the ring. The gold ring and gold wire were connected to the negative and positive electrodes of a potentiostat respectively. Hydrochloric acid and ethanol (50:50) were used as the electrolyte for etching. During the electrochemical reaction, hydrochloric acid was used to supply Cl^- ions and the ethanol was intended to reduce the bubbles produced.

By applying the external voltage at 4V, the electrochemical etching begins with the observation of bubbles around the gold ring. The voltage circuit was then switched off after the fallen of the lower gold wire. A rinsing process was also conducted to clean the remaining electrolyte on the surface of tips. The tip was then transferred to SEM to check the quality as shown in Figure 22c.

2.4 The conductance measurement experiment

2.4.1 STM Break Junction Technique.

A modified STM system (based on Keysight Technology 5500) was used for the STM BJ method. A mechanically cut Au tip was used to fabricate the gold−molecule−gold and gold−molecule−graphene molecular junctions. The gold/graphene substrate was mounted on the STM stage with the liquid cell. The gold tip was brought close to the surface at a current of 0.015 nA with a bias voltage of 0.2 V during the tip approach. The current was then increased to 0.1 and then to 1 nA in a stepwise manner to check the stability. Finally, the current was set to 30 nA to create the metallic point contacts in the case of gold/gold junctions or hard gold/graphene contacts for the graphene experiments. The current−distance signals were recorded with an external data acquisition instrument. A Z-sweep could be applied to the scanner (Z sweep 4 nm, 0.3 per second) if the system became unstable to help remove tip instabilities/contamination. The collected curves were then used for data analysis and histogram generation.

2.4.2 STM-Based *I*(*s*) Technique.

This technique was implemented in accordance with methods first described by Haiss et al. [13] with necessary modifications to our Bruker STM equipment. The electrochemically etched Au tip (ethanol/HCl 37% = 1:1, voltage = 4 V) was set at an initial vertical distance (4 nm in our experiment), and then the tip was brought close to the molecularly functionalized substrate by selecting a large current set-point (I_0) value. When the distance between the tip and substrate reached the preset threshold of the set-point current, the feedback loop was disconnected, the STM tip was then rapidly withdrawn to the initial vertical distance. During this process, the current was measured as a function of vertical distance. For each molecule, the parameters such as the applied bias, vertical distance, trigger threshold and moving speed can be varied. The conductance of Au−1,8-octanedithiol/1,6-hexanedithiol−Au junctions was determined in the liquid cell, whereas the conductance of graphene based junctions was measured under air conditions.

2.4.3 CP-AFM Break Junction Technique.

The Bruker Multimode 8 microscope equipped with a conductive AFM application module was used for formation of the molecular junctions by the CP-AFM BJ method. Such experiments were performed under ambient conditions with a conductive gold AFM probe and target molecules covered on the gold/graphene substrates. To obtain the contact between the two electrodes, the AFM contact mode is selected at a scan rate of 1 Hz, a sample bias of 0.3 V, and an applied piezo scanner voltage of 0.5 to 8 V (corresponding to a force of 20 to 300 nN). The current amplifier was calibrated using high-precision resistors. The force applied to the surface can be varied depending on the experimental conditions and requirements. In our setup, we use the minimum force which gives a sufficiently stable current signal. Similar to STM based techniques, the collected current and distance signals were then sent for data analysis to get the most probable conductance values of the junction.

Calibration of the CP-AFM module and scanner.

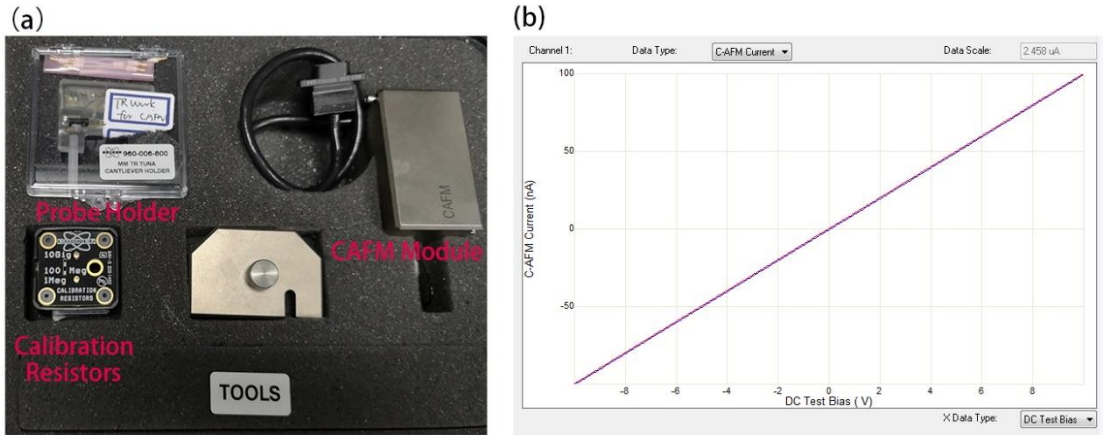

Figure 23. (a) The photo of the CP-AFM application module assembly (b) The standard *I-V* curve for calibrating the CP-AFM application module and the scanner.

Before performing the conductance measurement of the molecular junction, it is important to calibrate the CP-AFM module and piezo scanner in order to get accurate signals. The calibration resistor (100 Meg Ohm) is used for such test (Figure 23a). For the software setup, the system is set to the "Scan Mode" followed by a "False Engage", then the "Ramp mode" is selected in the Workflow toolbar to test the relationship between DC Test Bias (V) and CP-AFM Current (nA). Figure 23b shows a linear correlation of the applied bias (-10 to 10V) and the CP-AFM current (-100 to 100 nA), indicating the good situation of the system.

Conversion of the applied voltage (V) and the applied force to the surface (F)

According to the spring constant formula, $F=kx$, both parameters of spring constant (k) and deflection distance (x) are required to obtain the force value applied to the surface. Since the deflection of the probe is controlled by the applied voltage (V) to the piezo scanner, the relationship (deflection sensitivity) between the applied voltage and the responded extension or retraction distance should be calibrated firstly. This was done under the "Contact Mode" on the hard sapphire substrate and calculated by the "Ramp" function from the Bruker Nanoscope software. The spring constant (k) of the probe is obtained by the "Thermal Tune" function under the withdrawal status and calculated by the Nanoscope software as well. Therefore, the relationship between the applied voltage and contacting force is then obtained by the simple calculation based on the spring constant formula.

2.5 Data analysis

2.5.1 Manually selection

To determine the conductance of each junction, usually over 2000 current−distance curves were collected, and those showing junction formation were selected on a consistent basis to avoid the artificial bias. Then conductance histograms were constructed as described in the literature by combining these traces, and the resulting peaks in these plots for selected molecules were used to compute the molecular conductance [11]. Briefly, *I-s* curves were imported to OriginPro 2016 software to plot 1D and 2D histograms. A Gaussian fit was applied to the peak in 1D histograms, as a result, the conductance of the single molecule can be defined as peak center ± half of the full width at half maximum (FWHM). 2D histograms were plotted by the descriptive statistics function in the Origin, the 2D frequency counts of the conductance data was obtained, indicating the most probable distribution region of the conductance values.

2.5.2 Automatic data analysis algorithm

In Chapter 6, we introduce an efficient data sorting algorithm, including filters for noisy signals, conductance mapping for analyzing the most dominant conductance group and sub-population groups. The capacity of our data analysis process has also been corroborated on real experimental data sets of Au-1,6-hexanedithiol-Au and Au-1,8-octanedithiol-Au molecular junctions. The experimental data sets for gold-molecules-gold molecular junction were collected by the STM based $I(s)$ technique in a liquid cell environment.

Parameters of the data analysis algorithm

The data analysis algorithm was written in Matlab (2016b) and the detailed classification approach is described in Chapter 6. All relevant scripts and data can be found in the Appendix. When setting the parameters of specific data sets, several attempts can be made to find the optimum values. The detailed parameters used in this work are shown in the table 2 below. Using the optimum parameters for the code, the most dominant conductance cluster has been located after the data sorting program.

Table 2. Parameters used in the experiment.

	1,6-hexanedithiol	1,8-octanedithiol
X-Filter	Data range: 0–2.8 nm Mean value: 0.1 Variance: 0.1	Data range: 0–2 nm Mean value: 0.1 Variance: 0.1
Y-Filter	Data range: 20–30 nA Mean value: 3.5 Variance: 30	Data range: 6.6–10 nA Mean value: 3.5 Variance: 10
Peak-Filter	Peak number: 3	Peak number: 3
Conductance mapping	Number of steps: 5	Number of steps: 19

Explanation of the given parameters

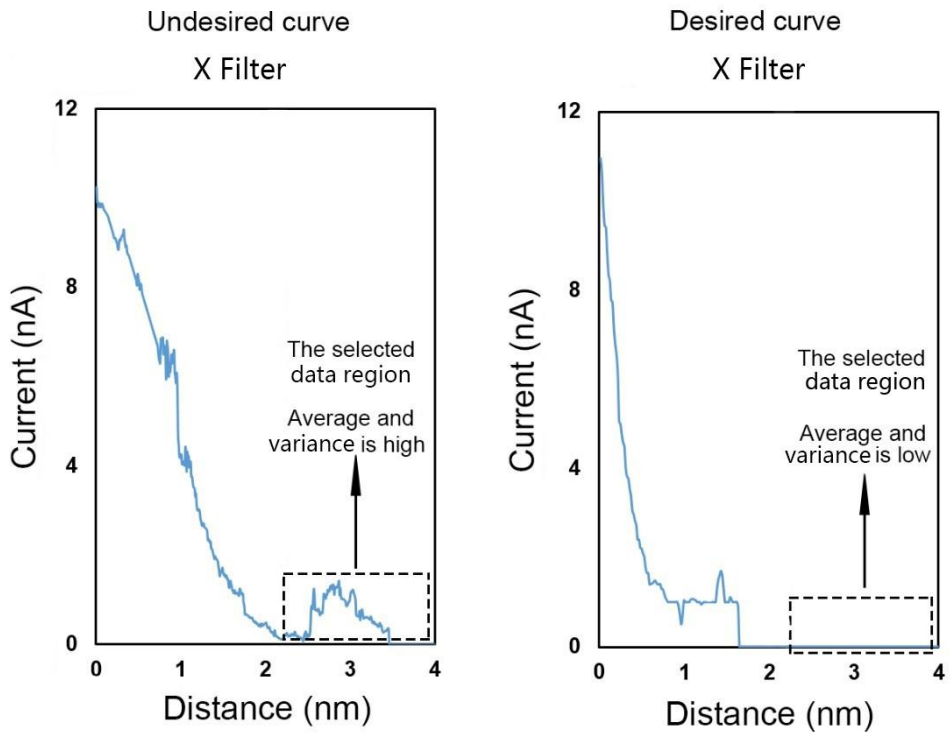

Figure 24. The parameter differences between the undesired curve and desired curve.

The parameters included in the study are not arbitrary choices of the operator, but based on a trial and error scheme. We firstly define an arbitrary, noise-free, exponentially decaying current–distance curve as the reference, the parameters for a standard noisy-free curve can be achieved. We then define a noisy curve as the reference to get the related parameters. Thus, the parameter combinations used for the trial and error scheme are generally in this range. Owing to the powerful computing capability of the computer, the software can list and try all the possibilities of the parameter combinations in a very short time. For example, the undesired curve in Figure 24 showed a high value of average and variance in the selected data region, while values for the desired curve are much lower, the script then takes these calculated values as difference to remove the undesired curves. The values in the study were chosen after many iterations of running the program, resulting in good Gaussian peaks in the histograms following double checking of the exported $I(s)$ curves.

Trial and error scheme

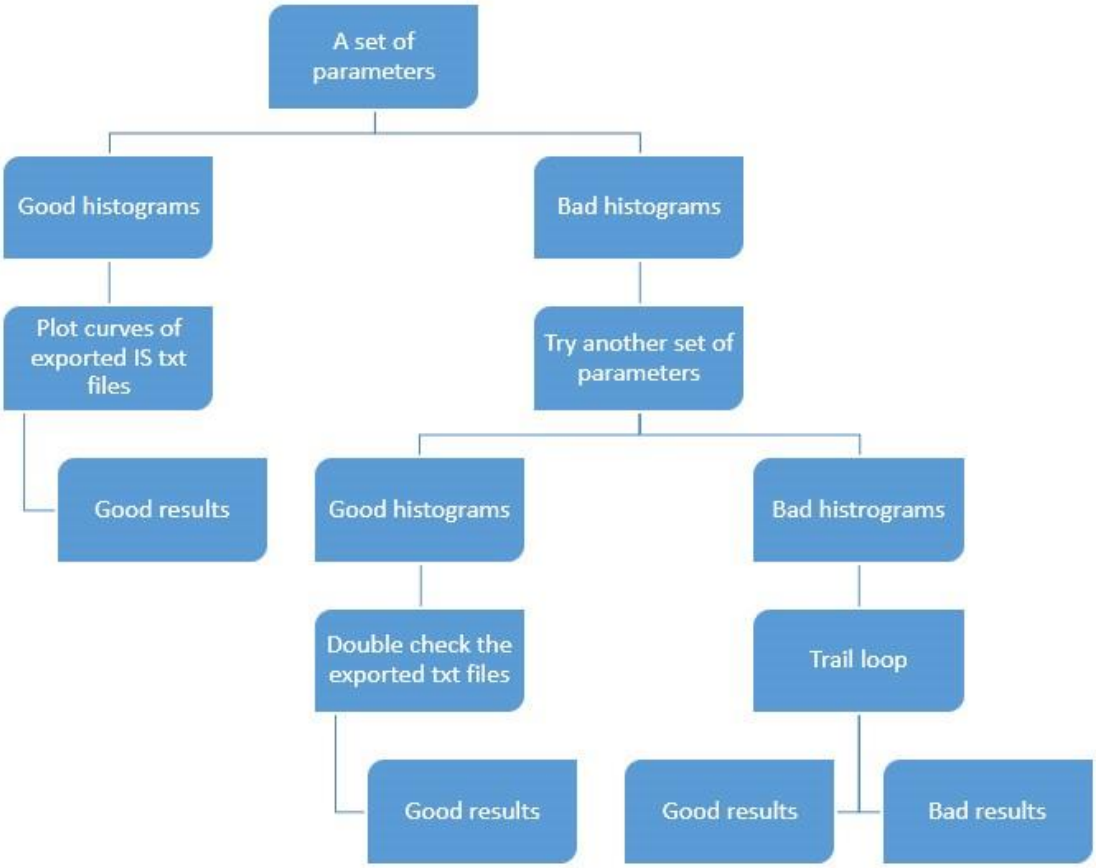

Figure 25. The flowchart of the trial and error scheme on how to obtain the good results and ideal parameters.

It is quite crucial to note that the selection of parameters does not simply rely on the subjective choices of the operator, but is based on a trial and error scheme as shown in Figure 25. Basically, with a set of parameters and raw $I(s)$ data, conductance histograms were generated by the algorithm within a minute, the selected files were then plotted as curves to double check the feature of plateaus. If bad histograms were obtained, a modified set of parameters was imported to run the script again and again. As long as the good histograms and $I(s)$ curves were obtained, we can treat the related parameters as a proper set, otherwise, the experiment data is bad.

Instruction of the data analysis algorithm

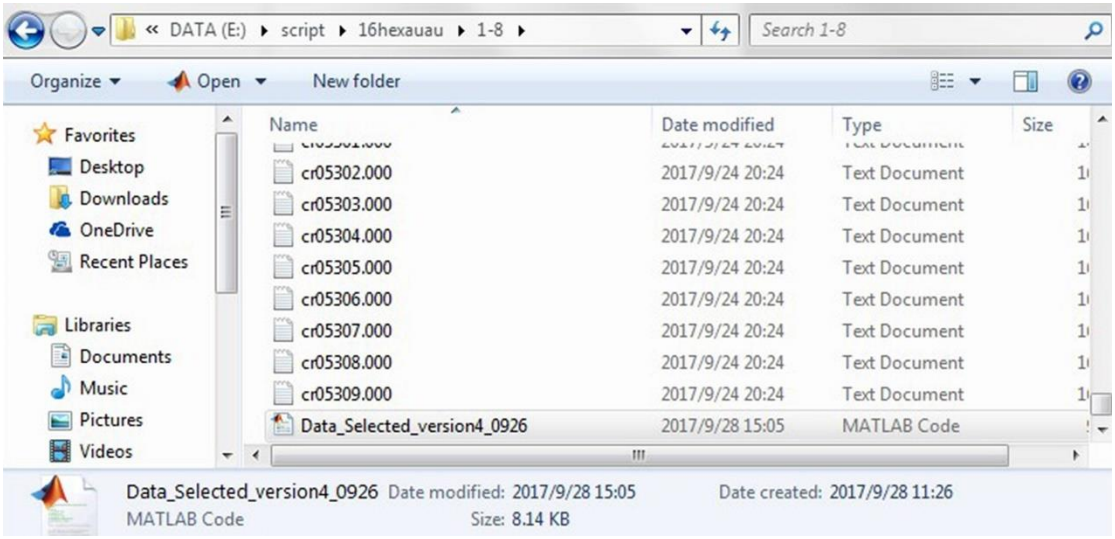

Figure 26. The screenshot of the exported $I(s)$ files in the same folder with Matlab code.

The raw $I(s)$ data were directly exported as ASCII text files, then the Matlab code was copied to the same folder of the $I(s)$ data.

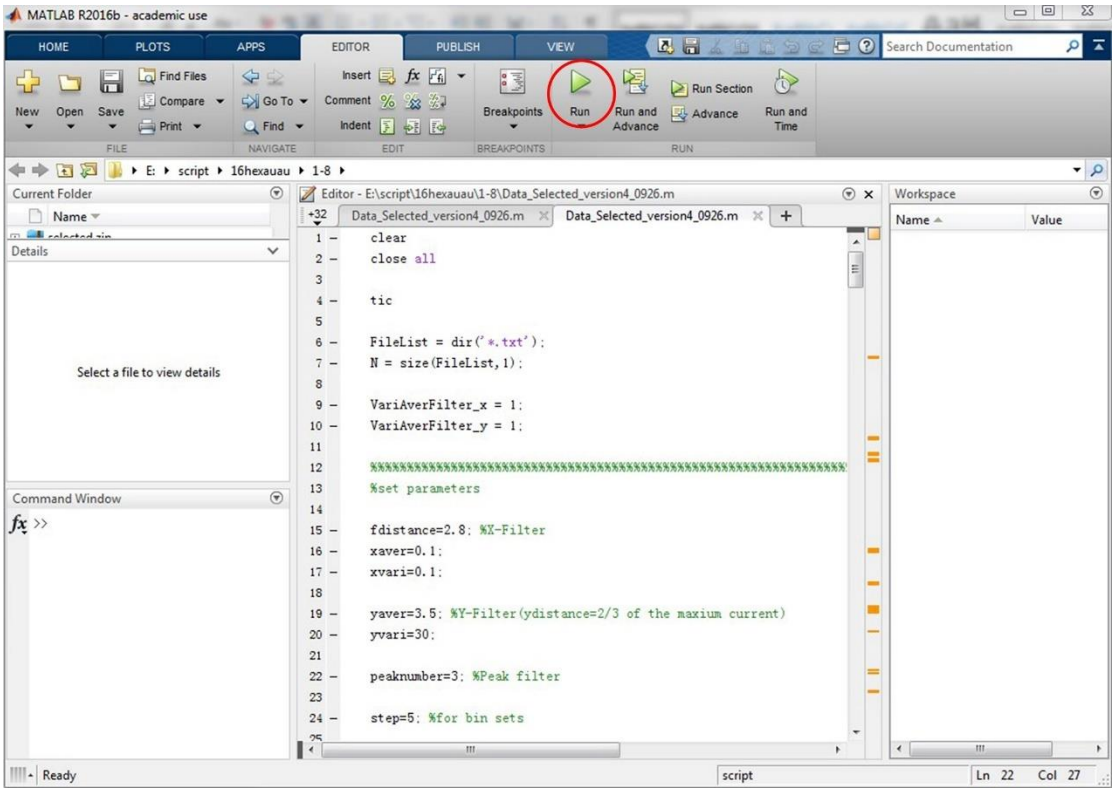

Figure 27. The screenshot of the Matlab code.

The Matlab code was displayed as Figure 27 by double click the code file. With the correct setting of parameters, the code was then executed by single click the run button as highlighted with a red circle.

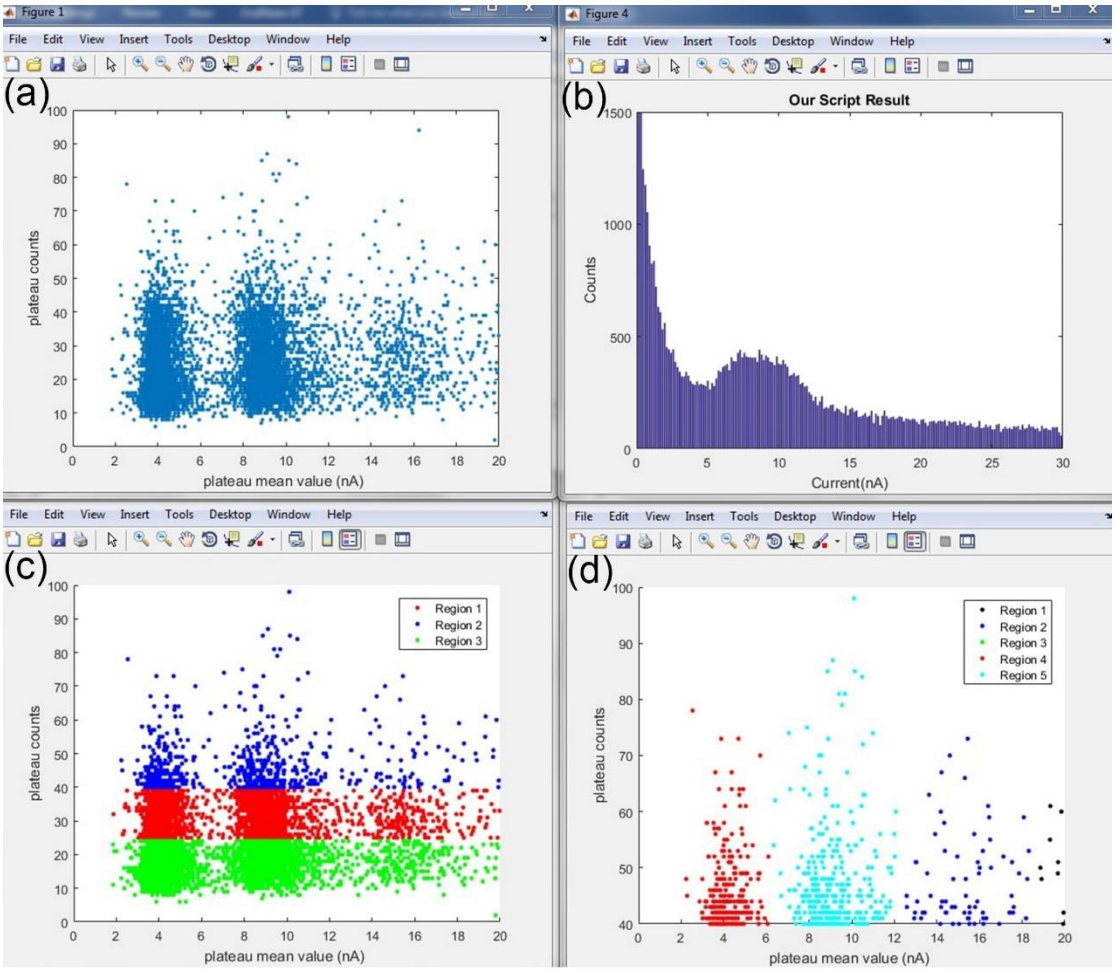

Figure 28. The screenshot of the generated 1D histogram (b) and conductance maps (a), (c), (d).

Within a minute, over 11,000 $I(s)$ were analyzed by the Matlab code, four histograms were then generated indicating the most probable conductance value of the molecular junction. Figure 28a shows the conductance map of all the $I(s)$ data without grouping. Figure 28b is the 1D histogram of the selected plateau featuring $I(s)$ curves, the selected $I(s)$ curves were also saved as a compressed file in the same folder. Figure 28c indicates the conductance map of all the $I(s)$ curves by grouping in three regions. Figure 28d represents the five defined regions of the blue region in Figure 28c. The detailed description can be also found in the Chapter 6.

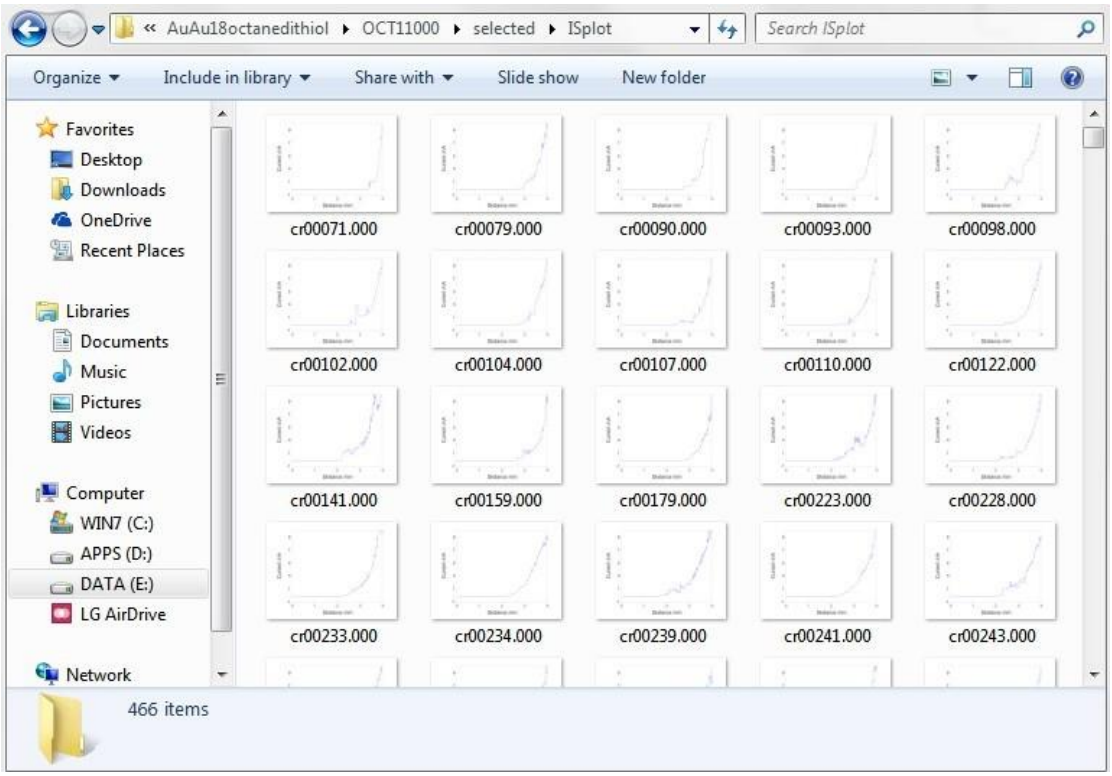

Figure 29. The screenshot of the exported *I*(*s*) curves.

The exported the *I*(*s*) files were plotted as traces to double check the plateau features.

3 Chapter 3: Charge Transport Properties of Alkanedithiol in Graphene Based Molecular Junctions

3.1 Preface

The research work in Chapter 3 was carried out in collaboration with the theoretical simulations by the Dr. Yannick J Dappe's group (CEA, CNRS, France). I will present my experimental work on the construction of gold−n-alkanedithiol−graphene asymmetric junctions and the related measurement of the charge transport properties. The results presented in this chapter were published and reproduced with permission from *Nano Lett.* **2016**, *16*, 6534−6540 (DOI: 10.1021/acs.nanolett.6b03180), with the title: 'Graphene as a Promising Electrode for Low-Current Attenuation in Nonsymmetric Molecular Junctions'. Copyright 2016, American Chemical Society. This study was designed by Richard J. Nichols, Li Yang and Cezhou Zhao. I carried out the main experimental work on the application of the $I(s)$ method, junction formation and data analysis plus writing the first draft of the manuscript. César González and Yannick J. Dappe conducted the simulation work and developed analysis tools. The manuscript was then corrected by Yannick J. Dappe, Richard J. Nichols, and Li Yang. The rest of authors conducted some other supporting works, for example, the data analysis, discussion and double check the experimental results.

In this chapter, we investigate the possibility of constructing non-metallic molecular junctions and the corresponding charge transport properties through such junctions by replacing the common gold electrode with a graphene electrode. We have measured the single-molecule conductance of 1,n-alkanedithiol molecular bridges (n = 4, 6, 8, 10, 12) on a graphene substrate using scanning tunnelling microscopy (STM)-formed electrical junctions. The conductance values of this homologous series ranged from 2.3 nS (n = 12) to 53 nS (n = 4), with a decay constant β_n of 0.40 per methylene (−CH_2) group. This result is explained by a combination of density functional theory (DFT) and Keldysh−Green function calculations. The obtained decay, which is much lower than the one obtained for symmetric gold junctions, is related to the weak coupling at the molecule−graphene interface and the electronic structure of graphene.

As a consequence, we show that using graphene nonsymmetric junctions and appropriate anchoring groups may lead to a much lower decay constant and more conductive molecular junctions at longer lengths.

Despite the main description in the publication, I will provide more interpretations here about the energy level shift in this study which is important to understand the low decay value of the graphene based junction. It is well-known that when a thiol-terminated molecule is adsorbed on gold, there is strong charge transfer from the sulfur to gold which is driven by an interface electric dipole. In the case of a gold-alkanedithiol-gold molecular junction, the HOMO level is known to be located around 2 eV below the Fermi level. There is a cancellation of the two interface dipoles, leading to an electrostatic equilibrium in the molecular junction. In the present case of the nonsymmetric gold−molecule−graphene junction, this equilibrium is broken due to the unbalanced the coupling strength (Au-Au > Au-Graphene). Since the removing of charges from molecules depopulates the HOMO level, then we observe a HOMO level shift to the Fermi level (-0.4 eV).

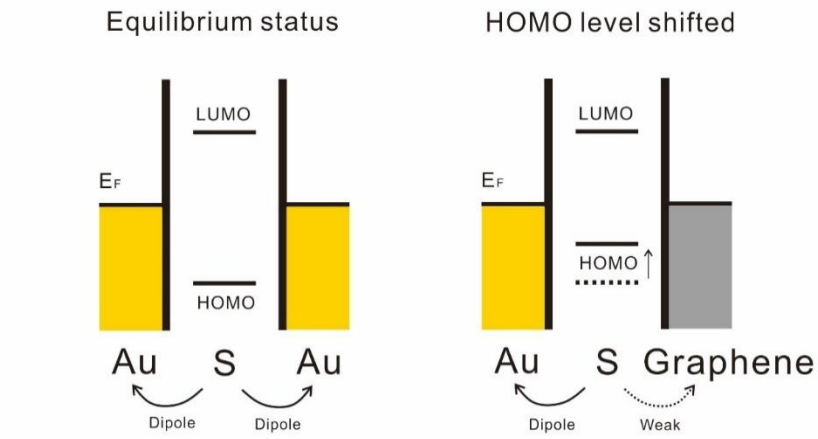

Figure 30. The equilibrium status and HOMO level shifted status of the gold-alkanedithiol-gold and gold-alkanedithiol-graphene junctions respectively.

3.2 Introduction

Although technologically relevant molecular electronic devices still seem a long way off, the ability to measure the electrical properties of single molecules can be now achieved with a variety of techniques that were not available at the genesis of the field [7]. The ability to construct robust and reproducible molecular junctions, both for large-area planar contacts and at the single-molecule level, and to reliably characterize their electrical properties has been a key driver of the field of molecular electronics over the past decade [44]. In particular, the development of techniques using, for example, mechanically controlled break junctions (MCBJ), scanning tunneling microscopy break junctions (STM-BJ), conductive probe atomic force microscopy (CP-AFM) and the $I(s)$ technique (I = current, s = vertical distance) based on STM [10-13] have given new understanding and control of the flow of current through molecules [28]. These techniques share the general concept of trapping molecules between two contacting electrodes and thereby assembling metal−molecule−metal junctions for electrical probing. Through such measurements, as well as measurements on large-area junctions, it has become clear that many factors can influence the electrical current flow through molecular junctions, such as the intrinsic properties of molecules, electrodes, external environment, and so on [34,84,85]. So far, studies of single-molecular electrical properties have mainly focused on metal electrodes (Au, Ag, and Pt), largely due to the relative ease of their preparation and the ability to link molecules to these electrodes through a range of accessible chemisorption with a growing variety of anchoring groups (e.g., −SH, −NC, $-NH_2$, and −COOH) [48,86].

However, there is an increasing realization that new single-molecule electrical junction functionality can be achieved through the use of nonmetallic electrodes, with contacts such as indium−tin oxide (ITO) [49,50,87,88], carbon-based materials, and even novel two-dimensional (2D) graphene now being considered [89-91]. Kim et al. have formed graphite−molecules−Au molecular junctions by the use of the STM-BJ technique and measured the conductance of amine-terminated oligophenyl compounds [69]. Ullmann et al. presented a reliable fabrication of graphene molecular junctions with C60 endcapped molecular wires [70]. Dappe et al. combined carbon tips with

graphene as a counter electrode to construct all-carbon molecular junctions [71]. These fundamental studies suggest that carbon based materials have the potential to be valuable alternative electrode materials for molecular electronics in the next generation of nanostructured devices.

Graphene, since its experimental discovery in 2004, has already been foreseen as an important future technology and applications of this material are gaining momentum [73-74]. This carbon monolayer exhibits remarkable electronic, thermal, mechanical and optical properties due to its zero-band gap and flat and super-thin structure [75], making it useful as a platform for electronics, sensors, and electrodes in field effect transistors and as transparent contacts for photovoltaic devices [19]. Here, as a first step toward realizing its potential as electrodes, we demonstrate the use of graphene as a bottom electrode in place of the more commonly used gold. The well-studied system of thiol-terminated 1,n-alkane molecular bridges were selected as a test-bed to investigate the possibility to use graphene electrodes to form single molecule junctions. We have constructed gold-(1,n-alkanedithiol)-graphene hybrid junctions (n = 4, 6, 8, 10, 12) and measured the conductance of each molecular target using the so-called $I(s)$ STM method to form single molecule junctions [8]. In addition, we investigated the length dependence of conductance of these molecules with the decay constant (β_n) being experimentally determined across the n = 1 to 12 series, which we have compared with literature values for equivalent Au−molecule−Au junctions.

First-principles theoretical methods have already been shown to be highly valuable in interpreting the transport properties of molecular electrical junctions [92-93] and have been developed as indispensable tools for understanding, in combination with experiments, junction electrical properties and mechanisms of charge transport. Here, we show that the asymmetry of the junction and the combination of strong charge transfer at the gold electrode−molecule interface and weak coupling at the graphene bottom contact all play an important role in the electrical properties of the junctions. The combination of these factors leads to a strong reduction of the electronic length decay value, which is found to be about half of the value obtained for symmetric gold junctions. This lower attenuation factor leads to higher junction conductance for the longest junctions studied here.

3.3 Results and discussion

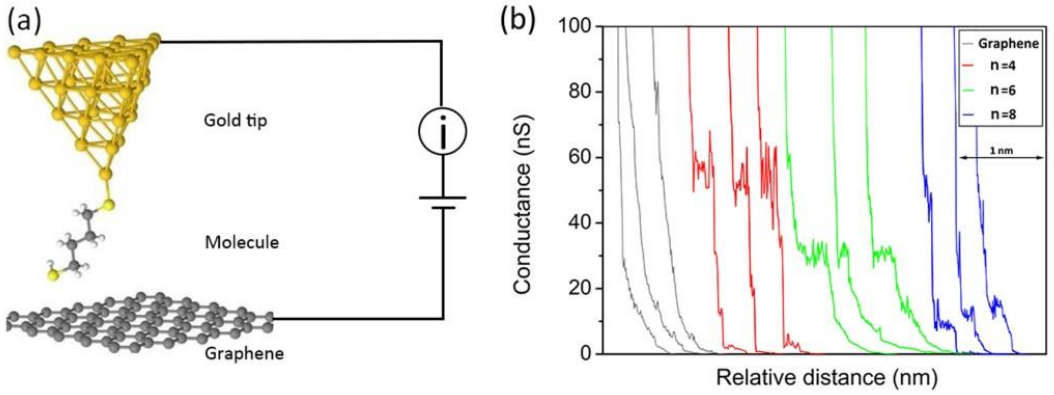

Figure 31. (a) Schematic diagram of the molecular junction formed in this study. (b) Typical *I*(*s*) curves of bare graphene (gray, without molecular junctions formed), gold−1,4-butanedithiol−graphene junctions (red), gold−1,6-hexanedithiol−graphene junctions (green), and gold−1,8−octanedithiol−graphene junctions (blue).

As mentioned above, the *I*(*s*) technique was used to construct gold−(1,n-alkanedithiol)−graphene hybrid junctions as well as to measure the single-molecule conductance (Figure 31a). Figure 31b shows two different kinds of typical conductance−distance curves: one type is the fast exponential decay (gray lines) of the current as a function of the distance between the tip and bare graphene substrate, and another type is the less-abrupt decay with the observation of well-defined plateaus (red, green, and blue lines). Taking 1,4-butanedithiol as an example, evidence for the formation of gold−1,4- butanedithiol−graphene hybrid junctions was derived from the observation of characteristic current plateaus located around 50−60 nS. Many factors can result in the sudden drop of the conductance in Figure 31b: one is the breaking of molecular junctions, and another one can be the change of metal−molecule configurations during the withdrawal [94-95].

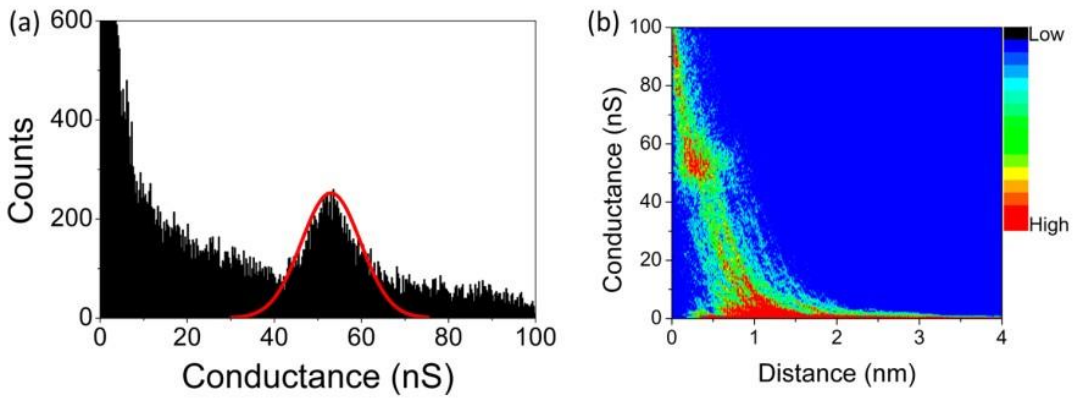

Figure 32. (a) 1D histograms of single-molecule conductance of gold−1,4-butanedithiol−graphene hybrid junctions with the Gaussian fit. (b) The corresponding 2D histogram with a sensitivity indicator of the conductance counts.

After the unbiased selection of plateaus featured curves, over 400 $I(s)$ curves were combined to form one-dimensional (1D) conductance and two-dimensional (2D) histograms, as shown in Figure 32. The 2D histograms were plotted by counting the data points corresponding to each conductance value as a function of the stretching distance of molecular junctions, and 1D histograms are represented by the conductance count values. From the 2D histograms, information concerning the distribution of conductance values and the length of the plateaus can be obtained, while the 1D histograms with peak fitting represent the conductance value. For each 2D histogram, a color bar was created to indicate the data sensitivity of conductance counts, with blue representing low count values, whereas red represents high count values. A significant peak around 53.0 nS is observed from the 1D histogram in Figure 32a, which indicates a dominant geometry between the molecules and the electrodes. Figure 32b is the corresponding 2D histogram with a distribution of conductance data ranging mainly between 45 and 60 nS. A red region (high point density) observed in the 2D histogram at the base of the 2D plot corresponds to the normal decay of the current, while the red region around 45−60 nS represents the distribution of current plateaus corresponding to molecular junctions. These values are consistent with the formation of molecular junctions for this molecule (Figure 32b).

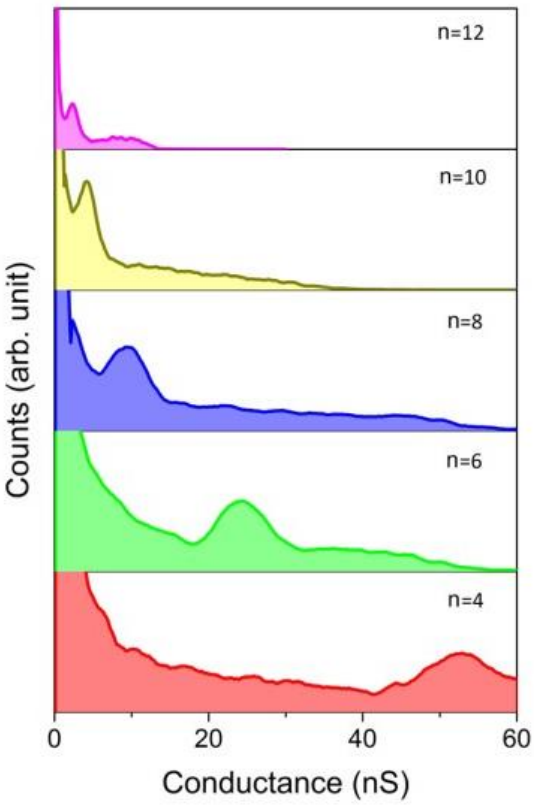

Figure 33. Stacked conductance histograms for gold−n-alkanedithiol−graphene hybrid junctions in which n = 4 (red), 6 (green), 8 (blue), 10 (yellow), and 12 (magenta).

Figure 33 presents conductance histograms of 1,n-alkanedithiol (n = 4, 6, 8, 10, 12) with the same conductance and counts scale. A single main peak dominates each of these plots, and this indicates the respective conductance values for each molecular junction. We found the conductance values of 1,4-butanedithiol (red), 1,6-hexanedithiol (green), 1,8-octanedithiol (blue), 1,10-decanedithiol (yellow), and 1,12-dodecandithiol (magenta) to be 53.0, 24.3, 9.2, 4.2, and 2.3 nS, respectively (the corresponding 1D and 2D histogram with the Gaussian fit of each molecular junction are shown in the Appendix A1).

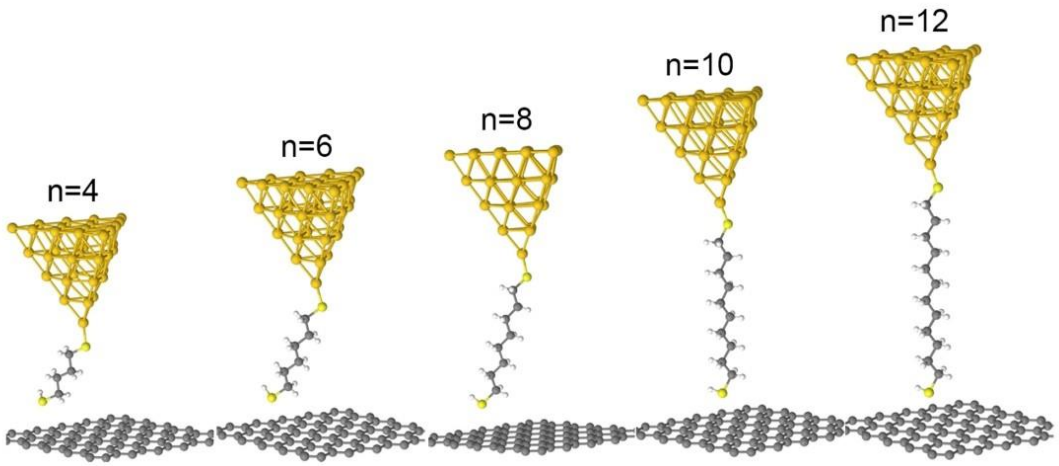

Figure 34. DFT-optimized model junctions used for the conductance calculations.

Also in parallel, we have calculated the theoretical conductance using a combined DFT and Keldysh−Green function formalism (Figure 34). In general, there is a good agreement between theoretical and experimental results despite some discrepancies in the overall behavior of the conductance, which can be attributed to different structural optimizations of the molecular junctions. Also, it is likely that many configurations are experimentally sampled in the stochastic junction formation process, whereas the calculations have been performed for an ideal single-molecule nanojunction. However, the general behavior compares well with experimental data. From Figure 34, we can observe that the molecular chains are oriented along the molecule−graphene axis for long chains, as expected, but present a small tilt angle for $n \leq 8$. This is probably related to a stronger tip−graphene interaction. With the shorter length of the molecule, the tip−graphene distance is much-reduced, therefore promoting more significant tip−graphene interactions, which can compress or tilt the molecule sandwiched in the junction.

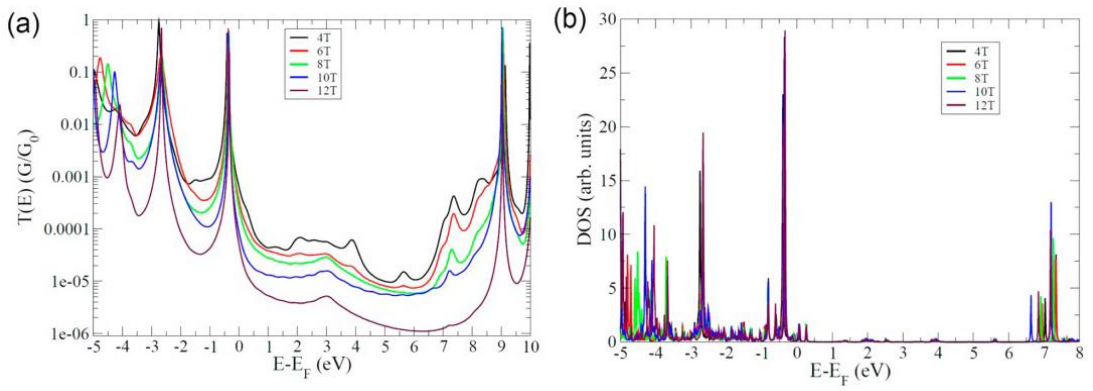

Figure 35. (a) Calculated electronic transmission T(E) of the molecular junctions for the different lengths. (b) Calculated PDOS of the molecules in the molecular junctions for different lengths. In both figures, a strong resonance appears, associated with the HOMO level, at −0.4 eV with respect to the Fermi level.

Figure 35a shows the evolution of the electronic transmission, $T(E)$, for the different molecular lengths. These transmission curves show an important peak located at around −0.4 eV below the Fermi level for each molecular junction, which corresponds to the transmission resonance associated with the HOMO level. The position of the HOMO level, as also shown in the density of states (DOS) of the junction represented in Figure 35b, is an indication of the charge transfer between the molecule and the electrode. From our calculations, we determined that the charge transfer from the S atom in the S−Au contact is around −0.26 e. This charge transfer and the corresponding interface dipole are relatively small but significant enough still to partially depopulate the HOMO level and relocate it closer to the Fermi level.

The position of the HOMO here can be analyzed with respect to the case of the symmetric gold−molecule−gold junction. It is well-known that when a thiol-terminated molecule is adsorbed on gold, there is strong charge transfer from the sulfur to gold and that, consequently, the HOMO level generally shifts toward the Fermi level (adding charges to the molecule will push the HOMO further away from the Fermi level, whereas removing charges depopulates the HOMO level, forcing it toward the Fermi level). This charge transfer is driven by an interface electric dipole pointing from the sulfur to the gold. However, in the case of a molecular junction when the molecule is connected to two gold surfaces through thiol groups, the HOMO level is known to be located around 2 eV below the Fermi level [96]. This means that the charge transfer

from the thiols to the gold surfaces is reduced, which can be interpreted as a cancellation of the two interface dipoles, which point in opposite directions, leading to an electrostatic equilibrium in the molecular junction. Now in the present case of our nonsymmetric gold−molecule−graphene junction, this equilibrium is broken. Indeed, the coupling between the thiol and the graphene is much weaker than the one between the thiol and gold due to van der Waals interactions. Therefore, the interface dipole on the graphene side is much smaller than on the gold side, meaning that the thiol−graphene dipole does not compensate the thiol−gold dipole. Thus, we recover a situation similar to the standard adsorption of a thiol terminated molecule on a gold surface, with a significant charge transfer at the thiol−gold interface, causing the HOMO level to move closer to the Fermi level. This is the reason why we obtain a HOMO level and consequently a peak in the transmission at around −0.4 eV with respect to the Fermi level.

As the length increases, the molecular gap gets smaller leading to a decreasing HOMO − Fermi level energy difference. Notice that the difference between n = 8 and n =10 is not so clear, probably due to the change of molecular conformation, from a tilted to a straight arrangement. As a remark, some small artifacts appear in the DOS due to the coupling with the gold electrode. As an atomic cluster, the gold tip presents many surface states that will couple with the molecule, which leads to the emergence of several peaks in the DOS. These peaks are not present in the electronic transmission because the coupling to the bulk electronic reservoirs removes these negligible contributions.

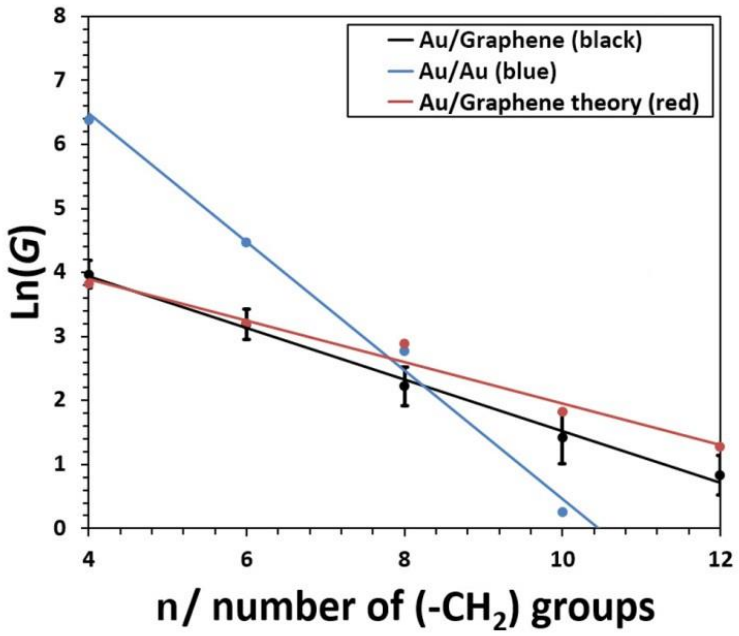

Figure 36. Natural logarithmic plot of the conductance as a function of the number of CH_2 groups. The red line represents the theoretical values, the black line is experimental data for Au−molecule−graphene junctions, and the blue line is the literature data for Au−Molecule−Au junctions.

The results show a clear decrease in the single molecular conductance with the addition of methylene (−CH_2) units to the molecules. This phenomenon can be explained by a superexchange mechanism. The exponential conductance decay with the number of molecular units is expressed by $G = A \exp(-\beta_n n)$, where G is the conductance; A is related to the nature of molecule−electrode interaction, which reflects the contact resistance; βn is the decay constant, which describes the efficiency of electron transport through the molecules; and n is the number of methylene groups [44,97]. To investigate the relationship between molecular length and conductance, a linear fitting of the natural logarithmic single-molecule conductance versus the number of (−CH_2) units per molecular junction was plotted, and a decay constant $\beta_n = 0.40$ was obtained from the slope in Figure 36. Besides the experimental conductance values, the theoretical decay constant is estimated to be around $\beta_n = 0.32$, in good agreement with the experiments, confirming the importance of the molecule− graphene interface on the electronic transport.

Many literature studies have been performed to measure the single-molecule conductance and investigate the decay constant of gold−alkanedithiol−gold systems. For example, Marita and Lindsay measured the conductance of 1,n-alkanedithiol (n = 8, 10, 12) compounds using CP-AFM, with conductance values of 16.1 ± 1, 1.37 ± 0.35, and 0.35 ± 0.04 nS found, respectively [30]. Based on STM-BJ measurements, Li et al. have reported conductance values for 1,n-alkanedithiols of 19.4 (n = 8) and 1.6 nS (n = 10), for example [52]. In general, the decay constant (β_n) ranges from 0.8 to 1.0, measured by either STM-BJ or CP-AFM technologies [30,36,52]. Although the general trend of the conductance decay with molecular length is qualitatively similar in metallic and hybrid junctions, the comparison of absolute conductance values of these two junction types is not straightforward, which is mainly due to the change of electrodes. This difference can be explained using a simple barrier tunneling model, which considers the relationship between the decay and the barrier height at the molecule−electrode interface [23]: $\beta_n = 2d_0\sqrt{(2m\phi)/\hbar}$., where d_0 is the unit length between the monomers in the molecule, m is the mass of the electron, and φ is the barrier height. The latter is given by the energy difference between the Fermi level and the HOMO level of the molecule in the present case. In the case presented here, with our nonsymmetric junction between gold and graphene, the theoretically determined values are $\varphi \approx 0.4$ eV (see the DOS in Figure 35b) and $\beta_n = 0.4$. In the case of a symmetric gold junction where φ is significantly higher at ~2 eV [96], the corresponding β value would be $\beta_n = 0.4\sqrt{(2/0.4)} = 0.4\sqrt{5} = 0.9$, in good agreement with experimental observations. This simple reasoning shows that our findings are in good agreement with previous observations for Au−alkanedithiol−Au junctions. The contact resistance can be determined from the intercept of the linear fits in Figure 36 by extrapolating the fits of literature (blue line) [30], our experiments (black line), and theory (red line) to zero length, and the resistance values found are ~27, ~5000, and ~3900 kΩ, respectively. This shows that the contact resistance of Au−molecule−graphene junctions is much higher than for the Au−molecule−Au junctions. This difference indicates that the coupling between molecules and electrodes

is rather weak at the graphene−molecule interface, which is in a good agreement with our theoretical interpretation above. The relatively small degree of electronic transfer at the graphene interface, in which the alkanedithiol donates a small partial electronic charge to the graphene surface, leads us to suggest that the binding at this interface is primarily related to a van der Waals coupling [98].

It is useful to compare our results to those in which large area graphene contacts have been deployed. For example, Cao et al. have used graphene electrodes to create "robust and identical molecular transport junctions" using a lithographic method [72]. To further prove the effectiveness of their junctions, they capped molecules with amino groups to construct graphene−molecule−graphene symmetric junctions, which showed excellent reproducibility and stability. In addition, graphene− molecule−graphene symmetric molecular junctions were formed to create devices with electronic functionality (for example, reversible conductance switching based on graphene−azobenzene junctions) [99]. The replacement of the gold electrode to construct a symmetric graphene−molecule−graphene junction changes the coupling strength between the molecules and electrodes [100]. In our present study we find that the bonding strength between graphene and thiol groups is relatively weak, and the interface resistance is much higher in comparison with that of the gold and thiol coupling. Thus, in graphene−alkanedithiol−graphene symmetric junctions, the resistance would be higher, giving a lower conductance than graphene−gold nonsymmetric junctions. It is therefore important to consider the nonsymmetric nature of the graphene−molecule−gold junctions and the complete junction electronic properties when comparing them to symmetric graphene−molecule−graphene junctions.

In the case of a symmetric gold−molecule−gold junction, the system tends to reach an electrostatic equilibrium where little charge transfer is observed, as explained earlier in the DOS analysis. However, in a nonsymmetric junction, substantial charge transfer is observed at the metallic electrode−molecule interface, which leads to a relocation of the HOMO closer to the Fermi level. In this case, there is large dipole at the gold−molecule interface that is not compensated at the graphene interface. Consequently, much-smaller attenuation of the current along the molecular wire is

obtained. This effect is mainly due to the weak coupling at the molecule−graphene interface, which excludes any significant charge transfer at this interface.

Indeed, the effect of graphene is mainly to decouple the molecule from the second electrode and to favor a stronger charge transfer at the S−Au interface, hence relocating the HOMO level near the Fermi level. In this case, the effect is less due to the electronic properties of graphene than to the weak coupling associated with van der Waals interactions. Consequently, the combination of a weak coupling at the bottom graphene electrode with a strong coupling and high charge transfer at the top metallic electrode opens perspectives for controlling charge transfer and attenuation factors of single molecule junctions.

3.4 Conclusion

In summary, we have systematically studied using an STM based technique the single-molecule conductance of 1,*n*-alkanedithiols (n = 4, 6, 8, 10, and 12) using graphene bottom and gold top electrodes. The conductance decays exponentially with the number of methylene groups with a decay constant of 0.40, much lower than the value obtained with a second metallic contact. Theoretical computations of the junction conductance values were also performed to investigate the electrical properties as a function of molecular length. These results show that the decay is related to the junction electronic structure, the nonsymmetric contact, and the weak coupling at the molecule−graphene interface, leading to a stronger charge transfer at the gold electrode−molecule interface. This work suggests that novel nonmetallic 2D materials could serve as promising electrodes to construct nonsymmetric junctions with tunable attenuation factors and electrical signatures, which differ from those of equivalent symmetric junctions with metal contacts.

4 Chapter 4: Effect of Anchoring Groups on Single Molecule Conductance in Graphene Based Molecular Junctions: Comparative Study of Thiol- and Amine- Terminated Molecules

4.1 Preface

The research work in Chapter 4 was carried out in collaboration with the theoretical simulations made by the group of Dr. Yannick J Dappe (CEA, CNRS, France). I will present my experimental work on the construction of the gold−n-alkanediamine−graphene asymmetric junction and the related measurement of the charge transport properties. The results presented in this chapter were published and reproduced with permission from *J. Phys. Chem. Lett.* **2017**, *8*, 5987−5992 (DOI: 10.1021/acs.jpclett.7b02822), with the title 'Symmetry Effects on Attenuation Factors in Graphene-Based Molecular Junctions'. Copyright 2017, American Chemical Society. This study was designed by Richard J. Nichols, Li Yang and Cezhou Zhao. I carried out the main experimental work on the conductance measurement and data analysis plus writing the first draft of the manuscript. Alexander Smogunov and Yannick J. Dappe conducted the simulation work. The manuscript was then corrected by Yannick J. Dappe, Richard J. Nichols, and Li Yang. The rest of authors conducted some other supporting works, for example, the data analysis, discussion and double check the experimental results.

We have demonstrated the unique structural and electronic characteristics of graphene material to serve as a bottom electrode to construct carbon based junctions in Chapter 3. Since the nature of molecules will strongly influence the charge transport properties of the junction, it is thus very important to elucidate the role of molecules with different anchoring groups in graphene based junctions. With this in mind, we have probed here the electrical conductance of a molecular junction based on α,ω-diaminoalkane chains sandwiched between a gold and a graphene electrode. This result is also compared with the junctions bridged with thiol-terminated molecules. STM based *I*(*s*) method combined with density functional theory-based transport calculations are used in this study, we demonstrate that the resulting attenuation factor turns out to

be much lower when compared to the standard molecular junction between two gold electrodes. This effect is attributed to asymmetric coupling of the molecule through strong chemisorption at the gold electrode and weaker van der Waals contact at graphene. Moreover, this asymmetric coupling induces higher conductance than that in the same hybrid metal−graphene molecular junction using standard thiol anchoring groups.

I will also provide an overview here about the interpretation of the decay and conductance values in gold-alkanediamine-graphene nonsymmetric junctions. The obtained decay value (0.37) is very similar to the alkanedithiol chains (0.40) and again much smaller than the one obtained in the case of a symmetric gold−gold molecular junction (0.88). From the DFT calculation, the HOMO level of the alkanediamine case is much farther from the Fermi level, −3.5 eV, than that in the alkanedithiol case (−0.4 eV). Considering the similar decay values, it is not sufficient to explain the low attenuation by the use of a simple barrier tunneling model (β_n ~ barrier heright). Hence, the attenuation factor of the diamine case is not only determined by the interface properties but also by the electronic properties of the isolated molecule. From the HOMO orbitals of the dithiol and diamine, the conductance along the chain is much more favored in the case of the diamine molecule compared to that in the dithiol case due to the symmetric factors of the molecules. We also observed the significant HOMO level shift (-5.5 to -3.5 eV) in the alkanediamine case, which is similar to the dithiol case (-2 to 0.4 eV). Thus, the attenuation factor of the junction is determined by the balance between E_F-E_{HOMO} (interface properties) and the propagation along the molecular chain (isolated molecular properties). For the diamine case, although the tunnelling barrier at the interface is relatively high, the charge transport along the molecular chain is relatively high as well. There are two factors for the unexpected conductance behaviour of the alkanediamne junctions compared to alkanedithiol ones. The first factor is related to the conductance along the chain being much favoured in the case of diamine as described above. The second one is the properties induced by the breakage of the junction symmetry.

4.2 Introduction

Single-molecule junctions (MJs) constitute elementary units in molecular electronics, and understanding their electrical transport properties continues to be a leading issue in molecular electronics [72]. The transport properties of molecular junctions are related to many factors such as molecular length, contact binding properties, and electronic level alignment between molecules and electrodes [34,101]. The concerted development of techniques like mechanically controlled break junctions (MCBJs) [10], scanning tunneling microscopy break junctions (STM-BJs) [11], conductive probe atomic force microscopy (CP-AFM) [12] and the $I(s)$ technique based on STM [13] has given much impetus to the field of molecular electronics. A plethora of studies have been performed to examine the specific role of electrode materials and anchoring groups of molecular wires [102]. To date, thiol has been the most widely studied anchoring group due to its strong covalent bond with gold contacts [51,88], although many other groups forming weaker chemisorption bonds such as pyridyl and amine have also been effective [11,104]. In our previous works [91,105], we investigated the possibility of using a graphene electrode to form hybrid metal−molecule−graphene junctions by the use of thiol anchoring groups [105]. We observed a reduction of the length attenuation factor of the tunneling current (the so-called β-factor) of the molecular junction (by a factor of almost 2) with respect to standard gold−alkanedithiol−gold junctions [105]. In this case, there is a stronger electronic dipole at the S−Au interface than at the SH−graphene interface, which leads to an important shift of the HOMO level toward the Fermi level of the system. The lower attenuation can then be attributed among other effects to the strong molecular level alignment at the gold interface, which results in better conductance for hybrid molecular junctions above ∼1 nm molecular length, with respect to standard symmetric junctions with two gold contacts. This result offers promising perspectives for graphene contacts for molecular junctions.

Here, we investigate further these hybrid junctions by considering a different anchoring group. So far, many anchoring groups have been studied for molecular junctions employing metallic electrodes like amine ($-NH_2$) [106], carboxylic acid

(−COOH) [49], isocyanide (−NC) [107], dimethyl phosphine ($-PMe_2$) [108], methyl sulfide (−SMe) [46], and selenol (−SeH) [109] groups. Comparisons between these different anchoring groups have also been made. In particular, Chen et al. studied the effect of thiol, amine, and carboxylic acid anchoring groups on single molecule conductance [44]. The contact resistance to gold of these anchoring groups varies in the order of thiolate (−SH), amine ($-NH_2$), and carboxylate (−COOH), attributed to different electronic coupling efficiencies between the molecule and electrodes. It can also be noted that the bonding patterns of these three anchoring groups are different: thiolate forms a strong covalent bond with gold, while the binding for gold and amine-terminated alkane is significantly weaker, and carboxylic acid groups are likely to deprotonate to the carboxylate in order to coordinate to gold electrodes. Also, the symmetry of the bonding orbitals at the interface and on the molecular backbone plays an important role in the conductance properties. For example, it has been shown recently that orbital symmetry mismatching can reduce drastically the molecular conductance or even filter the spin of the current through the junction [110-111].

Here we show in a combined experimental and theoretical study that the electronic conductance in a hybrid gold−graphene diaminealkane molecular junction presents a much smaller attenuation factor with respect to the standard gold−gold junction. The system has been investigated using an STM based $I(s)$ technique and theoretical calculations based on density functional theory (DFT) and a Keldysh−Green formalism. These computations reveal that the symmetry breaking induced by the graphene electrode is responsible for the low attenuation.

4.3 Results and discussion

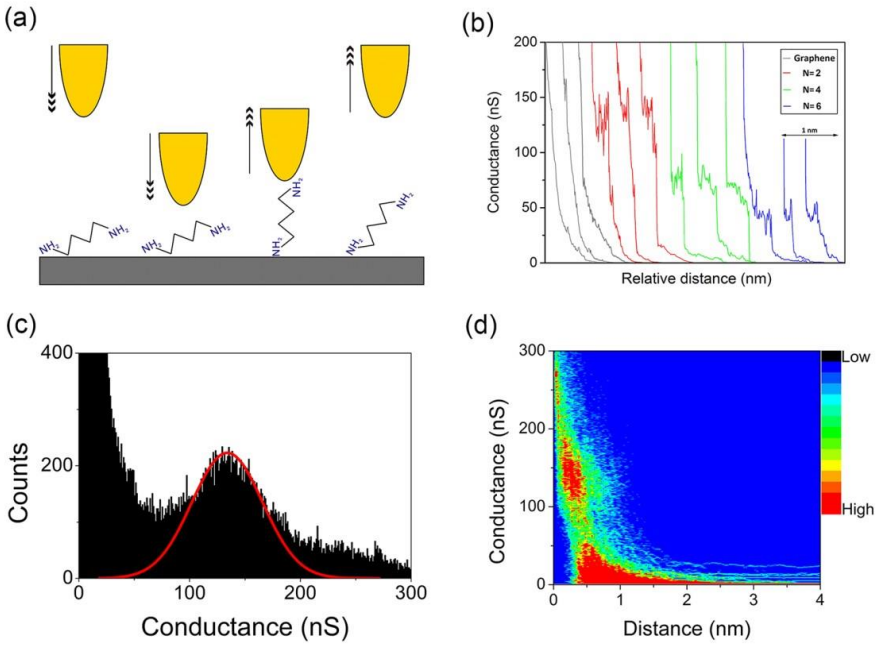

Figure 37. (a) Schematic diagram of the STM-based *I*(*s*) technique. (b) Typical *I*(*s*) curves of bare graphene (gray), gold−1,2-ethanediamine−graphene junctions (red), gold−1,4-butanediamine−graphene junctions (green), and gold−1,6-hexanediamine−graphene junctions (blue). (c) 1D histogram of single-molecule conductance of gold−ethanediamine−graphene hybrid junctions with a Gaussian fit. (d) Corresponding 2D histogram with a sensitivity indicator of the conductance counts.

Typical conductance curves for 1,n-alkanediamine (n = 2, 4, 6) are shown in Figure 37b. The gray curves indicate the fast exponential decay of conductance as a function of the distance between the tip and the graphene when no molecular junctions are formed. For the red (n = 2), green (n = 4), and blue (n = 6) curves, the conductances decrease in a stepwise fashion, providing evidence for molecular junction formation. For example, the conductance of gold−1,2-ethanediamine−graphene hybrid junctions is located at around 120−160 nS.

In Figure 37c, a clear peak is observed in the 1D histogram for gold−1,2 ethanediamine−graphene nonsymmetric junctions. Using a Gaussian fit of this peak, a conductance value of 137 nS is obtained. The corresponding 2D histogram shown in Figure 37d represents the data distribution of conductance values and the length of the molecular junction. A red region (high data point count) located at around 120−160 nS is clearly observed in the 2D histogram, which is consistent with the peak in Figure 37c and the plateaus shown in Figure 37b.

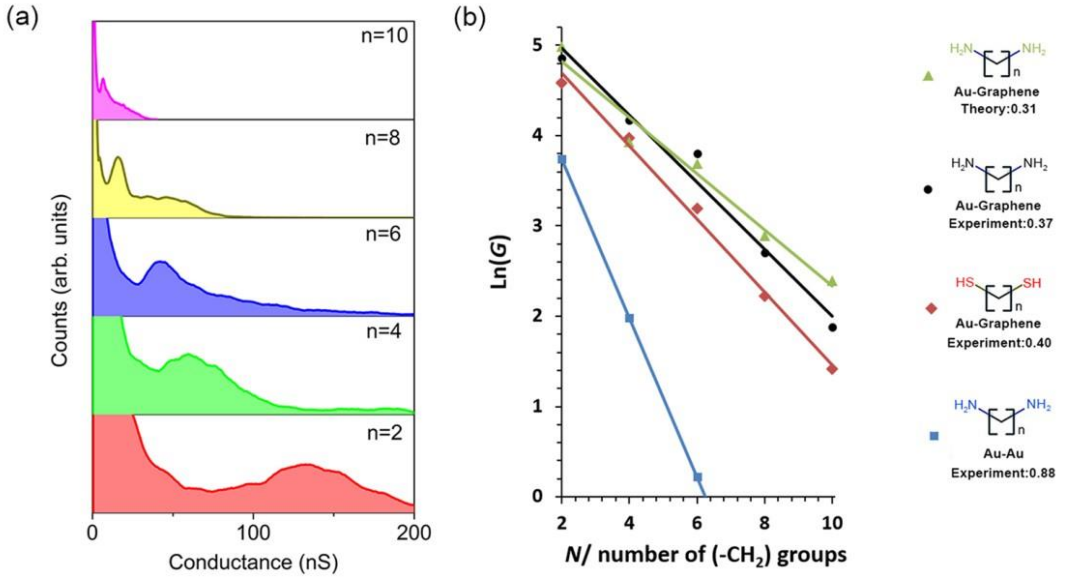

Figure 38. (a) Conductance histograms for gold−n-alkanediamine−graphene nonsymmetric junctions in which n = 2 (red), 4 (green), 6 (blue), 8 (yellow), and 10 (magenta). (b) Natural logarithmic plot of the conductance as a function of the number of CH_2 groups. The green (black) lines represent the theoretical (experimental) decay values of gold−diamine-terminated alkanes−graphene junctions. The red line is the experimental gold−dithiol-terminated alkanes−graphene junction. The blue line with a higher decay constant stands for the gold−diamine-terminated alkanes−gold symmetric junction.

To better illustrate the progression of conductance with molecular length, we plotted a stacked 1D histogram of 1,n-alkanediamine (n = 2, 4, 6, 8, 10) with the same conductance and counts scale (Figure 38a). For each conductance histogram, only one single peak dominates. Detailed 1D and 2D histograms of 1,n-alkanediamine (n= 4, 6, 8, 10) are presented in the Appendix A2. The description of the experimental details including the preparation of the molecular solution (diamine-terminated alkanes−methanol, 1:20, v/v) and substrate can be also found in the Chapter 2.

Table 3. Conductance Values and Tunneling Decay Value (β Value) for Au−Molecule−Graphene Nonsymmetric Junctions and Au−Molecule−Au Symmetric Junctions[a]

molecular junctions	conductance (nS)					tunneling decay value (β_n)
	n=2	n=4	n=6	n=8	n=10	
gold-n-alkanediamine-graphene	137	65	42	15	7	0.37
gold-n-alkanediamine-graphene (theory)	147	51	40	18	11	0.31
gold-n-alkanediamine-gold (literature)	42	7.3	1.2	-	-	0.88(LC)[44]
gold-n-alkanedithiol-graphene	98	53	24	9	4	0.40
gold-n-alkanedithiol-graphene (theory)	152	46	25	18	6	0.32
gold-n-alkanedithiol-gold (literature)	-	-	28.2	3.9	0.2	1.08(LC)[44,36]

As expected, the conductance values decrease with the molecular length for each series of molecules. Table 3 summarizes the experimental and theoretical conductance values as well as the decay constant of diamine-terminated compared to dithiol-terminated alkane analogues for nonsymmetric gold−molecule−graphene junctions [105]. We also list the literature conductance values (lower conductance group) of gold−gold symmetric junctions for comparison.

For short molecular junctions, the general conductance behavior is now well described as nonresonant tunneling. This regime predicts an exponential decrease of the conductance with the molecular length, while a weaker length dependence for longer molecular lengths [63] is generally attributed to hopping-type mechanisms. Hence, the conductance follows $G = A_n \exp(-\beta_n N)$, where G is the conductance, A is related to the nature of molecule−electrode interaction, reflecting the contact resistance, β_n is the decay constant, which describes the efficiency of electron transport through the molecules, and N is the number of methylene groups [97].

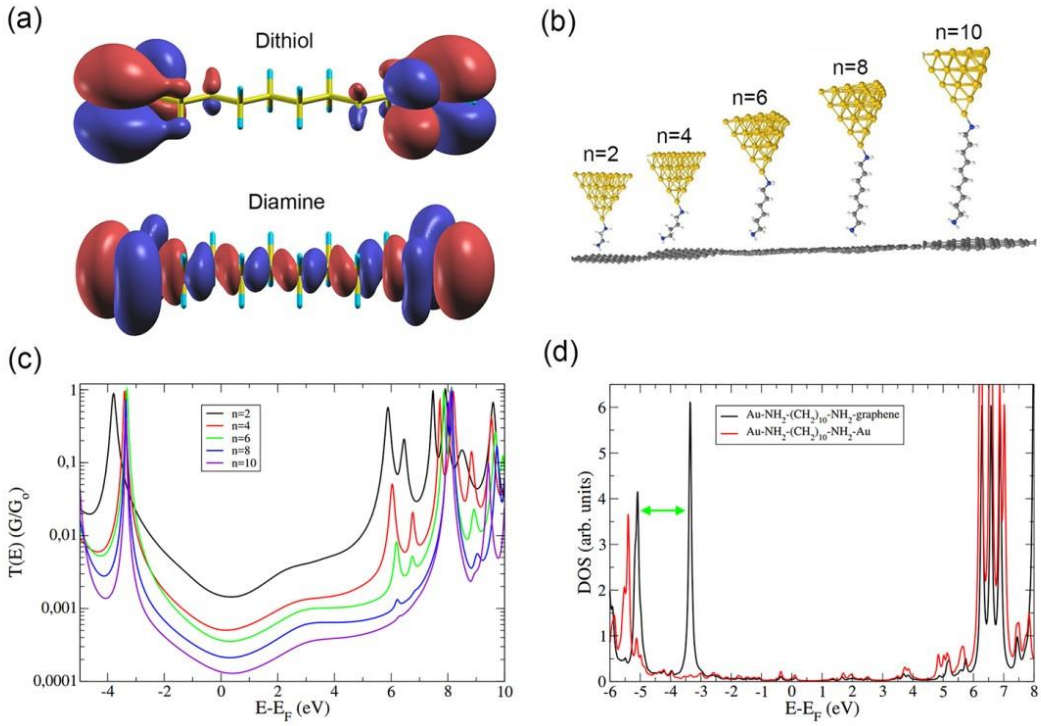

Figure 39. (a) HOMOs for dithiol and diaminealkane chains. Isosurfaces of positive (negative) isovalues (the same for both molecules) are shown in red (blue). (b) DFT optimized model junctions used for the conductance calculations. (c) Calculated electronic transmissions $T(E)$ of the molecular junctions for different lengths. (d) Comparison of the DOS of the n = 10 alkane chain in a gold−gold or a gold−graphene molecular junction.

From the natural logarithmic plot of the conductance versus the number of ($-CH_2$) units in Figure 38b, we found β_n = 0.37 for diamine-terminated alkane chains. This value is very similar to the one obtained in our previous work on alkanedithiol chains [91] and again much smaller than the one obtained in the case of a symmetric gold−gold molecular junction [104]. To understand the mechanism at the origin of this strong attenuation factor reduction, we have performed DFT calculations to model the system. The same procedure as the one for alkanedithiol chains has been applied here. Figure 39b represents the DFT-optimized molecular junction transmission curves. Using a Keldysh−Green formalism, we have calculated the electronic transmissions represented in Figure 39c. More details on the theoretical procedure can be found in ref 105. Here, the HOMO lies much closer to E_F, implying that HOMO-mediated hole tunneling would be the predicted mechanism. However, this HOMO position is markedly different for the alkanediamine compared with our previous work on alkanedithiols. In

the alkanediamine case Figure 39b, the transmission shows that the HOMO level is much farther from the Fermi level, at −3.5 eV, than that in the alkanedithiol case, where it was located at −0.4 eV. Consequently, the use of a simple barrier tunneling model here, where $\beta_n = 2d_0\sqrt{(2m\phi)/\hbar}$., is not sufficient to explain the low attenuation of the molecular junction. Hence, the attenuation factor is not only determined by the interface properties but also by the electronic properties of the isolated molecule. In this respect, we present in Figure 39a the HOMO wave functions for the dithiol chain (top) compared to those of the diamine (bottom).

From Figure 39a, it is clear that the (doubly degenerate) HOMO orbitals present a strong dependence on the anchoring groups. However, while for the dithiol case the HOMO orbital is strongly localized on sulfur atoms, it spreads significantly into the backbone chain for the diamine case. This striking difference in HOMO spatial localizations stems from their different symmetries with respect to a mirror plane passing horizontally through the molecule. Namely, the HOMO is an odd (even) function for dithiol (diamine) chains (Figure 39a). Also, the lowest-decay states in a gap of alkane chains are the σ-like states of even symmetry [112] (originating mainly from carbon p_z orbitals, z being the molecular axis). These states correspond to the evanescent wave functions through the gap of the "free" alkane chain (without anchoring groups or connection to an electrode, i.e., the molecular backbone) and support electronic transport through the molecular junction [112]. In an electronic transport process, the electrons are injected into those states through the HOMO or LUMO orbitals associated with the anchoring groups of the molecular junction. That would result in perfect symmetry matching between those states and the diamine HOMO orbital, leading to long penetration into the molecule. The odd HOMO orbital of the dithiol chain must be matched with odd evanescent states of the alkane chain, which have a much stronger decay rate in the gap region. Therefore, we can deduce that the conductance along the chain is much more favored in the case of the diamine molecule compared to that in the dithiol case. This feature has been illustrated theoretically in recent work on methyl sulfide-terminated alkane chains [113]. Notice

that similar reasoning can be performed on the same molecule connected to the gold and graphene electrodes. This feature is represented in Appendix A3, where we have considered the isoelectronic density of states (DOS) at the Fermi level. Indeed, the HOMO level strongly hybridized with the electrodes (in particular, at the gold−molecule interface) makes the symmetry interpretation more complicated. Moreover, due to this strong hybridization and the resulting induced DOS in the gap, the current has to be considered at the Fermi energy. The delocalization still remains more important for the diamine case (Appendix A3), as predicted by the symmetry analysis in the isolated molecule.

Additionally, molecular conductance is often attributed to the frontier orbitals in the molecule, which corresponds to the electronic states of the "free" alkane chain, or molecular backbone. However, we have noticed in our calculations that the frontier orbitals of the molecular backbone are not modified by the anchoring groups or the electrode nature. Therefore, we can state that the current attenuation is ruled by the HOMO level of the full molecular junction (combining molecular backbone and anchoring groups), strongly dependent on the anchoring groups and its delocalization through the molecule. This has been also demonstrated through molecular complex band structure calculations by Sankey et al. [114] where there is no difference observed with the anchoring groups.

From those symmetry arguments and because dithiol and diamine molecular junctions present the same attenuation factor when connected to two gold electrodes, we can expect an interplay between a higher tunneling barrier at the interface and better molecular conductance in the diamine case. However, a theoretical determination of the tunnel barrier in this molecular junction explaining formally the relationship between the attenuation factor, the interface barrier, and the conductivity in the molecular backbone is more complicated to establish and is beyond the scope of the present work.

Now we represent in Figure 39d a comparison between the DOS of diamine molecular junctions based on gold−gold or gold−graphene electrodes. The gold−alkanediamine−gold junction presents a HOMO level at around −5.5 eV from the gold Fermi level (E_F), which is much farther from E_F than values found in the literature

for the dithiol case under the same conditions (around −2 eV). Consequently, a similar attenuation factor obtained for the dithiol and diamine junctions in the gold−gold configuration is indeed explained by the interplay between an interface barrier related to the HOMO level (which is smaller in the dithiol case) and the conductivity along the molecular chain, which is related to HOMO level propagation along the molecule (which is larger in the diamine case). Considering the DOS of the gold−graphene junction in Figure 39d, we can observe that the HOMO peak appears much closer (by about 2 eV closer than that for Au−Au junctions) to the Fermi level, at about −3.5 eV, as indicated by a green arrow. This is a consequence of very asymmetric coupling of the molecule to two different electrodes. On the gold side, the bonding is covalent, whereas on the graphene side, the bonding is much weaker due to van der Waals interactions. This asymmetry is at the origin of a sharp HOMO resonance (spatially distributed around the graphene-side N atom) appearing for the gold−graphene diamine chain. This significant HOMO shift presents important consequences for the molecular junction conductance. The new tunnel barrier is reduced from −5.5 to −3.5 eV, which is similar to the reduction found previously for the dithiol case, from around −2 to −0.4 eV [111]. Because the attenuation factor is the same between the two types of molecular junctions in the gold−gold case, a similar shift induced by asymmetric connection will result in a much smaller attenuation factor for both molecules in the gold−graphene geometry.

Both experimental and theoretical results produce unexpected behavior of the alkanediamine junctions compared to alkanedithiol ones. Results in the literature [36,44,93] show higher conductance for alkanedithiol with respect to alkanediamine molecular junctions using gold electrodes, while we find here opposite behavior when one gold contact is substituted for a graphene one. Indeed, a systematically higher conductance for diamine chains is obtained. Moreover, the effective contact resistance can be estimated for both chains by extending the linear fits to zero methylene groups. This results in a contact resistance for the thiol compounds of 3900 kΩ, which is slightly higher than the one for diamine analogues (3700 kΩ). This small difference can be interpreted in terms of coupling to the electrode. These couplings are expected to be

modified because the gap between the gold Fermi level and the HOMO is reduced by about 2 eV in both cases as a result of the HOMO resonance shift, while there is no change in the LUMO level energy. These couplings vary as the inverse of the gap through self-energy calculations and are therefore increased by the gap reduction. Consequently, the conductance of the junction is strongly enhanced, which explains the slightly higher conductance of the gold−alkanediamine−graphene junction with respect to the gold−alkanedithiol−graphene junction where the gap remains unchanged with respect to the gold−gold case.

4.4 Conclusion

In summary, we have studied the conductance of alkanediamine molecular junctions using an STM-based technique, with a gold electrode at one end of the junction and a graphene electrode at the other. We have obtained a similar attenuation factor to what was obtained previously in the case of alkanedithiol junctions due to the asymmetric coupling of the diaminealkane molecular chain between gold and graphene. The weak coupling at the graphene interface is responsible for a significant HOMO molecular level shift toward the Fermi energy. This shift reduces the tunneling barrier at the interface in the same way as that for the dithiol case, which provides justification for the similarity in the attenuation factors. A slightly higher conductance of the diamine hybrid junction with respect to the dithiol hybrid junction is also found. These experimental results are supported by theoretical computation and symmetry considerations for the molecular junctions. These findings lead us to expect a general reduction of the attenuation factor for hybrid gold−graphene molecular junctions with different anchoring groups, with respect to standard gold−gold junctions. This work highlights the attractive features of graphene contacts in molecular electronics, which might inspire their future deployment in new device prototypes.

5 Chapter 5: Effect of Measuring Techniques on Electrical Properties in Graphene Based Junctions: Comparative Study of STM BJ, STM based *I*(*s*) and CP-AFM BJ Techniques

5.1 Preface

In previous chapters, we have demonstrated the possibilities of constructing non-metallic molecular junctions and the corresponding charge transport properties through gold-alkanedithiol/alkanediamine-graphene junctions by the *I*(*s*) technique. Here, we present an experimental study which focuses on comparing methods for capturing and measuring the electrical properties of single molecules in gold−graphene contact gaps. The results presented in this chapter were published and reproduced with permission from *J. Phys. Chem. C* **2018**, *122*, 23200–23207 (DOI: 10.1021/acs.jpcc.8b08196), with the title 'Technical Effects of Molecule−Electrode Contacts in Graphene-Based Molecular Junctions'. Copyright 2018, American Chemical Society. This study was designed by Richard J. Nichols, Li Yang and Cezhou Zhao. I carried out the main experimental work on the application of CP-AFM BJ method, conductance measurement and data analysis plus writing the first draft of the manuscript. The manuscript was then corrected by Yannick J. Dappe, Richard J. Nichols, and Li Yang. The rest of authors conducted some other supporting works, for example, the data analysis, discussion and double check the experimental results.

We have attempted to measure the single-molecule conductance of a series of 1,n-alkanedithiols (n = 4, 6, 8) tethered between a gold and a graphene contact with three different methods. The conducting probe atomic force microscopy break junction (CP-AFM BJ), scanning tunneling microscopy (STM) break junction (STM BJ), and STM-based *I*(*s*) techniques for forming molecular junctions with graphene lower contacts were compared. In each case, the upper contact was gold, with a gold-coated AFM probe in the CP-AFM BJ method and a gold STM tip for both the STM BJ and *I*(*s*) techniques. Both the CP-AFM BJ and the STM-based *I*(*s*) methods yielded similar values for the conductance decay constant values, with $\beta_N = 0.56$ and 0.40, respectively. In line with previous observations, these are much smaller than values recorded for the

same alkanedithiol series in symmetric gold−molecule−gold junctions, where we find that $\beta_N = 1.1$. This clearly shows the impact of substituting one of the gold contacts for a graphene one. This observation has been previously rationalized as resulting from the breaking of the junction symmetry, the change in electrode−molecule coupling and energy level alignment. On the other hand, stable molecular junctions could not be formed using the STM BJ technique with graphene contacts, which may be because of transient instability in the gold tip contact after it has been pushed hard onto the graphene surface.

5.2 Introduction

Investigating the nature of charge transport through molecules tethered between pairs of electrode contacts is one of the most active areas of contemporary molecular electronics [115]. A range of factors can influence the electrical characteristics of such molecular junctions, including the intrinsic properties of molecules and electrode materials, the external environment, the molecule−electrode binding, or molecular orbital alignment in relation to the Fermi levels of the electrodes [116]. To date, the most widely used techniques for probing the electrical properties of molecular junctions include mechanically controlled break junctions [10], scanning tunneling microscopy based break junctions (STM BJ), the *I*(*s*) technique [11,13] and conducting probe atomic force microscopy (CP-AFM) [12,26]. Originally introduced by Xu and Tao in 2003 [11], the STM break junction (BJ) method creates in situ a metallic gold-to-gold junction between the gold STM tip and the gold substrate in the presence of a solution of the target molecule or an adsorbed layer on the gold substrate. Upon withdrawal of the STM tip, the metallic junction is cleaved, leaving a gap into which the molecular target can adsorb and form a gold−molecule−gold junction. During the process of tip withdrawal, a conductance step near the so-called quantum conductance (G_o) is observed as the metallic contact is cleaved. This is followed on further tip retraction by a smaller conductance step as the molecular junction is subsequently broken. The tip is repeatedly cycled into and out of the contact with the gold substrate, and conductance histograms are recorded from many junction formation and breaking cycles to reveal peaks corresponding to the junction conductance.

Similar to the STM BJ method, the *I*(*s*) technique [13] also employs an STM tip to form the molecular junctions which are also extended until they cleave. A similar procedure of repeatedly forming and breaking junctions is also followed, and the molecular conductance is also determined by statistical analysis and histogram construction from a large number of such traces. The key difference between the STM BJ and *I*(*s*) methods lies in the fact that for the latter technique, the tip is brought very close to the substrate surface, but direct metallic contact is avoided. As such, the *I*(*s*) technique has been referred to as a “noncontact method”. It is also worth mentioning

here the STM "Touch-to-Contact" method, in which the STM tip is positioned just in contact with the top of the molecular monolayer film. As described by Martin et al., the separation between the STM tip and the substrate is determined through a calibration procedure which relates the STM set-point parameters to an absolute tip-substrate separation [29]. The STM "Touch-to-Contact" avoids both incursion of the tip into the molecular monolayer film or a gap between the top of the monolayer and the STM tip.

CP-AFM can also be used to determine the electrical characteristics of metal|molecule|metal junctions. Typically, the CP-AFM technique uses a conducting AFM probe to contact with a self-assembled molecular monolayer (SAM) on a metal substrate [26]. The AFM feedback loop controls the force loaded onto the surface, while the current−voltage ($I-V$) relationship of the molecular layer sandwiched between the tip and surface is recorded. This is not a single-molecule determination because the area probed depends on the tip geometry, contacting force, and deformation properties of the monolayer, but typical conditions for SAMs may result in tens or hundreds of molecules being contacted [26]. CP-AFM may also be used to probe single-molecule junctions by using the technique developed by Cui and Lindsay [12,30], in which gold nanoparticles are adsorbed on-top of SAMs of monothiols containing a small concentration of dithiols, which electrically wire the nanoparticle to the surface. Touching the top of such gold nanoparticles with the CP-AFM tip then enables $I-V$ characteristics of the molecular junction to be recorded [30]. Another way to form single molecule junctions by CP-AFM is the CP-AFM break junction (CP-AFM BJ) approach. In this method, the conducting AFM tip is brought into contact with the surface covered by the molecular target. The AFM tip is then rapidly retracted while monitoring the current and force signals [117-118]. As for the STM BJ and $I(s)$ methods, during such formation and retraction cycles, molecular junctions can be formed and cleaved and traces analyzed to extract single molecule data following a similar statistical analysis.

The techniques mentioned above share the basic concept of being able to capture single or small groups of molecules and recording electrical signals as the molecular junctions are stretched and broken. These techniques have been used to study many

fundamental aspects of single-molecule junctions, and they have given new impetus to the field of molecular electronics. However, despite sharing the same basic concepts, there is an ongoing debate on the comparability between these techniques in terms of single-molecule conductance determination. Apparent discrepancies between conductance values have been reported between different laboratories using these different techniques. For example, in early studies, the conductance of octanedithiol was measured to be 20 nS using the STM BJ technique by Xu et al. [11], whereas Haiss et al. obtained a value of 1 nS by the analogous STM technique [119]. This was later rationalized as arising from different ways in which these alkanedithiols can bind to the gold contacts through the thiol end groups, with the differing techniques favouring different anchoring configurations [28,52,120,121]. Indeed, measurements on surfaces of different roughness values showed different prominent conductance values [120]. Measurements with the STM BJ technique tend to form "rougher" contacts because of the gold contact breaking, while the $I(s)$ technique can be applied to flat surface areas if desired. In this respect, these techniques can be seen as complementary, and the application of both to the same molecular system could be expected to broaden the view of the molecular junction properties and the spread of favoured junction conductance values. CP-AFM, on the other hand, conveys the advantage of being able to record the force and current signals simultaneously offering the possibility to correlate electrical and mechanical properties of junctions [116,122]. However, a potential disadvantage can arise with the use of AFM tips with higher radii of curvature, where there could be ambiguity about forming truly single-molecule junctions when CP-AFM is used to form break junctions. In any case, measurements of molecular conductance with several different techniques should be seen as advantageous [122].

Metallic materials have been widely used as the electrodes to construct molecular junctions, where desired characteristics are outstanding stability, conductivity, and fabricability [19]. There is indeed a plethora of investigations of molecular junctions using metals (Au, Ag, Pt, Al, and Cu) as the electrodes [48,123]. However, there is an increasing interest in deploying carbon based electrodes to fabricate metal-free molecular junctions [124]. Among carbon-based materials, graphene is a promising

material with remarkable electrical and structural properties. On account of its high structural stability, charge carrier mobility, high thermal conductivity, and optical transmittance, graphene is considered to have many potential applications in electronics devices [78]. To date, systematic comparative investigations of graphene/molecule junctions formed by a variety of single-molecule junction techniques have not been performed.

In light of the discussion above, we systematically investigate the molecular conductance with a bottom graphene contact by comparing results from the STM BJ, STM *I*(*s*), and CP-AFM BJ techniques. As a first step, the conductance of 1,8-octanedithiol in gold−gold junctions was measured by the STM BJ, *I*(*s*), and CP-AFM BJ techniques to provide control experiments and to evaluate the stability of our experimental setup. These data for Au−alkanedithiol−Au junctions correspond well with the literature. Following this, the setups were applied to gold−graphene asymmetric junctions. The length dependence of conductance for Au/alkanedithiols/ graphene junctions has been determined and decay constants (attenuation factors) compared. When compared to standard gold−gold junctions, a lower attenuation factor is observed for the gold−graphene counterparts when applying both the STM based *I*(*s*) and CP-AFM methods. On the other hand, stable molecular junctions using graphene bottom contacts could not be formed with the STM BJ method and reasons for this are suggested.

5.3 Results and discussion

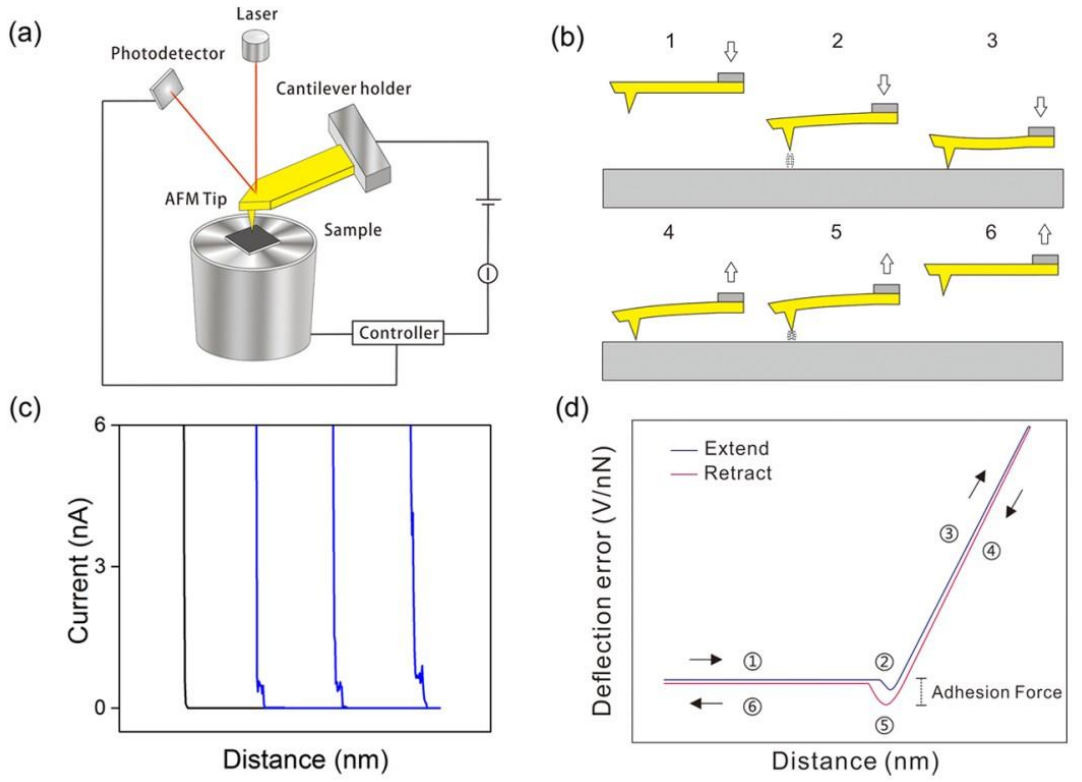

Figure 40. (a) Schematic diagram of the CP-AFM BJ technique. (b) Tip movement of the AFM tip and molecular junctions formed during the process. The AFM probe was first brought close to the substrate (1−3) and then withdrawn to its initial distance (4−6) after the contact is established. (c) Typical current−distance curves of the bare substrate (black, without molecular junctions formed) and molecular junctions formed (blue). (d) Typical force−distance curves representing the force loaded on the surface. The arrow and numbers (1−6) correspond to the tip movements in (b). The curves were sketched based on the data from gold−1,8-octanedithiol−gold junctions for better illustration.

We first determined the conductance of gold−1,8-octanedithiol−gold molecular junctions using the three techniques described in the introduction. The detailed setup for STM based techniques can be either found in our previous studies or other literature [105,125,126]. A description of the CP-AFM BJ method with the concurrent collection of currents and forces is given in the following text. Instead of using a fixed tip-sample distance while collecting the *I*−*V* data, in the CP-AFM BJ technique, the current and tip-sample distance is recorded at a fixed bias voltage as the AFM tip-cantilever assembly is rapidly retracted from the surface. Figure 40a shows a schematic diagram of the CP-AFM BJ method. The AFM force feedback circuit is used to control the force applied to the sample, whereas an extra electrical circuit is used to collect the current

signal. Similar to the STM BJ method, the conductive AFM probe was initially set at a given distance and then brought close to the substrate surface until contact is established (positions 1−3 in Figure 40b). During the approach process, a jump to the contact force is observed (2) followed by a corresponding deflection of the cantilever as it is moved to the set-point force (3). The AFM probe was then withdrawn to its initial distance by adjusting the piezo scanner of the AFM (positions 4−6 in Figure 40b), and a jump from the contact is observed at position 5 during the process. The molecular targets can span the narrow gap through the stochastic formation of molecular junctions, both during the approach and retraction processes (position 1−2 and 5−6). In such a circumstance, a plateau feature is observed during retraction, signifying the formation of a molecular junction (blue curves in Figure 40c). For situations where no molecular junctions are formed, a fast decay of the current is observed as a function of the distance (black curve in Figure 40c). It is noted that the "distance" here is not the real length of the molecular junction, but the extension or retraction of the piezo scanner. Figure 40d shows a sketched illustrative force−distance curve which shows the loading of the force on the surface, and the subsequent cleavage of junction as the piezo scanner is extended. This curve contains information about the force applied to the AFM probe and the adhesion force. In the case of molecular monolayers, it would be expected that a higher force loaded on the surface would produce a greater deformation of the monolayer and possibly a greater contacting footprint, both of which may be likely to give a higher junction conductivity. Excessive force may result in structural damage to the probe apex, SAMs, and the bottom electrode; therefore, careful control and monitoring of the force curve is desirable. It is important to note, however, that the CP-AFM BJ experiments are different to the conventional CP-AFM experiments on molecular monolayers because in the former case, the force is unloaded as conductance is measured while the tip/cantilever assembly is being retracted. Nevertheless, the adhesion force might be important for such determinations [127]. The molecular junction is broken as the AFM probe snaps back from the surface. Forces are negative ("attractive"), and in general, the magnitude of such forces is about 10 nN according to the literature [26,127]. Another possible source of adhesion is the capacitive force

which might be expected to scale with the magnitude of the applied voltage. In most of the situations, this is relatively minor, for example, around 1 nN at a voltage of 1 V [116].

In our experiment, the movement (deflection) of the probe is achieved by applying the bias voltage to the piezo scanner, and an additional conversion of the voltage to the force signal is required to plot the force versus distance curve. In the simplest situation in the contact regime, the spring constant formula, $F = kx$, can be applied where F is the force applied to the surface, k is the spring constant of the gold probe, and x is the deflection of the gold probe (see Chapter 2 for detailed explanations). We applied the minimum force (lowest deflection of the probe) to the surface where the current signal is stable. Such contacting force can be varied (from 20 to 300 nN) during the process which is highly dependent on the topographical situation of the sample and the SAMs of the molecules.

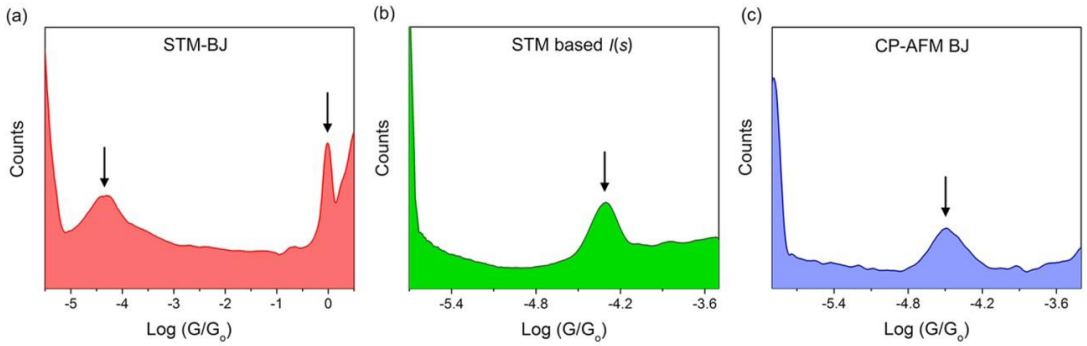

Figure 41. Conductance histograms for gold−1,8-octanedithiol−gold junctions constructed by (a) STM BJ, (b) STM-based $I(s)$, and (c) CP-AFM BJ techniques.

Generally, over 10 000 current−distance raw curves were collected with the preset bias voltage and set-point current followed by data analysis, either manually or automatically. The plateau featuring curves were then used to plot the 1D conductance histogram representing the most probable conductance value of the junction. Figure 41 shows the 1D conductance histograms of gold−1,8-octanedithiol−gold molecular junctions recorded by STM BJ, STM-based $I(s)$, and CP-AFM BJ techniques. Two dominant peaks located at 3.5 and 77 400 nS are observed in Figure 41a, demarking the

most probable conductance value of the molecular junction and gold−gold quantum contact conductance G_o ($G_o = 2e^2/h$), respectively. Owing to the limitation of the detector dynamic range, only the conductance peaks located at 3.7 and 2.3 nS are observed in Figure 41b and 41c, respectively. The conductance values of the three techniques are in good agreement with previous studies [36,44], indicating the reliability and stability of our setup. The conductance value obtained from CP-AFM BJ is slightly lower than from STM-based techniques. This may be because of differences in how the contacts are formed and how gold atoms rearrange during the contacting process, resulting in different distributions of favored contacting configurations [30]. During the early stages of single-molecule conductance measurement, there were some apparent discrepancies in the literature, with reports of different conductance values for gold−octanedithiol−gold molecular junctions created by different methods [28,52,120,121]. In an early report, Chen et al. distinguished two sets of peaks, which were designated as high conductance and low conductance (LC) values [44]. As discussed in a review, and references therein, the different conductance groups could be related to different molecule contact morphologies and the roughness of electrode contacts [28,128]. Different conductance groups could be attributed to different possible molecule−electrode configurations; for example, with the sulfur atoms coordinated to either single gold atoms, bonding to multiple surface atoms or in higher coordination defects sites such as at gold steps [28].

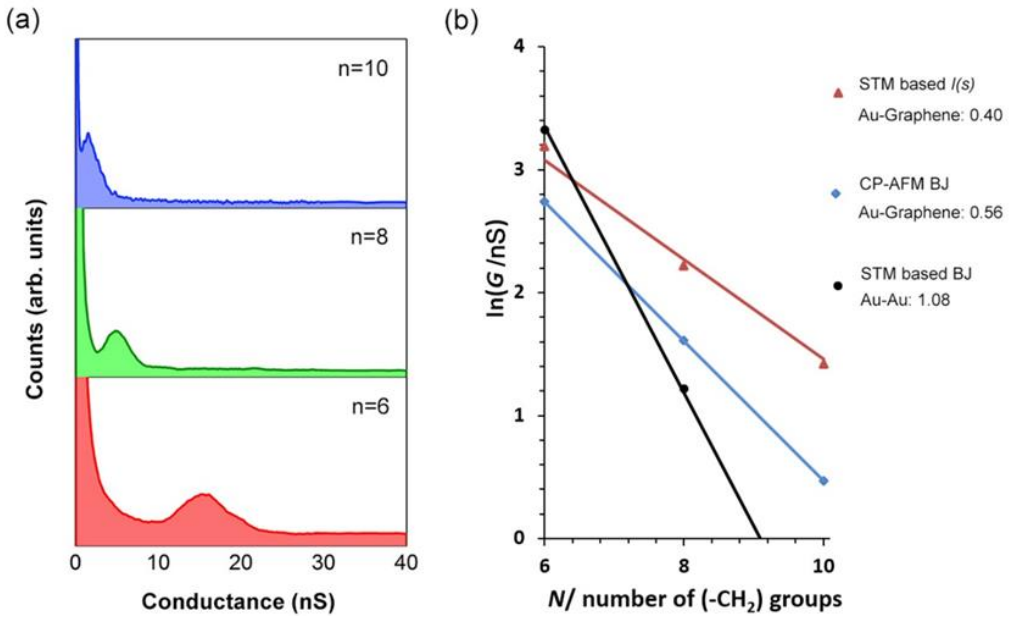

Figure 42. (a) Conductance histograms for gold−n-alkanedithiol−graphene junctions (n = 6, 8, and 10). (b) Natural logarithmic plot of the conductance with the number of methylene groups measured by different techniques: red line measured by the STM-based *I*(*s*) technique, blue line measured by the CP-AFM BJ method, and black line measured by the STM BJ technique.

The bottom gold electrode is now replaced by the graphene substrate, while using the same setup as described in the foregoing text for gold−1,8-octanedithiol−gold single molecule junctions. The aim here is to investigate the impact for substituting gold for a graphene contact and whether the junction formation method plays a role. Figure 42a shows 1D histograms of gold−n-alkanedithiol−graphene junctions (n = 6, 8, and 10) with the same conductance and count scale. In each conductance histogram, only one pronounced peak is observed, indicating the most probable conductance of the junction. It is clear that the conductance values decrease as a function of the molecular length. In principle, a number of approaches might be used to describe the length dependence of the junction conductance [129], for example, coherent resonant tunneling, coherent nonresonant tunneling, or diffusive transport. Here, the transport behavior is typically in the nonresonant tunneling regime, where the conductance scales exponentially with the separation of the electrodes and consequently with the molecular length [26]. Despite its known limitations, it is common to use a simplified Simmons model to express the conductance as $G = A \exp(-\beta_N N)$, where β_N is the decay constant, $\beta_n = 2\sqrt{2m\phi/\hbar^2}$ [23,97,130], and the prefactor A is related to the effective contact

resistance which is commonly linked to the nature of the molecule−electrode interaction. To experimentally obtain the decay constant of the junction, the natural logarithm of the conductance is plotted against the molecular length. Then, the tunneling decay constant, or the attenuation factor β_N, is given by the slope of the linear fit, and the contact resistance is determined by the intercept at the zero junction length [69]. Figure 42b shows the natural logarithmic plot of conductance with the number of methylene groups. The blue and red lines represent the decay constant (β_N = 0.56 and 0.40) of gold−alkanedithiol−graphene junctions measured by the CP-AFM BJ technique and the STM-based $I(s)$ technique, respectively. The black line represents the decay constant (β_N = 1.1) of gold−alkanedithiol−gold junctions measured by the STM BJ method from the literature [36,44].

We are not able to measure the conductance of 1,8-octanedithiol with graphene bottom contacts by the STM BJ method using the same experimental setup as shown in Figure 41a. The physical mechanism of forming defined, stable, and reproducible metallic contacts by the STM BJ method has been well studied by Sabater et al. both experimentally and theoretically [131]. They suggested that a clear conductance trace can be obtained when the tip indentation depth is greater than the value which corresponds to a conductance of $5G_o$. This gives a minimum cross section corresponding to 15 atoms for the case of gold. During the contact cycles, a number of gold atoms are exchanged between the two sides of the gold electrode with respect to its original configuration, and this tends to reach a constant number after 7−8 cycles. Stable tips are formed after 10 cycles with a pyramidal shape evolving with (111) faces which complies with energetic considerations. Here, in the case of graphene as the bottom electrode, such atom exchange phenomena between the upper and lower contact are clearly not possible. Because in the STM BJ method the STM tip is pushed into the substrate, it could be easily compressed or damaged upon hard physical contact with the graphene surface. Therefore, the failure of the STM BJ method to capture a stable current signal with graphene bottom contacts might be explained by the excessive force loaded on the sample. It seems that the noncontact STM $I(s)$ technique or CP-AFM method with in situ force monitoring is more suitable for few layers of graphene substrates or other two-dimensional (2D) thin-film materials.

Table 4. Conductance Values, Decay Constant, and Contact Resistance for Gold−n-Alkanedithiol−Graphene and Gold−n-Alkanedithiol−Gold Junctions (n = 6, 8, 10), with Literature Values Included in the Latter Case [a]

Molecular junction	Techniques	Conductance (nS)			Decay constant (β_N)	Contact resistance (kΩ)
		n = 6	n = 8	n = 10		
gold-n-alkanedithiol-graphene	CP-AFM break junction (contact mode)	15.6	7.2	1.7	0.56	~ 2100
gold-n-alkanedithiol-graphene	STM based *I*(*s*) (non-contact mode)	24.0	9.0	4.0	0.40[91]	~ 3900
gold-n-alkanedithiol-gold	STM break junction (contact mode)	28.2	3.9	0.2	1.08(LC)[36,44]	~ 27

[a] The conductance values involved correspond to the center value of the Gaussian fit from the dominant peak in the conductance histogram.

Table 4 summarizes the experimental values and the decay constants of nonsymmetric gold−n-alkanedithiol−graphene measured by the CP-AFM BJ and STM-based *I*(*s*) techniques. The conductance values (LC values in ref 44 and values in ref 36) of gold−gold symmetric junctions are also listed for comparison. The conductance values obtained with the CP-AFM BJ method for graphene bottom contacts are slightly lower than the ones reported in our previous work [105] using the STM-based *I*(*s*) technique, which may be related to different ways in which the junctions are created. Both CP-AFM BJ and *I*(*s*) techniques show similarly low decay constant (β_N) values for gold−alkanedithiol−graphene junctions when compared to the much higher β_N values for symmetric gold−gold molecular junctions. Our previous experimental and theoretical studies have suggested that the low decay constant is ascribed to the breaking of the junction symmetry [105,125]. Here, in the present case of nonsymmetric gold−n-alkanedithiol−graphene junctions constructed by the CP-AFM BJ method, we observe the same behavior. It is well known that thiolate can form a strong covalent bond with gold, whereas the interaction of the thiol with graphene is mainly related to the van der Waals (vdW) interaction [98]. The contact resistance is given by extrapolating the chain length to zero in Figure 42b, and the resistance values are found to be ~3900 and ~2700 kΩ for graphene nonsymmetric junctions formed by STM *I*(*s*)

and AFM based techniques, respectively. These values can be compared to much lower resistance (~27 kΩ) for Au−alkanedithiol−Au symmetrical junctions. This can be explained by coupling at the graphene−molecule interface which is quite weak and primarily dominated by vdW coupling. The influence of electrode materials on contact resistance in the low-voltage regime has been investigated by the Frisbie group [132]. It was reported in that case that for metallic electrodes, the contact resistance decreases substantially with the increasing electrode work function. The work function of the single-layer graphene is around 4.5 eV [133], which is lower than that of gold at 5.3 eV [134]; therefore, this is also consistent with a higher contact resistance for Au(tip)/Graphene(substrate) compared to the Au(tip)/Au(substrate) system. Because of the high asymmetry of the junctions, the thiol−graphene dipole does not compensate the thiolate−gold dipole, and a significant highest occupied molecular orbital (HOMO) level shift toward the Fermi level is then observed [105]. This explains why we obtained low decay constant values in both techniques with graphene bottom contacts and reveals that the change of decay values is mainly dependent on the electrode itself and not on the measurement method.

5.4 Conclusion

In summary, we have used the CP-AFM BJ method to study the effects of molecule−electrode contacts in single-molecular junctions. The typical gold−octanedithiol−gold molecular junctions fabricated by STM BJ, STM-based $I(s)$, and CP-AFM BJ techniques were first examined to verify the stability of the experimental setup, and the determined conductance values agree well with the literature. This setup was then used to investigate the differences which transpire when the bottom electrode contact is changed from a gold to graphene substrate to form gold−n-alkanedithiol−graphene molecular junctions. Both the STM-based $I(s)$ and CP-AFM BJ techniques showed a similar behavior; namely, the conductance decays exponentially as a function of the molecular length with β_N of 0.40 and 0.56 for gold−graphene asymmetric junctions. This is significantly lower than the corresponding symmetric Au−alkanedithiol−Au junctions (β_N = 1.1) previously reported in the literature. This behavior leads us to suggest that the change of decay values is mainly related to the electrodes themselves and not greatly influenced by the measurement method. Both CP-AFM BJ and $I(s)$ show contact resistance values on the molecule−graphene side that are much higher than that on the molecule−gold side. The resulting unbalanced interactions at these two different sides of the molecular junction result in noncompensation between thiol−graphene and thiolate−gold dipoles. This consequently leads to a significant HOMO level shift toward the Fermi level, as we have theoretically described in chapter 3 and 4. A slightly lower conductance value measured by the CP-AFM BJ with respect to the STM based $I(s)$ technique is also observed, which may be because of differences in the junction formation method and in the resulting distribution of molecule−electrode contacts. On the other hand, the STM BJ technique does not lead to the formation of stable molecular junctions with graphene bottom contacts. The STM BJ technique requires that a hard physical contact be made between the tip and the substrate, which differs from the STM-based $I(s)$ technique, which is a noncontact method. There could be many reasons behind this inability of the STM BJ technique to form stable molecular junctions with a graphene bottom contact. The STM BJ technique relies on the formation of gold atomic point contacts which,

after cleavage, form an open Au−Au electrode gap to which molecules can be bound. The pressing of the gold tip onto the graphene substrate will clearly deform the soft gold apex but may also produce (transient) substrate deformation. A possible reason for the STM BJ technique being ineffective here could be that there is a high transient instability in the gold tip contact after it has been pushed onto the graphene surface and then withdrawn. This highlights that the method for single-molecule junction formation to be selected depends on the specific system, notably the respective contact materials.

6 Chapter 6: Unsupervised Data Analysis Approach in Single Molecule Junctions Based on the MATLAB Algorithm

6.1 Preface

We have investigated the charge transport properties in graphene based junctions by STM BJ, STM based *I*(*s*) and CP-AFM BJ techniques. For all of these measurements, even the most reliable contact anchoring groups lead to a generally large variability in any given conductance determination, it is thus necessary to repeatedly record many traces and then statistically represent this data by plotting conductance histograms. In chapter 6, we demonstrate a fast and straightforward analysis approach of conductance traces based on an automatic MATLAB algorithm. The results presented in this chapter were published and reproduced with permission from *Nanotechnology*, **2018**, *29*, 325701 (DOI: 10.1088/1361-6528/aac45a), with the title 'Fast and straightforward analysis approach of charge transport data in single molecule junctions' Copyright 2018, IOPscience. This study was designed by Richard J. Nichols, Li Yang, Cezhou Zhao and myself. I carried out the algorithm design, program coding, and the experimental works plus writing the first draft of the manuscript. Chenguang liu also conducted the algorithm design and program coding with the integration of different functions of the code. The manuscript was then corrected by Yannick J. Dappe, Richard J. Nichols, and Li Yang. The rest of authors conducted some other supporting works, for example, the data analysis, discussion and double check the experimental results.

In this study, we introduce an efficient data sorting algorithm, including filters for noisy signals, conductance mapping for analyzing the most dominant conductance group and sub-population groups. The capacity of our data analysis process has also been corroborated on real experimental data sets of Au-1,6-hexanedithiol-Au and Au-1,8-octanedithiol-Au molecular junctions. The fully automated and unsupervised program requires less than one minute on a standard PC to sort the data and generate histograms. The resulting one-dimensional and two-dimensional log histograms give conductance values in good agreement with previous studies. Our algorithm is a

straightforward, fast and user-friendly tool for single molecule charge transport data analysis. We also analyze the data in a form of a conductance map which can offer evidence for diversity in molecular conductance. The code for automatic data analysis is openly available, well-documented and ready to use, thereby offering a useful new tool for single molecule electronics.

6.2 Introduction

It is now possible to reliably measure the conductance of single molecules trapped between metallic electrodes. Important experimental factors here include achieving reliable and robust electronic and chemical coupling between the molecular bridge targets and the contacting electrodes [7,11,72]. Techniques capable of trapping single molecules between electrode contacts include the use of scanning tunnelling microscopy (STM) [13,44,104], conducting atomic force microscopy [12], mechanically formed break junctions (BJs) [10] or nano-lithographically created gaps [135]. However, for all of these techniques, even the most reliable contact anchoring groups lead to a generally large variability in any given conductance determination [14]. This can be due to a number of factors including variable surface binding geometry between the molecule and contact, noise, environmental and contact fluctuations, multiple and interacting molecules in the gap and the stochastic nature of the junction formation and breaking processes [136]. It is then necessary to repeatedly record many traces and then statistically represent this data recorded for the making and breaking of many molecular junctions. In the simplest case, a single peak in a 1D conductance histogram resulting from plateau featured traces is usually taken to represent molecule junction formation and the most probable conductance value [137-138]. Such a statistical analysis has been underpinning for achieving reliable electrical data for single molecule junctions.

There are then two broad approaches which can be applied to statistically analyze the data, each of which has its advantages and disadvantages. The first approach is to simply use all traces in the conductance histogram analysis. This has the advantage that there is no data preselection, however the analysis may include a lot of traces where either no or poorly contacted molecular junctions are formed. It may also be not possible to recognize molecular junction data if the probability of junction formation is low. The second approach is to try to select events where clear molecular junctions form from those where they do not. The advantage here is that data that is not relevant to molecular junction forming events is removed from the analysis, while molecular data is retained. The disadvantage here is that a preselection of data could introduce

conscious or unconscious bias and affect the scientific interpretation of the determined conductance values [36]. It is of benefit to the single molecular electronics community to have a range of different analysis approaches available, including both the analysis of unselected data, as well as algorithmic approaches which attempt to recognize molecular junction forming events. The aim of the present study is to provide a new and well-documented approach to the latter.

Early work used hand-selected data through the recognition of plateau containing traces as an indicator of good molecular junction formation, although it is recognized here that care has to be taken to avoid conscious or unconscious bias. On the other hand, a few algorithmic approaches to data selection have been presented in the literature. Jang et al. have introduced a last-step analysis method for determining single molecule conductance, in which traces are selected which are believed to arise from molecular junction formation [36]. In this method, only curves featuring a very rapid conductance drop in the last step are selected. Gonzalez et al. presented an alternative method to extract the electrical conductance curves from a set of measured conductance traces [37]. Instead of selecting the plateau-containing curves, they consider all the traces and only remove background curves that feature a normal exponential decay of current synonymous with tunneling through an empty gap. Halbritter et al. introduced a two-dimensional (2D) correlation analysis of conductance traces to study the contact evolution in metal nano-junctions [139]. However automatic selection and analysis tools are also desirable for high throughout data analysis.

More recently an algorithmic method has been used for data sorting by Albrecht group [38-39]. Firstly, for each exported current-distance trace the current signal is divided into many bins with a selected bin width (BW). Each bin will have a value for the number of plateaus-determining bin counts. With a sorting algorithm which recognizes plateau containing traces from the bin counts, the traces containing plateau (molecular) features can be separated from both exponential traces and those primarily related to experimental noise [38]. Inspired by the widespread application of vector based classification method in genetics, robotics and neuroscience [40-41], they also developed an unsupervised vector-based classification of $I(s)$ traces which

demonstrates how differently shaped $I(s)$ curves can be separated and grouped into clusters. Different event shapes are separated by this approach which essentially relies on a pattern analysis using several variables extracted for each current versus distance trace [39].

The methods described above are based on the ideas of how to select plateau featured curves or how to group the $I(s)$ traces into clusters of traces showing similarities. In typical experimental sets, instabilities in the molecular junction formation process, stochastic fluctuations in the microscopic details of the metal contacts or contamination of electrodes may all produce 'noisy' traces which lead to the inclusion of traces in a data set which are not representative of proper molecular junction formation and consequently present difficulties in the subsequent data analysis. It is hence desirable to therefore effectively remove traces which do not show molecular junction formation.

Instead of such a targeted selection of plateau featured curves, we propose here a different approach to data analysis, which does not select plateau featured traces, but removes undesired curves with clearly bad decay features as well as noisy traces, while keeping plateau-containing traces which are generally indicative of molecule junction formation. We demonstrate this method's ability to treat actual experimental data obtained from the well-studied gold-octanedithiol-gold and gold-hexanedithiol-gold molecular junction systems [52-53]. The originality of this work lies in offering a new and straightforward scheme for automatic data analysis with good performance (the data processing time is less than one minute). The present approach can also offer evidence for diversity in molecular conductance.

6.3 Results and discussion

6.3.1 *Data collection*

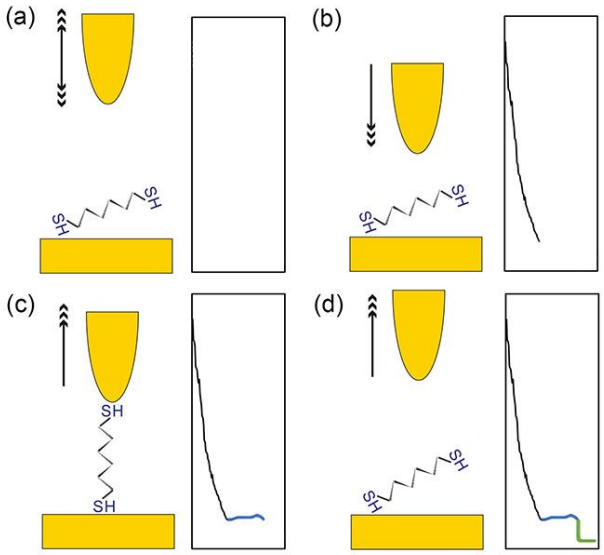

Figure 43. Schematic diagram of the *I*(*s*) technique. (a) The initial stage of the molecular junction. (b) The gold tip is brought close to the gold substrate, the black curve represents the sharp decay of the current. (c) Formation of the Au-octanedithiol-Au molecular junction, the blue curve represents the plateau signal. (d) Breaking of the molecular junctions, with the green curve showing the rapid drop of the current.

The experiments were performed using the *I*(*s*) technique, implemented according to the methodology described by Haiss et al. [119] with necessary modification to our Bruker STM instrumentation. For the *I*(*s*) measurements the gold STM tip was initially set at a given distance and then the tip was approached close to the substrate surface by adjusting the set-point current to high values. Current distance traces were then recorded by rapidly withdrawing the tip back to 4 nm at a rate of 7.66 nm s^{-1}. In the absence of molecular junction formation, an exponential decay of the current is observed. However, upon close approach of the STM tip to the substrate molecules can also bridge the short gap through the stochastic formation of junctions. In such circumstance a plateau in the current-distance traces is typically observed, which is synonymous with the formation of a molecular junction (blue curve in figure 43(c)). With further stretching of such molecular junctions the molecule becomes disconnected from the gold STM tip and a rapid drop of the current signal is then seen as a step at the end of the plateau (green curve in figure 43(d)).

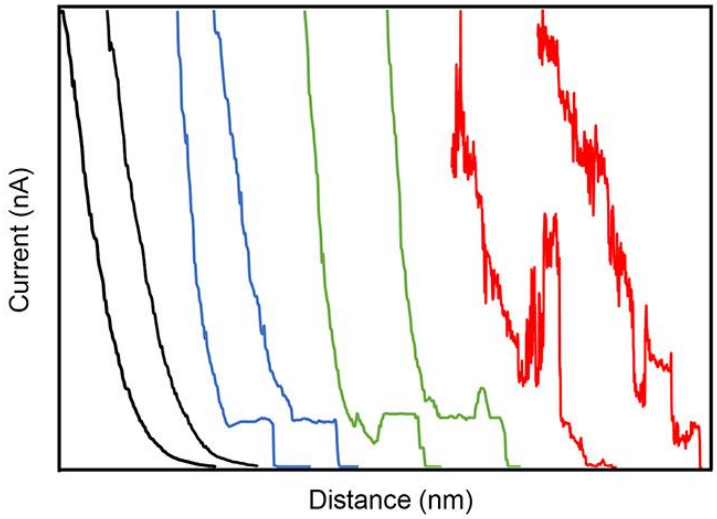

Figure 44. Typical I(s) traces experimentally obtained (black, without molecular junction formation; blue, ideal plateau-featuring curves; green, plateau-featuring curves with noisy peaks; red, very noisy curves).

Over 10 000 current-distance curves were collected during this process with a preset bias voltage of 0.3 V and setpoint current of 10 nA. The $I(s)$ traces can present highly diverse characteristics, such as pure decay (figure 44, black), ideal plateau-featuring curves (figure 44, blue), plateaus with noise spikes (figure 44, green) and highly noisy curves (figure 44, red). The preferred traces, taken as characteristic of stable molecular junction formation, are those featuring with the plateaus (blue), which signify defined formation of molecular junctions followed by their breaking. The aim here is then to sort the data to eliminate curves with abnormal shape or signs of excessive instability or noise.

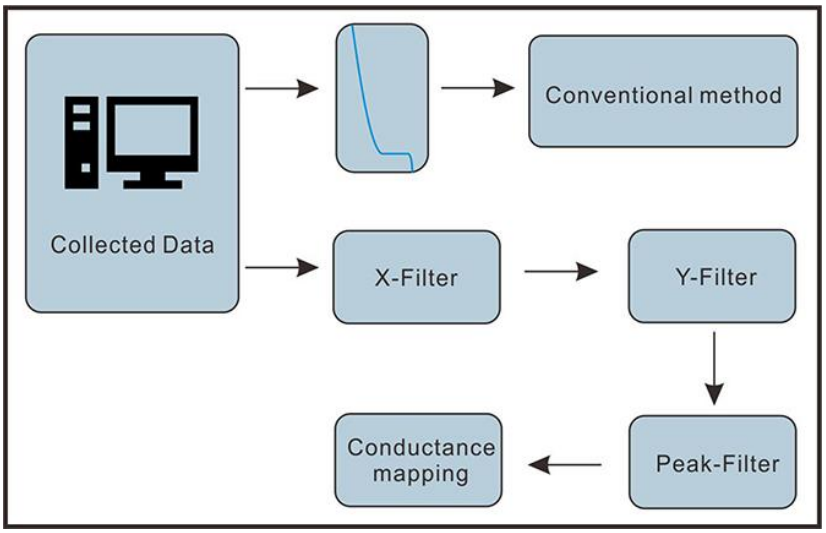

Figure 45. Flowchart of two main data analysis pathways. One is the conventional method of plotting the $I(s)$ signal in a visualized way using the conventional 1D or 2D histograms. The other one is our automatic data sorting algorithm, which includes an X-Filter, Y-Filter, Peak-Filter and conductance mapping functions, as explained in the text.

Generally, two main analysis pathways can be applied to these exported data (figure 45). In the conventional method, the collected $I(s)$ data is plotted in a visualized way as 1D or 2D conductance (junction separation distance) histograms, with plateau featuring curves being selected for the data visualization. However, this approach relies on the signal shape and therefore can impose an assumptive outcome on the final histograms. To avoid this issue, consistent criteria for plateau selection should be applied for every data set, ideally with data analysis or selection which does not make any overly restrictive a priori assumptions about the data shape. In our data sorting routine, the $I(s)$ data is sent through a series of filters to remove any noisy signals caused by, for instance, contamination of the electrodes, passivation of the STM tip, fluctuations of the molecular junctions and so on. The follow filters are applied in a stepwise manner: X Filter, Y-Filter, Peak-Filter. Finally, the conductance mapping distributes the majority of the plateau featured traces and the sub-populations in one histogram.

6.3.2 *X-Filter*

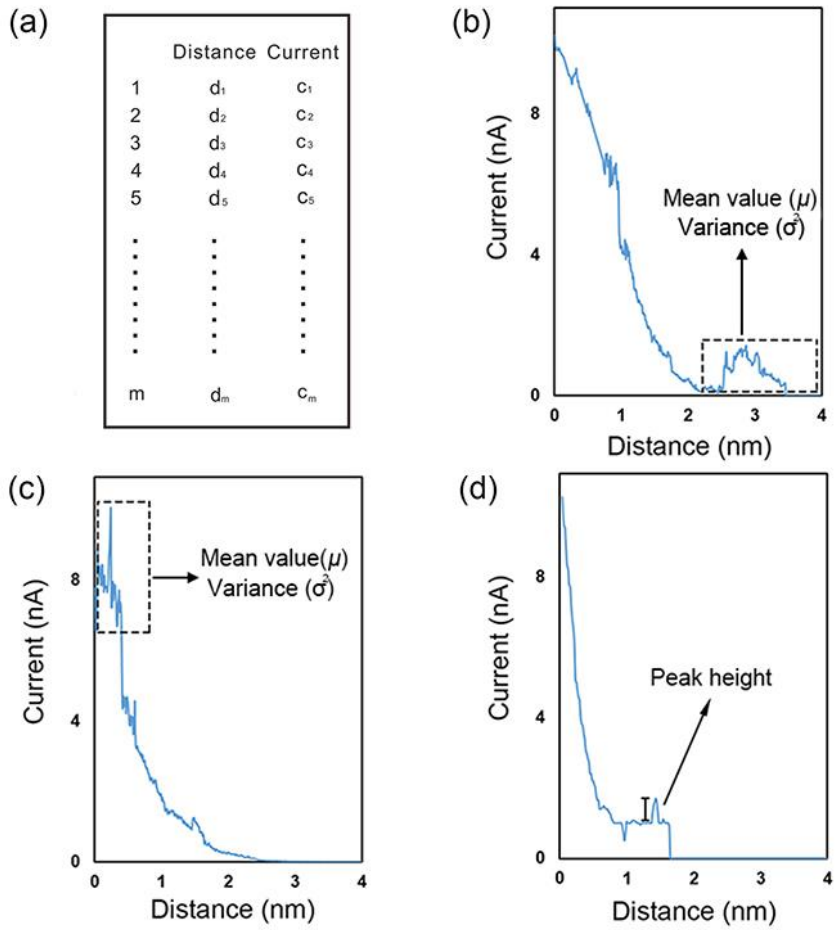

Figure 46. (a) Structure of the I(s) data and schematic diagram of X-Filter (b), Y-Filter (c) and Peak-Filter (d) functions.

Each *I*(*s*) file consists of distance and current signals in m rows as shown in figure 46(a), each row of the data is a single point in the plotted *I*(*s*) curve. For example, the first point p_1 (d_1, c_1), the second point p_2 (d_2, c_2), the third one p_3 (d_3, c_3) and so on, aggregate to a total number of *N* rows resulting in a data matrix. This matrix is the fundamental platform for further processing. Ideally in the absence of molecular junction formation the current will decay exponentially as a function of the increasing distance between the gold tip and substrate, and a well decaying current should approach 0 nA as the distance moves towards the limit of the tip retraction. Also in the presence of molecular junction formation the current should also decay to zero as the molecular bridge is broken and the tip is moved to the limit of its retraction. However, in the real experiment, a certain fraction of retraction traces may show an abnormal

decay of current. In these cases, the current does not proceed effectively towards zero or there are noise features or peaks which appear in the low current range. Our X-Filter algorithm aims at removing these noisy curves caused by the abnormal decay of the current. Here, we consider the distance signal as the *X*-axis, and the current signal as the *Y*-axis. For values above 2 nm ($d_n > 2$) in the *X*-axis, the corresponding values in *Y*-axis have been used for calculating the mean value (μ) and variance (σ^2) (figure 46(b)). The equations for mean value (1) and variance (2) are simple but quite effective.

$$\mu = (c_1 + c_2 + c_3 \ldots + c_N) / N \quad (1)$$

$$\sigma^2 = (c_1 - \mu)^2 + (c_2 - \mu)^2 + \ldots + (c_N - \mu)^2 / N \quad (2)$$

The mean value is used to check whether the current decays to 0 nA, while the variance is used to express the quality of the data being different, divergent or inconsistent. Using a given threshold of mean value and variance, for example, $\mu_c < 0.1$, $\sigma^2_c < 0.1$, only decay curves close to normal would follow this criterion. The chosen mean value and variance as a setting criterion relies on the trial and error scheme (see Chapter 2). The trial and error values can be adjusted many times, with the result being checked in the exported figures. Here, we use 0.1 as the criterion to make sure the current signals decay to close to 0. As a result, abnormally decaying $I(s)$ curves are removed by the X-Filter.

6.3.3 *Y-Filter*

The Y-Filter is also based on the mean value and variance scheme, but here there is a focus on the very beginning of the current decay. When the gold STM tip reaches the preset tunneling region, which is 10 nA in our Au-1,8-octanedithiol-Au system, the current should drop sharply with the retraction of the tip during the very initial stages of junction opening. Some $I(s)$ traces exhibit an oscillating or excessively noisy signal at the beginning of the current decay which may arise from poorly contacted molecules, contaminated tips or multiple interacting molecules in the junction. It is beneficial to eliminate such curves from the final conductance histograms. By locating the data points at the high range of the current, the mean value of the corresponding distance and the variance of these current values have been calculated. For curves which decay well in the initial stages of the retraction corresponding to the current above 6 nA ($y > 6$), the variance of the current should be small (i.e., close to the y axis). There should be a rapid decay of this current and the mean value of the corresponding distance should be close to zero ($\mu_d \sim 0$). However, in the case of figure 46(c), the noisy signal would both bring a higher value of the mean of distance (μ_d) and the current variance (σ^2_c). As a consequence, the mean value of the distance and the variance of the current have been used to define the decay quality in the high current range. To find the optimum mean and variance values for data filtration, the values obtained from well decaying curves can be used as a reference.

6.3.4 *Peak-Filter*

Subsequently, we investigated the noisy peaks present in the plateau region. For $I(s)$ traces with otherwise reasonable current decay forms, the linear plateau can show oscillating signals (small peaks) as shown in figure 46(d). These traces may also be deemed as undesired curves, and if there are sufficient of them they could lead to broadening or shoulder peaks in the conductance histograms. By comparing the mathematical difference of the current values, the location, width and height of the peaks can be obtained. A local peak is a data sample that is larger than its two neighboring samples with the peak height taken as the difference between the peak data and its neighboring samples. If we defined seven current points (1, 2, 1, 3, 1, 5, 1) as a simple illustrative example, then three local peaks (2, 3, 5) with peak height (1, 2, 4) are calculated above the plateau current of 1. Following this regime, the number of the local peaks and the peak height can be then used to classify the data. Although, the $I(s)$ data can present diverse shapes, such as the slanted plateau and nonlinear with high or low amplitude, the Peak-Filter focuses on the removal of telegraphic noise on the plateau, the other plateau traces being then sent to the conductance mapping process.

6.3.5 *Conductance mapping*

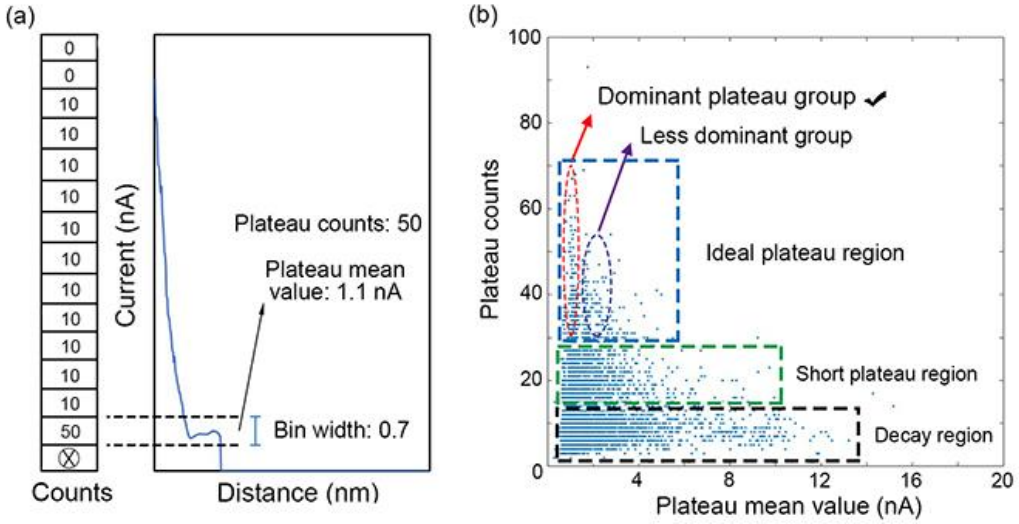

Figure 47. (a) The counts scheme for obtaining the plateau mean value and plateau location. (b) Conductance mapping histogram, including the decay region, short plateau region and ideal plateau region. In the ideal plateau region, a dominant plateau group indicates the most probable conductance value of the molecular junction.

Finally, we use a conductance mapping process to obtain the most dominant conductance value for a given molecular target. For a single $I(s)$ trace constructed from 512 data points, the Y-axis (current axis) was simply divided into many steps (bins). In each bin, the counts of the data points are different and the plateau region will always have a larger bin count than those adjacent bins. We have also noticed that, since the current decays to zero, the first bin will give very large counts, and therefore we excluded this bin to eliminate the effect of the high count value for the first bin. As shown in figure 47(a), the current value was divided into 15 bins (BW = 0.7 nA), the plateau was included in the second bin with a bin counts of 50, and the other bins possess a smaller bin counts of 10. Instead of simply using the bin counts as a criterion to separate the pure decay curve and plateau featured curves which is described by Inkpen et al. [38] here we introduce a new approach for analysing each population of the data set. We select the maximum bin counts to calculate the current mean value of these data points. For example, the maximum counts in figure 47(a) is 50, and consequently we calculate the mean value of these 50 data points to get a plateau mean value of 1.1 nA. Besides the plateau counts, a conductance mapping has been plotted

as shown in figure 47(b). In this map, the $I(s)$ curves have been transformed as blue points according to their plateau mean values (X-axis) and plateau counts (Y-axis). The conductance map was then grouped in three main parts based on the plateau counts. For a region with plateau counts lower than 15 (black rectangular region) in figure 47(b), we deemed it as the decay region, including the pure decay featuring $I(s)$ curves. The point counts for a pure decay curve is low and hence this region lies at the bottom of the plot. Similarly, we treat the plateau counts above 15 but lower than 30 as the short plateau region (green rectangular region) and the plateau counts above 30 as the ideal plateau region (blue rectangular region). In the ideal plateau region, we find that the distribution of blue points has a dominant region (red oval region) and a less dominant region (purple oval region). Even though the plateau position for these featured curves is different, we do observe a dominant region of the plateau mean value to indicate the most probable conductance value for the molecular junction. Notably, for a particular molecular junction, we can also observe multiple plateaus in the $I(s)$ curves and low or high conductance peaks in the 1D histogram [52, 140]. This is ascribed either to the formation of multi-molecule junctions or to different molecular junction configurations [12, 28]. It is thus possible to analyze if the molecular junction is a dominant conformation scheme (one dominant region) or if it has a multiple peak scheme. It is noteworthy that the parameters and settings included in the conductance mapping do not rely on the subjective choices of the operator, but are based on a trial and error scheme. An appropriate setting is achieved after obtaining clear 1D and 2D histograms. Notably, the software can list and try many possible BW and bin count combinations in a very short time.

6.4 Experimental results

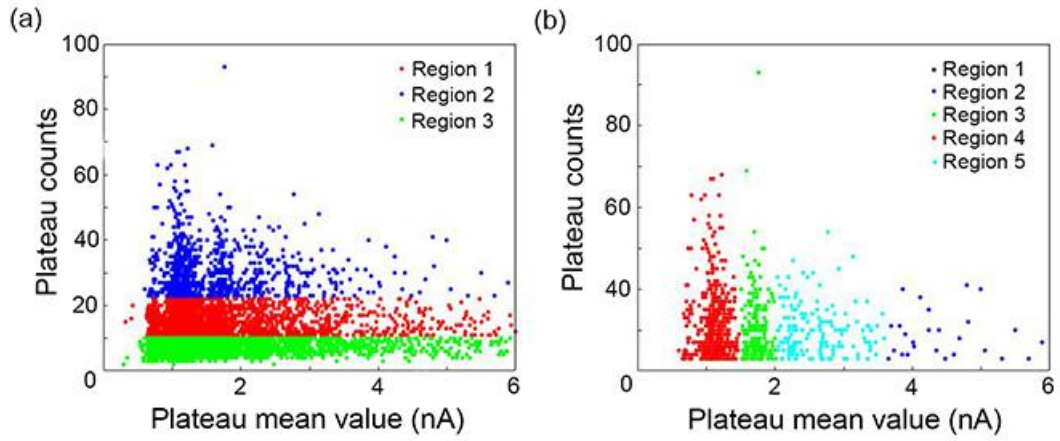

Figure 48. (a) Conductance mapping for Au-1,8-octanedithiol-Au molecular junctions grouped in three main regions based on the plateau counts. (b) Conductance mapping grouped in five refined regions to get insights in the most dominant conductance peak.

We first apply the noise removal and conductance mapping algorithm to the experimental data for Au-1,8-octanedithiol-Au molecular junctions. Over 11 000 $I(s)$ traces were collected at a bias voltage of 0.3 V, a current set-point of 10 nA and a tip displacement of 4 nm from the initial separation at the set-point current. The raw data were directly exported as ASCII text files without any treatment and then analyzed by the algorithm.

In figure 48(a), the conductance map was firstly grouped to three main regions based on the plateau counts. As discussed above, region 1 (green) was deemed to correspond to the decay region without any plateau featured curves included, region 2 (red) reflected the $I(s)$ curves with short plateau or small noisy peaks, and the region 3 (blue) related to the plateau region with linear plateau curves of sufficient extension. To gain insights in these plateau featuring curves, the plateau region was then sorted in the horizontal direction based on the plateau mean value (position of the plateau), and five refined regions were then classified, as shown in figure 48(b). One can clearly observe that region 5 (red) in figure 48(b) presents a dominant number of data points, indicating the highest probability of the plateau position. The $I(s)$ curves in region 5 were then plotted as 1D and 2D histograms.

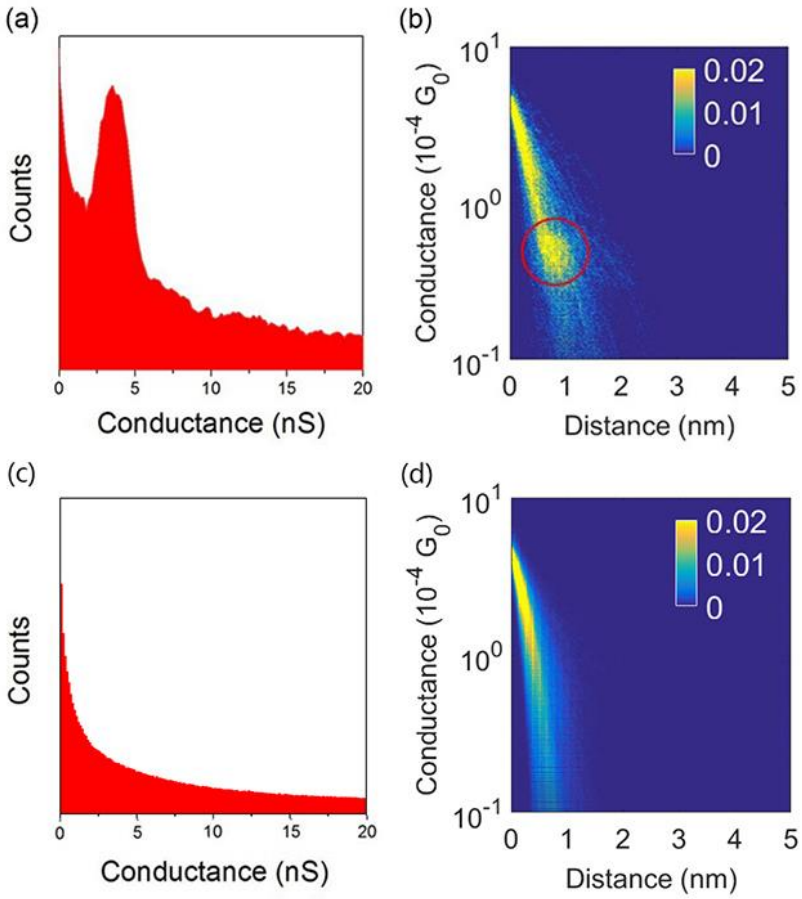

Figure 49. (a) 1D histogram of single-molecule conductance of gold–1,8-octanedithiol–gold junctions, a dominant peak was located at 3.67 nS. (b) The corresponding 2D log histogram with a sensitivity indicator of the conductance counts. 1D (c) and 2D (d) log histogram of all the raw *I*(*s*) data without the treatment of the algorithm.

In the 1D conductance histogram, a dominant peak located at 3.67 nS (4.75×10^{-5} G_o) is observed. The corresponding yellow area around this conductance value in the 2D log histogram indicates the distribution of the plateau featuring traces (figures 49(a), (b)). This conductance value agrees well with previously reported values for Au-1,8-octanedithiol-Au molecular junctions which shows that our automatic data analysis approach is reliable for this test [30,36,44]. For comparison, 1D and 2D histograms are also plotted in figures 49(c) and (d) for the raw data without the use of the algorithm. Since these unfiltered histograms include a lot of traces where either no or poorly contacted molecular junctions form, the conductance peak was then hidden by the large proportion of deleterious background curves. There was a quandary at the early stages of the single molecule conductance technique development that different values of

conductance were measured using different methods [121,141,142]. For the BJ method, both high and low current steps were found, with a primary conductance value of 20 nS being obtained from the BJ technique for gold–1,8-octanedithiol–gold junctions [11]. On the other hand, Haiss measured a primary conductance value of 1 nS using the $I(s)$ method [53]. Nichols et al. suggested this observation could be related to the coordination differences of the sulfur anchoring group to the gold electrodes [28]. Three difference conductance values were attributed to different contact configurations of the thiolate binding to gold surface atoms. Our experimental data found using the $I(s)$ method and conductance mapping process verifies such a conductance diversity and the existence of differing conductance groups. In the conductance mapping, a dominant red region was observed, indicating the most abundant class of plateau featured traces, the other regions being sub-populations caused by other configurations.

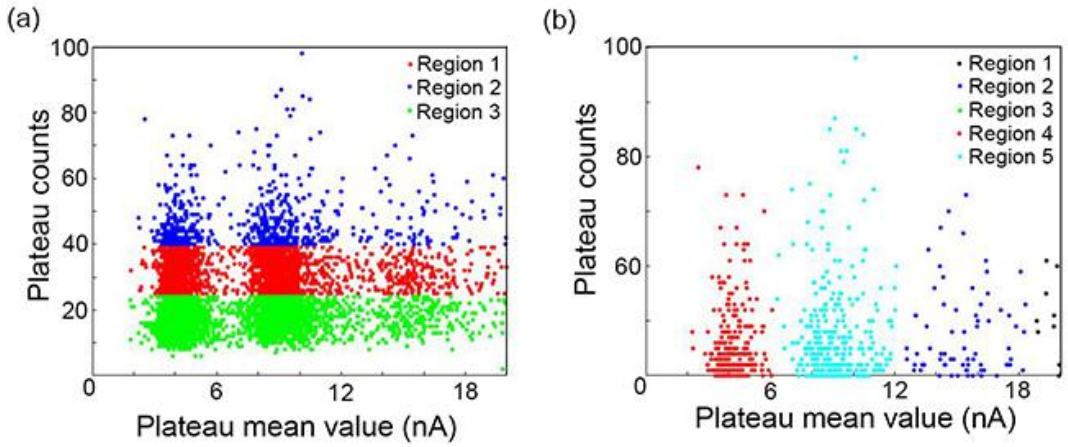

Figure 50. (a) Conductance mapping for Au-1,6-hexanedithiol-Au molecular junctions with color coded grouping into three main regions based on the plateau counts. (b) Conductance mapping of the ideal plateau region, five refined regions were grouped to examine the most dominant conductance peak and sub-groups.

Our algorithm has also been applied to 1,6-hexanedithiol, following a similar procedure to that just described for 1,8-octanedithiol. The resulting conductance map in figure 50(a), was grouped in three main regions, including the decay region (green), short plateau region (red) and the ideal plateau region (blue). The data points at ideal plateau region were then plotted as a refined conductance map with five color coded regions marked. In this map, the light blue region dominates, indicating the most probable conductance value of the Au-1,6-hexanedithiol-Au molecular junction. It is also worth noting here a less dominant red region also appears on this map, representing the possibility of forming a molecular junction with a smaller conductance value. We treat the dominant region (light blue region) as the main conductance value of 1,6-hexanedithiol molecular junctions and the related data was then plotted as 1D and 2D log histograms.

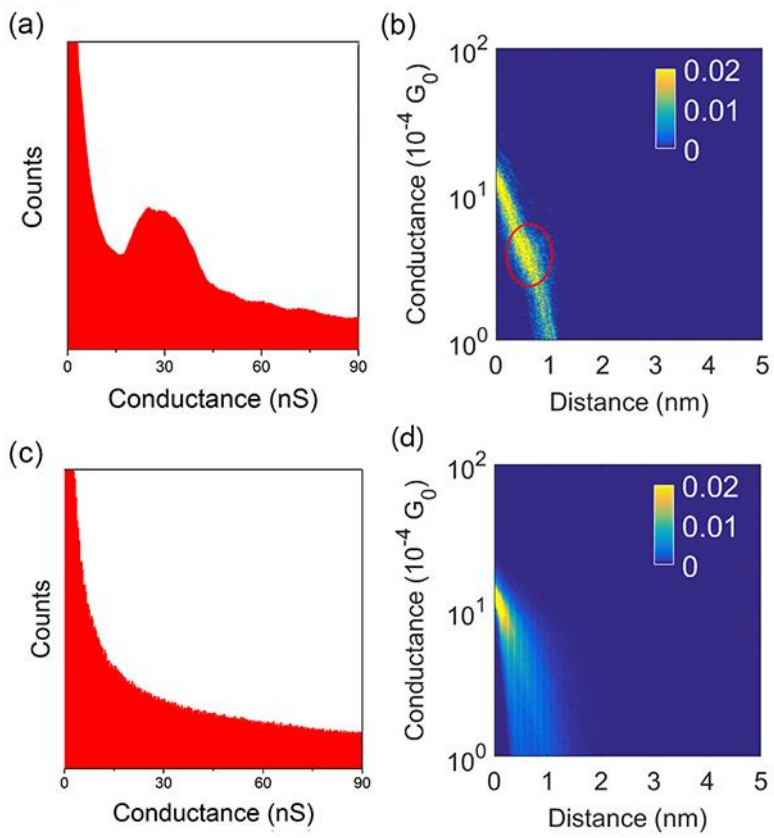

Figure 51. (a) 1D histogram of single-molecule conductance of gold–1,6-hexanedithiol–gold junctions, a dominant peak was located at 29 nS. (b) The corresponding 2D log histogram with a sensitivity indicator of the conductance counts, a higher density yellow region was located at 3.75×10^{-4} G_o. 1D (c) and 2D (d) log histogram of all the raw $I(s)$ data without the treatment of the algorithm.

Figure 51(a) shows the 1D conductance histogram of selected plateau traces; a dominant peak located at 29 nS (3.75×10^{-4} G_o) is observed, the corresponding yellow area in 2D log histogram indicates the distribution of the plateau featuring traces. The 1D and 2D histograms of all curves without any algorithmic analysis have also been plotted (figures 51(c), (d)). In comparison with the previously reported value (28 nS), our data agrees very well with the literature data [36,44]. We also noticed that the less dominant region (red in figure 51(b)) around 4.3 nA showed a respectable number of plateau featured curves, and hence our algorithm can be used to visually assess the number and distribution of each population. The most dominant region (light blue in figure 51(b)) in conductance mapping was considered then to correspond to the most probable configuration of Au-1,6-hexanedithiol-Au molecular junctions with a conductance value of 29 nS.

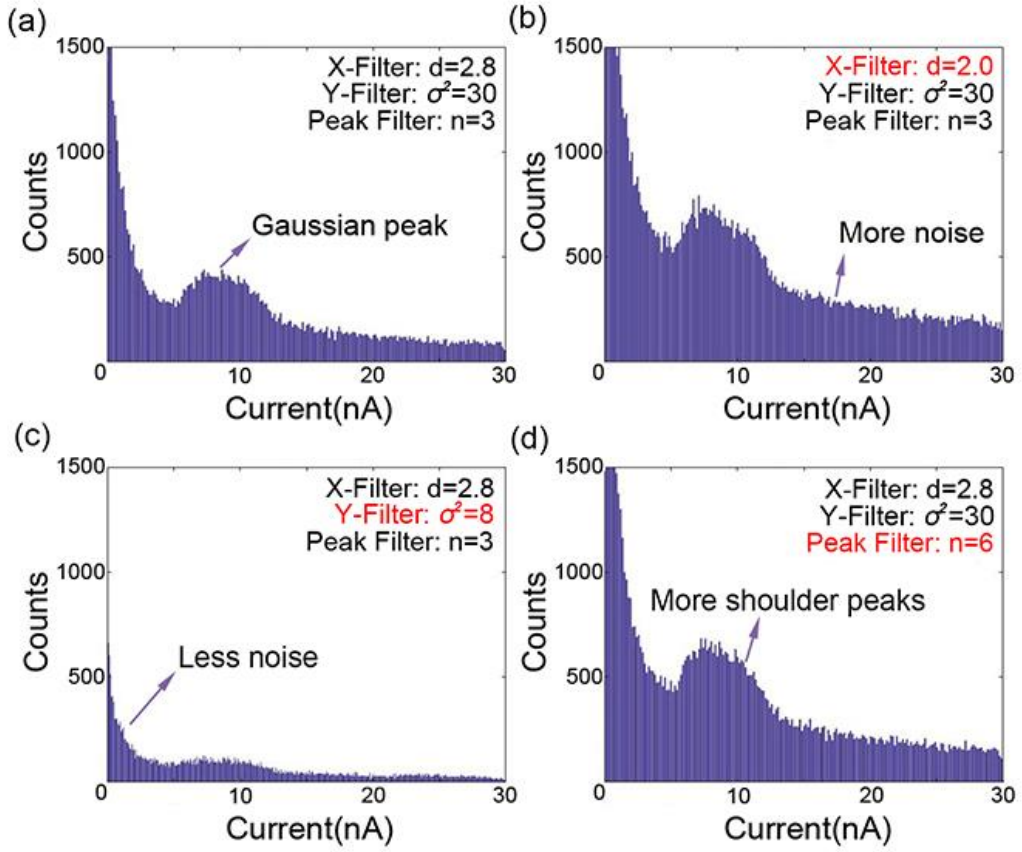

Figure 52. (a) 1D histogram of Au-1,6-hexanedithiol-Au molecular junctions constructed using the given filters. These are an X-Filter at the distance of 2.8 (d = 2.8), the variance of the Y-Filter was set to 30 (σ^2 = 30), the number of peaks for the Peak-Filter was set to 3 (n = 3). (b) 1D histogram plotted using the parameters of X-Filter: d = 2.0, Y-Filter: σ^2 = 30, Peak-Filter: n = 3. (c) 1D histogram after the application of filter using the following parameters: X-Filter: d = 2.8, Y-Filter: σ^2 = 8, Peak-Filter: n = 3. (d) 1D histogram using an X-filter of d = 2.8, Y-Filter of σ^2 = 30, Peak-Filter of n = 6.

Selection of appropriate parameter filters is important for an effective implementation of the algorithm. Here, we take the data from 1,6-hexanedithiol molecular junctions as the example to demonstrate the capabilities of each filter. Please note that the parameters chosen do not simply rely on the subjective choices of the operator, but are based on the trial and error scheme (see detailed explanation in section 2.5.2). Values can be adjusted many times until the clear Gaussian peaks are observed in the exported histograms.

In figure 52, we performed some tests to demonstrate the effect of different algorithm parameters. The 1D histogram in figure 52(a) was deemed to represent the preferred implementation as it gives a well-defined conductance peak, indicating the most probable conductance value of the molecular junction. This histogram was plotted

setting the distance range of 0–2.8 nm for the X-Filter, a variance of 30 for Y-Filter, and a value of 3 for the Peak-Filter. As discussed earlier, the X-Filter algorithm is aimed at removing noisy curves caused by the abnormal decay of the current, by selecting a threshold of the mean value and variance for the selected distance range, for example, d = 0–2.8 nm, $\mu < 0.1$, $\sigma^2 < 0.1$. In figure 52(b), the distance range of the X-Filter was decreased to 0–2 nm, which means more curves could comply with this criterion and consequently contribute noise from the initial decay region. Compared with figure 52(a), only the variance value for the Y-Filter was changed to 8 in figure 52(c), indicating a more stringent criterion. Since the Y-Filter focuses on undesired oscillating or noisy signals at the very beginning of the current decay, the lower variance value cleans up the histogram. Figure 52(d) demonstrates the efficiency of the Peak Filter, by changing the tolerance of peak numbers from 3 to 6, more plateau featuring curves with oscillating signals (small peaks) on the plateau could fit the criterion, the resulting shoulder peaks were then observed. These results demonstrate that some adjustments of the algorithm parameters are necessary for each molecular junction, but even with these adjustments the main peak conductance remains broadly unchanged.

6.5 Conclusion

We present here a simple, fast and user-friendly algorithm for the analysis of single molecule conductance data obtained by the $I(s)$ STM method. This could readily be extended to other methods such as the STM–BJ technique or mechanically controlled BJs. In the supporting information, we provide fully documented MATLAB routines to promote usage of this analysis package by the molecular electronics community. The automatic data analysis process focuses on the removal of traces where proper molecule junction formation does not occur, such as excessively noisy traces as the molecular bridge is formed or traces that do not properly decay to zero current when the molecular junction is cleaved. Through the application of noise removal algorithms, the difficulties caused by instability, fluctuations and noise in single molecule junction formation have been reduced, and data pertaining to effective junction formation can be separated from interfering signals. The remaining traces are then displayed using a conductance mapping process which makes it possible to analyze the statistical diversity in the data set and recognize groups and sub-groups in the data. This captures the statistical complexity of the molecular system in a straightforward way enabling analysis of the effects of molecular structure, contacts, environment and other physical parameters. The algorithms we present here are also amenable to the analysis of very large data sets. The algorithm is a simple and direct method in which the raw $I(s)$ text files are simply copied into the same folder as the program file, the parameters are set and code is simply launched to run the analysis. For experimental groups having a different text structure to ours, only one extra step is needed to convert the text data files. We have applied the algorithm to our experimental data for Au-1,8-octanedithiol-Au and Au-1,6-hexanedithiol-Au molecular junctions. Following the proscribed analysis, a clear conductance peak is seen in the histograms and the conductance values are in good agreement with previous studies. Future development could include coding which eliminates the need to manually set parameters with the algorithm finding suitable parameters itself, for example by exploiting machine learning algorithms.

7 Summary

In this thesis, we have systematically studied the single-molecule conductance of 1,n-alkanedithiols (n = 4, 6, 8, 10, and 12) bridged between the graphene bottom and gold top electrodes by using an STM based technique. The conductance decays exponentially with the number of methylene groups with a decay constant of 0.40, much lower than the value obtained with a second metallic contact. The low decay is related to the junction electronic structure, the nonsymmetric contact, and the weak coupling at the molecule−graphene interface, leading to a stronger charge transfer at the gold electrode−molecule interface. We also investigated the effects of anchoring groups in graphene based junction by constructing the same hybrid gold-alkanediamine-graphene molecular junctions as the dithiol case. A similar attenuation factor (0.37) to the case of alkanedithiol junctions was obtained due to the asymmetric coupling of the diaminealkane molecular chain between gold and graphene. This weak coupling is responsible for the HOMO level shift toward the Fermi energy which consequently reduces the tunnelling barrier at the interface. A slightly higher conductance of the diamine hybrid junction with respect to the dithiol hybrid junction is also found.

The technical effects of molecule-electrode contacts were also investigated by comparing the methods used for capturing and measuring the electrical properties of single molecules in gold−graphene contact gaps. The typical gold−octanedithiol−gold molecular junctions fabricated by STM BJ, STM-based *I*(*s*), and CP-AFM BJ techniques were first examined to verify the stability of the experimental setup and the same setup was then used to investigate the contact difference by changing the bottom gold substrate to graphene. Both the STM-based *I*(*s*) and CP-AFM BJ techniques showed a similar low conductance decay (0.40 and 0.56) when compared to the gold-gold symmetric junctions (1.1). This behaviour leads us to suggest that the change of decay values is mainly related to the electrodes themselves and not greatly influenced by the measurement method. A slightly lower conductance value measured by the CP-AFM BJ with respect to the STM based *I*(*s*) technique is also observed, which may be because of differences in the junction formation method and in the resulting distribution

of molecule−electrode contacts. We also found the STM BJ technique does not lead to the formation of stable molecular junctions with graphene bottom contacts which is probably due to the high transient instability in the gold tip contact after it has been pushed onto the graphene surface and then withdrawn.

We also present a simple, fast and user friendly algorithm for the analysis of single molecule conductance data obtained by the $I(s)$ STM method. The automatic data analysis process firstly focuses on the removal of traces where proper molecule junction formation does not occur. Traces caused by instability, fluctuations and noise in single molecule junction formation have been reduced though noise removal algorithm. The remaining traces are then displayed using a conductance mapping process which makes it possible to analyze the statistical diversity in the data set and recognize groups and sub-groups in the data. This captures the statistical complexity of the molecular system in a straightforward way enabling analysis of the effects of molecular structure, contacts, environment and other physical parameters. The algorithms we present are also amenable to the analysis of very large data sets. We have applied the algorithm to our experimental data for Au-1,8-octanedithiol Au and Au-1,6-hexanedithiol-Au molecular junctions. Following the proscribed analysis, a clear conductance peak is seen in the histograms and the conductance values are in good agreement with previous studies.

The experimental results presented in this thesis are supported by theoretical computation and symmetry considerations for the molecular junctions. This work highlights the attractive features of graphene contacts in molecular electronics, which might inspire their future deployment in new device prototypes. The further work could extend the graphene material to other 2D materials to take the advantage of their chemical and physical properties, for example, the h-BN and MoS_2. The indirect bandgap of the bulk MoS_2 also makes it valuable to build semiconductor based junctions and flexible semiconductors. Future development for the data analysis could include coding which eliminates the need to manually set parameters with the algorithm finding suitable parameters itself, for example by exploiting machine leaning algorithms.

8 References

1. Tsutsui, M.; Taniguchi, M. *Sensors* **2012**, *12*, 7259-7298.
2. Moore, G. E. *Electronics* **1965**, *38*, 114−117.
3. Huang, D. S.; Lee, J. H.; Tsai, Y. S.; Wang, Y. F.; Huang, Y. S.; Lin, C. K.; Lu, R.; He, J. *IEEE International Reliability Physics Symposium (IRPS*), **2018**, 6F.7-1-6F.7-5.
4. Song, H.; Reed, M. A.; Lee, T. *Adv. Mater.* **2011**, *23*, 1583-1608.
5. Metzger, R. M. *J. Mater. Chem* **2008**, *18*, 4364-4396.
6. Mann, B. & Kuhn, H. *J. Appl. Phys.* **1971**, *42*, 4398–4406.
7. Aviram, A.; Ratner, M. A. *Chem. Phys. Lett.* **1974**, *29*, 277−283.
8. Metzger, R. M. *Nanoscale* **2018**, *10*, 10316-10332.
9. Joachim, C.; Gimzewski, J. K.; Aviram, A. *Nature* **2000**, *408*, 541.
10. Reed, M. A. *Science* **1997**, *278*, 252−254.
11. Xu, B.; Tao, N. J. *Science* **2003**, *301*, 1221−1223.
12. Cui, X. D.; Primak, A.; Zarate, X.; Tomfohr, J.; Sankey, O. F.; Moore, A. L.; Moore, T. A.; Gust, D.; Harris, G.; Lindsay, S. M. *Science* **2001**, *294*, 571-574.
13. Haiss, W.; van Zalinge, H.; Higgins, S. J.; Bethell, D.; Höbenreich, H.; Schiffrin, D. J.; Nichols, R. J. *J. Am. Chem. Soc.* **2003**, *125*, 15294−15295.
14. Ratner, M. *Nat. Nanotechnol* **2013**, 8, 378-381.
15. Metzger, R. M. *Chem. Rev.* **2015**, *115*, 5056-5115.
16. Xiao, X., Xu, B. & Tao, J. *Nano Lett.* **2004***, 4*, 267–271.
17. Ruoff, R. S.; Kadish, K. M.; Boulas, P.; Chen, E. C. M. *J. Phys. Chem.* **1995**, *99*, 8843−8850.
18. L. Bogani and W. Wernsdorfer, *Nat. Mater.,* **2008**, *7*, 179.
19. Jia, C.; Guo, X. *Chem. Soc. Rev.* **2013**, *42*, 5642-60.
20. Leary, E.; La Rosa, A.; Gonzalez, M. T.; Rubio-Bollinger, G.; Agrait, N.; Martin, N. *Chem. Soc. Rev.* **2015**, *44*, 920-942.
21. Salomon A. Cahen D. Lindsay S. Tomfohr J. Engelkes V.B. Frisbie C.D. *Adv. Mater.* **2003**, *15*, 1881-1890.
22. Silvia, K. *J. Phys. Condens. Matter* **2011**, *23*, 013001.
23. Cuevas, J. C.; Scheer, E. Molecular Electronics: An Introduction to Theory and Experiment; World Scientific: Singapore, 2010.
24. Guo, X.; Small, J. P.; Klare, J. E.; Wang, Y.; Purewal, M. S.; Tam, I. W.; Hong, B. H.; Caldwell, R.; Huang, L.; O'Brien, S.; Yan, J.; Breslow, R.; Wind, S. J.; Hone, J.; Kim, P.; Nuckolls, C. *Science* **2006**, *311*, 356-359.
25. Nijhuis, C. A.; Reus, W. F.; Whitesides, G. M. *J. Am. Chem. Soc.* **2009**, *131*, 17814-17827.
26. Wold, D. J.; Frisbie, C. D. *J. Am. Chem. Soc.* **2001**, *123*, 5549−5556.
27. C. Kergueris, J. P. Bourgoin, S. Palacin, D. Esteve, C. Urbina, M. Magoga and C. Joachim, *Phys. Rev. B: Condens. Matter Mater. Phys.* **1999**, *59*, 12505–12513.
28. Nichols, R. J.; Haiss, W.; Higgins, S. J.; Leary, E.; Martin, S.; Bethell, D. *Phys. Chem. Chem. Phys.* **2010**, *12*, 2801−2815.
29. Osorio, H. M.; Martín, S.; Lopez, M. C.; Marques-Gonzalez, S.; Higgins, S. J.; Nichols, R. J.; Low, P. J.; Cea, P. *Beilstein J. Nanotechnol.* **2015**, *6*, 1145−1157.

30. Morita, T.; Lindsay, S. J. *J. Am. Chem. Soc.* **2007**, *129*, 7262−7263.
31. Cui, X. D.; Primak, A.; Zarate, X.; Tomfohr, J.; Sankey, O. F.; Moore, A. L.; Moore, T. A.; Gust, D.; Nagahara, L. A.; Lindsay, S. M. *J. Phys. Chem. B* **2002**, *106*, 8609-8614.
32. Mativetsky, J. M.; Palma, M.; Samorì, P. *Top. Curr. Chem.* **2008**, *285*, 157−202.
33. Kelley, T. W.; Granstrom, E.; Frisbie, C. D. *Adv. Mater.* **1999**, *11*, 261−264.
34. Scullion, L. E.; Leary, E.; Higgins, S. J.; Nichols, R. J. *J. Phys.: Condens. Matter* **2012**, *24*, 164211.
35. Nichols, R. J.; Higgins, S. *J. Annu. Rev. Anal. Chem.* **2015**, *8*, 389-417.
36. Jang, S.-Y.; Reddy, P.; Majumdar, A.; Segalman, R. A. *Nano Lett.* **2006**, *6*, 2362−2367.
37. González, M. T.; Wu, S.; Huber, R.; van der Molen, S. J.; Schönenberger, C.; Calame, M. *Nano Lett.* **2006**, *6*, 2238-2242.
38. Inkpen, M. S.; Lemmer, M.; Fitzpatrick, N.; Milan, D. C.; Nichols, R. J.; Long, N. J.; Albrecht, T. *J. Am. Chem. Soc.* **2015**, *137*, 9971-9981.
39. Lemmer, M.; Inkpen, M. S.; Kornysheva, K.; Long, N. J.; Albrecht, T. *Nat. Commun.* **2016**, *7*, 12922.
40. Haxby, J. V.; Connolly, A. C.; Guntupalli, J. S. *Annu. Rev. Neurosci.* **2014**, *37*, 435–456.
41. Naselaris, T.; Kay, K. N.; Nishimoto, S.; Gallant, J. L. Encoding and decoding in fMRI. *Neuroimage* **2011**, ***56***, 400–410.
42. Quek, S. Y.; Kamenetska, M.; Steigerwald, M. L.; Choi, H. J.; Louie, S. G.; Hybertsen, M. S.; Neaton, J. B.; Venkataraman, L. *Nat. Nanotechnol* **2009**, *4*, 230-234.
43. Xiao, X.; Nagahara, L. A.; Rawlett, A. M.; Tao, N. *J. Am. Chem. Soc.* **2005**, *127*, 9235-9240.
44. Chen, F.; Li, X.; Hihath, J.; Huang, Z.; Tao, N. J. *J. Am. Chem. Soc.* **2006**, *128*, 15874−15881.
45. Quinn, J. R.; Foss, F. W.; Venkataraman, L.; Hybertsen, M. S.; Breslow, R. *J. Am. Chem. Soc.* **2007**, *129*, 6714-6715.
46. Park, Y. S.; Whalley, A. C.; Kamenetska, M.; Steigerwald, M. L.; Hybertsen, M. S.; Nuckolls, C.; Venkataraman, L. *J. Am. Chem. Soc.* **2007**, *129*, 15768−15769.
47. Yasuda, S.; Yoshida, S.; Sasaki, J.; Okutsu, Y.; Nakamura, T.; Taninaka, A.; Takeuchi, O.; Shigekawa, H. *J. Am. Chem. Soc.* **2006**, *128*, 7746-7747.
48. Kiguchi, M.; Miura, S.; Takahashi, T.; Hara, K.; Sawamura, M.; Murakoshi, K. *J. Phys. Chem. C* **2008**, *112*, 13349−13352.
49. Peng, Z.-L.; Chen, Z.-B.; Zhou, X.-Y.; Sun, Y.-Y.; Liang, J.-H.; Niu, Z.-J.; Zhou, X.-S.; Mao, B.-W. J. *J. Phys. Chem. C* **2012**, *116*, 21699−21705.
50. Battacharyya, S.; Kibel, A.; Kodis, G.; Liddell, P. A.; Gervaldo, M.; Gust, D.; Lindsay, S. *Nano Lett.* **2011**, *11*, 2709−2714.
51. Kiguchi, M.; Kaneko, S. *Phys. Chem. Chem. Phys.* **2013**, *15*, 2253−2267.
52. Li, X.; He, J.; Hihath, J.; Xu, B.; Lindsay, S. M.; Tao, N. *J. Am. Chem. Soc.* **2006**, *128*, 2135−2141.
53. Haiss, W.; Nichols, R. J.; van Zalinge, H.; Higgins, S. J.; Bethell, D.; Schiffrin, D. J. *Phys. Chem. Chem. Phys.* **2004**, *6*, 4330−4337.

54. Haiss, W.; Martín, S.; Leary, E.; van Zalinge, H.; Higgins, S. J.; Bouffier, L.; Nichols, R. J. *J. Phys. Chem. C* **2009**, *113*, 5823−5833.
55. Li, C.; Pobelov, I.; Wandlowski, T.; Bagrets, A.; Arnold, A.; Evers, F. *J. Am. Chem. Soc.* **2008**, *130*, 318−326.
56. Su, T. A.; Neupane, M.; Steigerwald, M. L.; Venkataraman, L.; Nuckolls, C. *Nat Rev Mater* **2016**, *1*, 16002.
57. Prins, F.; Barreiro, A.; Ruitenberg, J. W.; Seldenthuis, J. S.; Aliaga-Alcalde, N.; Vandersypen, L. M. K.; van der Zant, H. S. J. *Nano Lett.* **2011**, *11*, 4607-4611.
58. Lafferentz, L. et al. Conductance of a single conjugated polymer as a continuous function of its length. Science 323, 1193–1197 (2009).
59. Leary, E.; González, M. T.; van der Pol, C.; Bryce, M. R.; Filippone, S.; Martín, N.; Rubio-Bollinger, G.; Agraït, N. *Nano Lett.* **2011**, *11*, 2236-2241.
60. Martin, C. A.; Ding, D.; Sørensen, J. K.; Bjørnholm, T.; van Ruitenbeek, J. M.; van der Zant, H. S. J. *J. Am. Chem. Soc.* **2008**, *130*, 13198-13199.
61. Aradhya, S. V.; Frei, M.; Hybertsen, M. S.; Venkataraman, L. *Nat. Mater.* **2012**, *11*, 872.
62. Heimel, G.; Duhm, S.; Salzmann, I.; Gerlach, A.; Strozecka, A.; Niederhausen, J.; Bürker, C.; Hosokai, T.; Fernandez-Torrente, I.; Schulze, G.; Winkler, S.; Wilke, A.; Schlesinger, R.; Frisch, J.; Bröker, B.; Vollmer, A.; Detlefs, B.; Pflaum, J.; Kera, S.; Franke, K. J.; Ueno, N.; Pascual, J. I.; Schreiber, F.; Koch, N. *Nat. Chem.* **2013**, *5*, 187–194.
63. Yan, H.; Bergren, A. J.; McCreery, R.; Della Rocca, M. L.; Martin, P.; Lafarge, P.; Lacroix, J. C. *Proc. Natl. Acad. Sci. U. S. A.* **2013**, *110*, 5326−5330.
64. Emberly, E. G.; Kirczenow, G. *Phys. Rev. Lett.* **2003**, *91*, 188301.
65. Zhuang, M.; Ernzerhof, M. *Phys. Rev. B* **2005**, *72*, 073104.
66. Kudernac, T.; Katsonis, N.; Browne, W. R.; Feringa, B. L. *J. Mater. Chem. C* **2009**, *19*, 7168-7177.
67. Elbing, M.; Ochs, R.; Koentopp, M.; Fischer, M.; von Hänisch, C.; Weigend, F.; Evers, F.; Weber, H. B.; Mayor, M. *Proc. Natl. Acad. Sci. U.S.A.* **2005**, *102*, 8815-8820.
68. Song, H.; Kim, Y.; Jang, Y. H.; Jeong, H.; Reed, M. A.; Lee, T. *Nature* **2009**, *462*, 1039-1043.
69. Kim, T.; Liu, Z.-F.; Lee, C.; Neaton, J. B.; Venkataraman, L. *Proc. Natl. Acad. Sci. U. S. A.* **2014**, *111*, 10928−10932.
70. Ullmann, K.; Coto, P. B.; Leitherer, S.; Molina-Ontoria, A.; Martín, N.; Thoss, M.; Weber, H. B. *Nano Lett.* **2015**, *15*, 3512−3518.
71. Dappe, Y. J.; Gonzalez, C.; Cuevas, J. C. *Nanoscale* **2014**, *6*, 6953−6958.
72. Cao, Y.; Dong, S.; Liu, S.; He, L.; Gan, L.; Yu, X.; Steigerwald, M. L.; Wu, X.; Liu, Z.; Guo, X. *Angew. Chem.* **2012**, *124*, 12394−12398.
73. Wen, Y.; Chen, J.; Guo, Y.; Wu, B.; Yu, G.; Liu, Y. *Adv. Mater.* **2012**, *24*, 3482−3485.
74. Jarvinen, P.; Hamalainen, S. K.; Banerjee, K.; Hakkinen, P.; Ijas, M.; Harju, A.; Liljeroth, P. *Nano Lett.* **2013**, *13*, 3199−3204.
75. Bolotin, K. I.; Sikes, K. J.; Jiang, Z.; Klima, M.; Fudenberg, G.; Hone, J.; Kim, P.; Stormer, H. L. *Solid State Commun.* **2008**, *146*, 351−355.
76. Lee, C.; Wei, X.; Kysar, J. W.; Hone, J. *Science* **2008**, *321*, 385-388.

77. Stoller, M. D.; Park, S.; Zhu, Y.; An, J.; Ruoff, R. S. *Nano Lett.* **2008**, *8*, 3498-3502.
78. Song, X.; Hu, J.; Zeng, H. Two-dimensional semiconductors: recent progress and future perspectives. *J. Mater. Chem. C* **2013**, *1*, 2952−2969.
79. Brownson, D. A.; Kampouris, D. K.; Banks, C. E. *Chem. Soc. Rev.* **2012**, *41*, 6944-76.
80. Patel, A. N.; Collignon, M. G.; O'Connell, M. A.; Hung, W. O. Y.; McKelvey, K.; Macpherson, J. V.; Unwin, P. R. *J. Am. Chem. Soc.* **2012**, *134*, 20117-20130.
81. Velický, M.; Bradley, D. F.; Cooper, A. J.; Hill, E. W.; Kinloch, I. A.; Mishchenko, A.; Novoselov, K. S.; Patten, H. V.; Toth, P. S.; Valota, A. T.; Worrall, S. D.; Dryfe, R. A. W. *ACS Nano* **2014**, *8*, 10089-10100.
82. Guo, X. *AIMS Mater Sci* **2014**, *1*, 11-14.
83. Ren, B.; Picardi, G.; Pettinger, B. *Rev. Sci. Instrum.* **2004**, *75*, 837.
84. Sun, L.; Diaz-Fernandez, Y. A.; Gschneidtner, T. A.; Westerlund, F.; Lara-Avila, S.; Moth-Poulsen, K. *Chem. Soc. Rev.* **2014**, *43*, 7378-7411.
85. Venkataraman, L.; Park, Y. S.; Whalley, A. C.; Nuckolls, C.; Hybertsen, M. S.; Steigerwald, M. L. *Nano Lett.* **2007**, *7*, 502−506.
86. Yokota, K.; Taniguchi, M.; Kawai, T. J. Phys. Chem. C 2010, 114, 4044−4050.
87. Chen, F.; Hihath, J.; Huang, Z.; Li, X.; Tao, N. J. *Annu. Rev. Phys. Chem.* **2007**, *58*, 535−564.
88. Kim, B.; Choi, S. H.; Zhu, X. Y.; Frisbie, C. D. *J. Am. Chem. Soc.* **2011**, *133*, 19864−19877.
89. Jia, C.; Ma, B.; Xin, N.; Guo, X. *Acc. Chem. Res.* **2015**, *48*, 2565− 2575.
90. Pshenichnyuk, I. A.; Coto, P. B.; Leitherer, S.; Thoss, M. *J. Phys. Chem. Lett.* **2013**, *4*, 809−814.
91. Liu, L.; Zhang, Q.; Tao, S.; Zhao, C.; Almutib, E.; Al-Galiby, Q.; Bailey, S. W. D.; Grace, I.; Lambert, C. J.; Du, J.; Yang, L. *Nanoscale* **2016**, *8*, 14507−14513.
92. Rocha, A. R.; Garcia-suarez, V. M.; Bailey, S. W.; Lambert, C. J.; Ferrer, J.; Sanvito, S. *Nat. Mater.* **2005**, *4*, 335−339.
93. Quek, S. Y.; Venkataraman, L.; Choi, H. J.; Louie, S. G.; Hybertsen, M. S.; Neaton, J. B. *Nano Lett.* **2007**, *7*, 3477−3482.
94. Nazin, G. V.; Qiu, X. H.; Ho, W. *Science* **2003**, *302*, 77−81.
95. Basch, H.; Cohen, R.; Ratner, M. A. *Nano Lett.* **2005**, *5*, 1668−1675.
96. Gonzalez, M. T.; Brunner, J.; Huber, R.; Wu, S.; Scho´nenberger, C.; Calame, M. *New J. Phys.* **2008**, *10*, 065018.
97. Wang, Y.-H.; Zhou, X.-Y.; Sun, Y.-Y.; Han, D.; Zheng, J.-F.; Niu, Z.-J.; Zhou, X.-S. *Electrochim. Acta* **2014**, *123*, 205−210.
98. Adak, O.; Kladnik, G.; Bavdek, G.; Cossaro, A.; Morgante, A.; Cvetko, D.; Venkataraman, L. *Nano Lett.* **2015**, *15*, 8316−8321.
99. Cao, Y.; Dong, S.; Liu, S.; Liu, Z.; Guo, X. *Angew. Chem., Int. Ed.* **2013**, *52*, 3906−3910.
100. Jia, C.; Guo, X. *Chem. Soc. Rev.* **2013**, *42*, 5642-60.
101. Hybertsen, M. S.; Venkataraman, L.; Klare, J. E.; Whalley, A. C.; Steigerwald, M. L.; Nuckolls, C. *J. Phys.: Condens. Matter* **2008**, *20*, 374115.
102. Kim, Y.; Hellmuth, T. J.; Bürkle, M.; Pauly, F.; Scheer, E. *ACS Nano* **2011**, *5*,

4104−4111.
103. Lee, S. H.; Lin, W. C.; Kuo, C. H.; Karakachian, M.; Lin, Y. C.; Yu, B. Y.; Shyue, J. J. *J. Phys. Chem. C* **2010**, *114*, 10512−10519.
104. Venkataraman, L.; Klare, J. E.; Tam, I. W.; Nuckolls, C.; Hybertsen, M. S.; Steigerwald, M. L. *Nano Lett.* **2006**, *6*, 458−462.
105. Zhang, Q.; Liu, L.; Tao, S.; Wang, C.; Zhao, C.; Gonzalez, C.;´ Dappe, Y. J.; Nichols, R. J.; Yang, L. *Nano Lett.* **2016**, *16*, 6534−6540.
106. Quek, S. Y.; Choi, H. J.; Louie, S. G.; Neaton, J. B. *Nano Lett.* **2009**, *9*, 3949−3953.
107. Kiguchi, M.; Miura, S.; Hara, K.; Sawamura, M.; Murakoshi, K. *Appl. Phys. Lett.* **2006**, *89*, 213104.
108. Kamenetska, M.; Koentopp, M.; Whalley, A. C.; Park, Y. S.; Steigerwald, M. L.; Nuckolls, C.; Hybertsen, M. S.; Venkataraman, L. *Phys. Rev. Lett.* **2009**, *102*, 126803.
109. Yokota, K.; Taniguchi, M.; Tsutsui, M.; Kawai, T. *J. Am. Chem. Soc.* **2010**, *132*, 17364−17365.
110. Jasper-Tönnies, T.; Garcia-Lekue, A.; Frederiksen, T.; Ulrich, S.; Herges, R.; Berndt, R. *Phys. Rev. Lett.* **2017**, *119*, 066801.
111. Smogunov, A.; Dappe, Y. J. *Nano Lett.* **2015**, *15*, 3552−3556.
112. Picaud, F.; Smogunov, A.; Corso, A. D.; Tosatti, E. *J. Phys.: Condens. Matter* **2003**, *15*, 3731-3740.
113. Wang, M.; Wang, Y.; Sanvito, S.; Hou, S. *J. Chem. Phys.* **2017**, *147*, 054702.
114. Tomfohr, J. K.; Sankey, O. F. *Phys. Rev. B: Condens. Matter Mater. Phys.* **2002**, *65*, 245105.
115. Wang, G.; Kim, T.-W.; Jo, G.; Lee, T. *J. Am. Chem. Soc.* **2009**, *131*, 5980−5985.
116. Mativetsky, J. M.; Palma, M.; Samorì, P. *Top. Curr. Chem.* **2008**, *285*, 157−202.
117. Xu, B.; Xiao, X.; Tao, N. J. *J. Am. Chem. Soc.* **2003**, *125*, 16164−16165.
118. Huang; Xu; Chen; Di Ventra, M.; Tao. *Nano Lett.* **2006**, *6*, 1240−1244.
119. Haiss, W.; Nichols, R. J.; van Zalinge, H.; Higgins, S. J.; Bethell, D.; Schiffrin, D. J. *Phys. Chem. Chem. Phys.* **2004**, *6*, 4330−4337.
120. Haiss, W.; Martín, S.; Leary, E.; van Zalinge, H.; Higgins, S. J.; Bouffier, L.; Nichols, R. J. *J. Phys. Chem. C* **2009**, *113*, 5823−5833.
121. Li, C.; Pobelov, I.; Wandlowski, T.; Bagrets, A.; Arnold, A.; Evers, F. *J. Am. Chem. Soc.* **2008**, *130*, 318−326.
122. Kelley, T. W.; Granstrom, E.; Frisbie, C. D. *Adv. Mater.* **1999**, *11*, 261−264.
123. Nakazumi, T.; Kaneko, S.; Kiguchi, M. *J. Phys. Chem. C* **2014**, *118*, 7489−7493.
124. Castellanos-Gomez, A.; Bilan, S.; Zotti, L. A.; Arroyo, C. R.; Agraït, N.; Cuevas, J. C.; Rubio-Bollinger, G. *Appl. Phys. Lett.* **2011**, *99*, 123105.
125. Zhang, Q.; Tao, S.; Yi, R.; He, C.; Zhao, C.; Su, W.; Smogunov, A.; Dappe, Y. J.; Nichols, R. J.; Yang, L. J. Phys. Chem. Lett. 2017, 8, 5987−5992.
126. Venkataraman, L.; Klare, J. E.; Nuckolls, C.; Hybertsen, M. S.; Steigerwald, M. L. *Nature* **2006**, *442*, 904−907.
127. Engelkes, V. B.; Beebe, J. M.; Frisbie, C. D. *J. Phys. Chem. B* **2005**, *109*, 16801−16810.
128. Kim, C. M.; Bechhoefer, J. *J. Chem. Phys.* **2013**, *138*, 014707.
129. Ratner, M. A.; Davis, B.; Kemp, M.; Mujica, V.; Roitberg, A.; Yaliraki, S. *Ann.*

N.Y. Acad. Sci. **1998**, *852*, 22−37.
130. Engelkes, V. B.; Beebe, J. M.; Frisbie, C. D. *J. Am. Chem. Soc.* **2004**, *126*, 14287−14296.
131. Sabater, C.; Untiedt, C.; Palacios, J. J.; Caturla, M. J. *Phys. Rev. Lett.* **2012**, *108*, 205502.
132. Beebe, J. M.; Engelkes, V. B.; Miller, L. L.; Frisbie, C. D. *J. Am. Chem. Soc.* **2002**, *124*, 11268−11269.
133. Liang, S.-J.; Ang, L. K. *Phys. Rev. Appl.* **2015**, *3*, 014002.
134. Sachtler, W. M. H.; Dorgelo, G. J. H.; Holscher, A. A. *Surf. Sci.* **1966**, *5*, 221−229.
135. Guo, X.; Small, J. P.; Klare, J. E.; Wang, Y.; Purewal, M. S.; Tam, I. W.; Hong, B. H.; Caldwell, R.; Huang, L.; O'Brien, S.; Yan, J.; Breslow, R.; Wind, S. J.; Hone, J.; Kim, P.; Nuckolls, C. *Science* **2006**, *311*, 356-359.
136. Frisenda R.; Perrin M L.; Valkenier H.; Hummelen J C.; van der Zant H S J. *J. Phys. Status Solidi B*, **2013**, *250*, 2431–6.
137. Haiss, W.; Wang, C.; Grace, I.; Batsanov, A. S.; Schiffrin, D. J.; Higgins, S. J.; Bryce, M. R.; Lambert, C. J.; Nichols, R. J. *Nat. Mater.* **2006**, *5*, 995.
138. Wang C.; Batsanov A S.; Bryce M R.; Martín S.; Nichols R J.; Higgins S J.; García-Suárez V M.; Lambert C J. *J. Am. Chem. Soc.* **2009**, *131,* 15647–54
139. Halbritter A.; Makk P.; Mackowiak S.; Csonka S.; Wawrzyniak M.; Martinek J. *Phys. Rev. Lett.* **2010**, *105*, 266805.
140. Zhou X S.; Chen Z B.; Liu S H.; Jin S.; Liu L.; Zhang H M.; Xie Z X.; Jiang Y B.; Mao B W. *J. Phys. Chem. C* **2008**, *112*, 3935–40.
141. Xia J L.; Diez-Perez I.; Tao N J.; *Nano Lett.* **2008**, *8*, 1960–4.
142. Fujihira M.; Suzuki M.; Fujii S.; Nishikawa A. *Phys. Chem. Chem. Phys.* **2006**, *8*, 3876–84.
143. Inkpen, M. S.; Liu, Z. F.; Li, H.; Campos, L. M.; Neaton, J. B.; Venkataraman, L. *Nat. Chem.* **2019**, *11*, 351-358.

9 Appendix

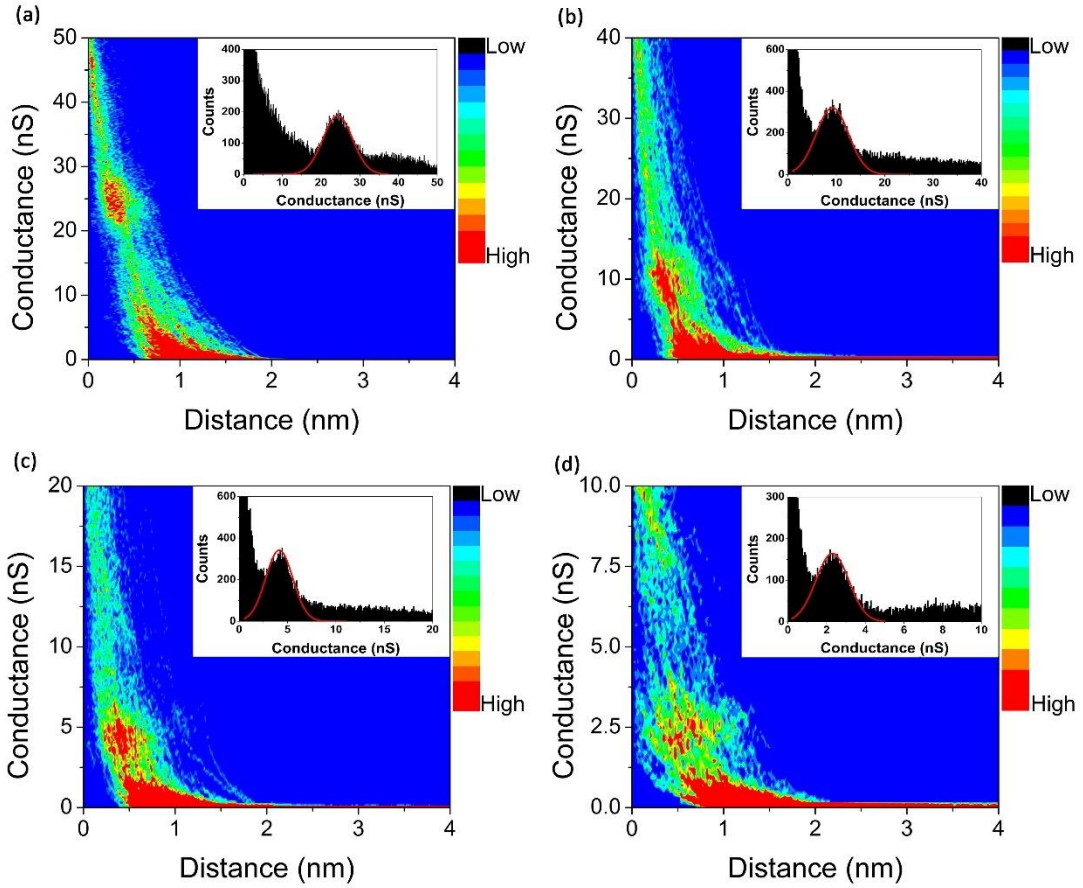

Figure A1. (a)-(d) 2D histograms of single molecule conductance of gold-N-alkanedithiolgraphene hybrid junctions which N=6, 8, 10, 12 respectively and the corresponding 1D conductance histograms with the Gaussian fit in inset.

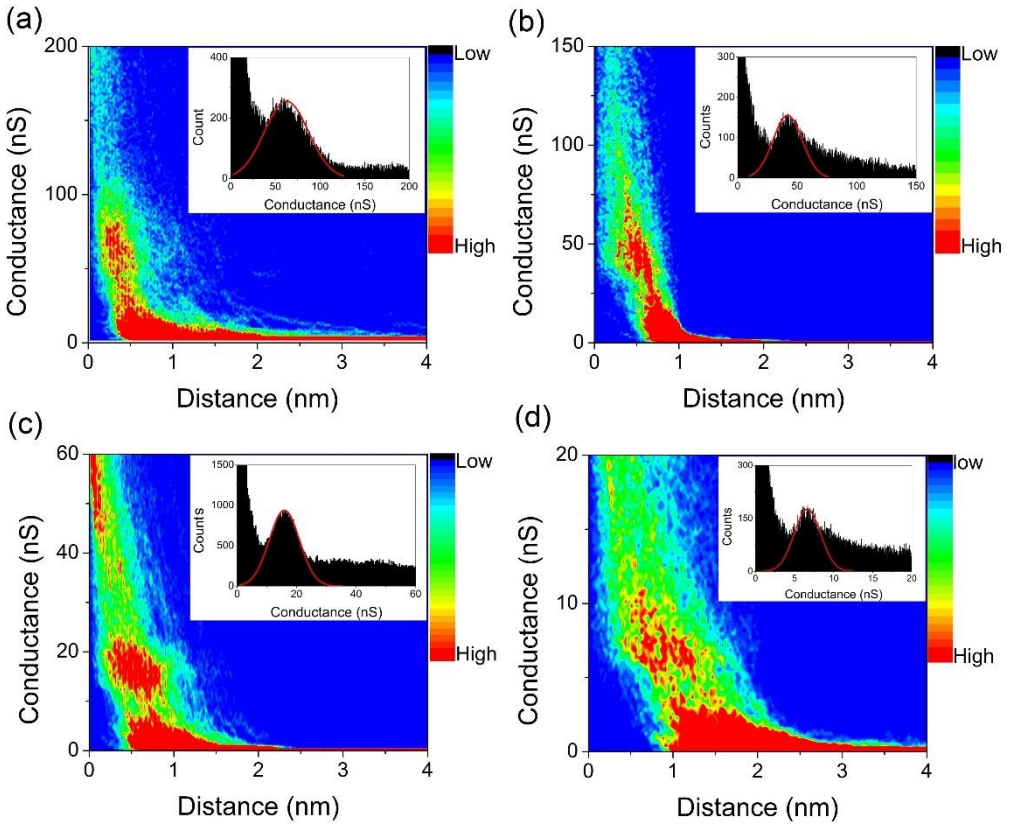

Figure A2. (a)-(d) 2D histograms of single molecule conductance of gold-*N*-alkanediamine-graphene hybrid junctions which *N*=4, 6, 8, 10 respectively and the corresponding 1D conductance histograms with the Gaussian fit in inset.

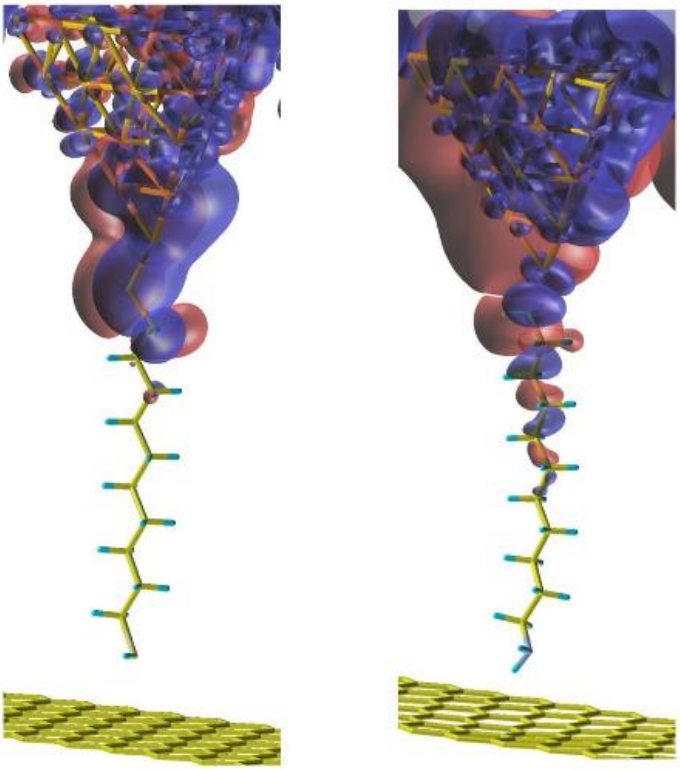

Figure A3. Isoelectronic density of states at the Fermi energy for (left) the alkanedithiol and (right) the alkanediamine gold-graphene junction.

MATLAB analysis code

```
% Fast and straightforward analysis approach of charge transport data in single molecule junctions%
% Tested on MATLAB R2016b%
% Refer DOI: 10.1088/1361-6528/aac45a%
% Authors: Zhang,Q.; Liu, C.; Tao, S.; Yi, R.; Su, W.;Zhao, C.; Zhao, C.;
% Dappe, Y.;Nichols, R. J.; Yang, L.%



clear
close all

tic

FileList = dir('*.txt');
N = size(FileList,1);

VariAverFilter_x = 1;
VariAverFilter_y = 1;

%%%%%%%%%%%%%%%%%%%%%%%%%%%%%%%%%%%%%%%%%%%%%%%%%%%%%%%%%%%%%%%%%%%%%%%%%%%%%%%%%%%%%%%
%set parameters

fdistance=2.0; %X-Filter
xaver=0.1;
xvari=0.1;

yaver=3.5; %Y-Filter(ydistance=2/3 of the maxium current)
yvari=10;

peaknumber=3; %Peak filter

step=19; %for bin sets

%%%%%%%%%%%%%%%%%%%%%%%%%%%%%%%%%%%%%%%%%%%%%%%%%%%%%%%%%%%%%%%%%%%%%%%%%%%%%%%%%%%%%%%

Save_Cluster=zeros(N,2);
Save_name=cell(N,1);
Save_Cluster_count=0;

for m1 = 1:N
```

```

filename = FileList(m1).name;
disp(filename);
ImperialFile = fopen(filename);

Data = textscan(ImperialFile, '%f%f %*[^\n]', 'HeaderLines', 1,'delimiter', '\t');
fclose(ImperialFile);
U = cell2mat(Data);
U(:,2) = 1.0e1 * U(:,2);

U_size=size(U,1);

data_max=max(U(:,2));
data_min=min(U(:,2));

[pks,locs,widths,proms] = findpeaks(U(:,2));

peaks_flag=0;

for n=1:length(proms)
    if proms(n) >= (data_max*1/10)
        peaks_flag=peaks_flag + 1;
    end
end

if peaks_flag <= peaknumber && peaks_flag >= 0

%%%%%%%%%%%%%%%%%%%%%%%%%%%%%%%%%%%%%%%%%%%%%%%%%%%%%%%%%%%%%%%%%%%%%%%%%%%%%%%%%%%%%%%
    if VariAverFilter_x == 1 && VariAverFilter_y == 1

        xxflag=0;
        yyflag=0;

        xx_filterx=zeros(U_size,1);
        x_filtery=zeros(U_size,1);
        y_filtery=zeros(U_size,1);

        xx_filtery=1;
        yy_filtery=1000;
```

```
80
81 -        for i = 1 : U_size
82 -            if U(i,1) <= fdistance
83 -                xx_filterx(i) = U(i,2);
84 -            else
85 -                xx_filterx(i) = [];
86 -            end
87 -            if data_max*2/3 <= U(i,2)
88 -                x_filtery(i) = U(i,1);
89 -                y_filtery(i) = U(i,2);
90
91 -            end
92 -        end
93
94
95 -        xx_filtery = x_filtery(x_filtery~=0); %REMOVE 0 MAIRIX FOR FURTHER MEAN AND VAR FILTER
96 -        yy_filtery = y_filtery(y_filtery~=0);
97
98
99 -        if var(xx_filterx)<xvari && mean(xx_filterx)<xaver
100 -              xxflag=1;
101 -          end
102
103 -          if mean(xx_filtery) > yaver && var (yy_filtery) < yvari
104 -                yyflag=1;
105 -          end
106
107 -      end
108
109 -      if xxflag==1 && yyflag==1
110
111   %%%%
```

```
158
159 -   Temp_cluster=[counts_max_values counts_max];
160 -   Save_Cluster_count=Save_Cluster_count+1;
161 -   Save_Cluster(Save_Cluster_count,:)=Temp_cluster;
162 -   Save_name{Save_Cluster_count}=filename;
163
164 -       end
165 -   end
166
167 -   clear filename Data U ImperialFile %pks locs widths proms % xx_filterx x_filtery y_filtery
168     %clearvars -except FileList faver fvari Save_Cluster Save_name Save_Cluster_count step
169
170     % VariAverFilter_x = 1;
171     % VariAverFilter_y = 1;
172     %
173     % fdistance = 2;
174     % xx_filtery = 1;
175     % yy_filtery = 1000;
176
177 -   end
178
179 -   Save_Cluster(Save_Cluster(:,2) == 0,:)=[];
180 -   Save_name(cellfun(@isempty,Save_name))=[];
181
182 -   figure;
183 -   plot(Save_Cluster(:,1),Save_Cluster(:,2),'.','MarkerSize',8);
184 -   xlabel('plateau mean value (nA) ');
185 -   ylabel('plateau counts');
186 -   xlim([0 6]);
187
188
189     %%%%%%%%%%%%%%%%%%%%%%%%%%%%%%%%%%%%%%%%%%%%%%%%%%%%%%%%%%%%%%%%%%%%%%%%%%%%%%%
190
191
192 -   X = Save_Cluster;
193
194 -   rng(1); % For reproducibility
195 -   [idx,C] = kmeans(X(:,2),3);
196
197     %%%%%%%%%%%%%%%%%%%%%%%%%%%%%%%%%%%%%%%%%%%%%%%%%%%%%%%%%%%%%%%%%%%%%%%%%%%%%%%
198
199 -   figure;
200 -   hold on;
201 -   plot(X(find(idx==1),1),X(find(idx==1),2),'.r','MarkerSize',10);
202 -   plot(X(find(idx==2),1),X(find(idx==2),2),'.b','MarkerSize',10);
203 -   plot(X(find(idx==3),1),X(find(idx==3),2),'.g','MarkerSize',10);
204 -   xlabel('plateau mean value (nA) ');
205 -   ylabel('plateau counts');
206 -   legend('Region 1','Region 2','Region 3');
207 -   xlim([0 6]);
208 -   hold off;
209
210
211
212     %%%%%%%%%%%%%%%%%%%%%%%%%%%%%%%%%%%%%%%%%%%%%%%%%%%%%%%%%%%%%%%%%%%%%%%%%%%%%%%
213
214 -   [selected_MAX_value,selected_MAX_location]=max(X(:,2));
215 -   selected_counts_group=idx(selected_MAX_location);
216
217 -   index=0;
218 -   Save_Cluster_Seclected=[];
219 -   Save_name_selected={};
220 -   for n=1:length(Save_Cluster(:,1))
221 -       index=index+1;
222 -       if idx(n)==selected_counts_group
223 -           Save_Cluster_Seclected=[Save_Cluster_Seclected;Save_Cluster(n,:)];
224 -           Save_name_selected=[Save_name_selected;Save_name{n}];
225 -       end
226 -   end
227
228
229
230     %%%%%%%%%%%%%%%%%%%%%%%%%%%%%%%%%%%%%%%%%%%%%%%%%%%%%%%%%%%%%%%%%%%%%%%%%%%%%%%
231
232 -   X = Save_Cluster_Seclected;
233 -   rng default;  % For reproducibility
234 -   idx = clusterdata(X(:,1),'linkage','ward','savememory','on','maxclust',5);
235
```

```
figure;
hold on;
plot(X(find(idx==1),1),X(find(idx==1),2),'.k','MarkerSize',10);
plot(X(find(idx==2),1),X(find(idx==2),2),'.b','MarkerSize',10);
plot(X(find(idx==3),1),X(find(idx==3),2),'.g','MarkerSize',10);
plot(X(find(idx==4),1),X(find(idx==4),2),'.r','MarkerSize',10);
plot(X(find(idx==5),1),X(find(idx==5),2),'.c','MarkerSize',10);
xlabel('plateau mean value (nA) ');
ylabel('plateau counts');
legend('Region 1','Region 2','Region 3','Region 4','Region 5');
xlim([0 6]);
hold off;

%scatter(X(:,1),X(:,2),100,idx,'filled')  %%%

%%%%%%%%%%%%%%%%%%%%%%%%%%%%%%%%%%%%%%%%%%%%%%%%%%%%%%%%%%%%%%%%%%%%%%%%%%%%%%%

for no_group=1:max(idx)
    group_counts_sum(no_group)=0;
for no=1:length(idx)
    if idx(no) == no_group
    group_counts_sum(no_group)=group_counts_sum(no_group)+Save_Cluster_Seclected(no,2);
    end
end
end

[selected_MAX_counts_value,selected_MAX_counts_location]=max(group_counts_sum);


%%%%%%%%%%%%%%%%%%%%%%%%%%%%%%%%%%%%%%%%%%%%%%%%%%%%%%%%%%%%%%%%%%%%%%%%%%%%%%%

U_save = [];
Save_name_selected_zip={};
for n=1:length(idx)

    if idx(n) == selected_MAX_counts_location
        filename = Save_name_selected{n};
        disp(filename);
        ImperialFile = fopen(filename);

        Data = textscan(ImperialFile, '%f%f %*[^\n]', 'HeaderLines', 1,'delimiter', '\t');
        fclose(ImperialFile);
        U = cell2mat(Data);
        U(:,2) = 1.0e1 * U(:,2);
        U_save=[U_save;U];

        Save_name_selected_zip=[Save_name_selected_zip;Save_name_selected{n}];

        clear filename ImperialFile Data
    end

end

zip('selected.zip',Save_name_selected_zip);

%%%%%%%%%%%%%%%%%%%%%%%%%%%%%%%%%%%%%%%%%%%%%%%%%%%%%%%%%%%%%%%%%%%%%%%%%%%%%%%

rangemax=max(U_save(:,2))
rangemin=min(U_save(:,2))

[totalbincounts,xyaxis] = histcounts(U_save(:,2),501);

figure;
%xyaxis=xyaxis/0.3;
bar(xyaxis(1:length(xyaxis)-1),totalbincounts)
axis([0 10 0 1500]);
title('Our Script Result');
ylabel('Counts');
xlabel('Current(nA)');%will be conductance if divide by the bias

%%%%%%%%%%%%%%%%%%%%%%%%%%%%%%%%%%%%%%%%%%%%%%%%%%%%%%%%%%%%%%%%%%%%%%%%%%%%%%%

toc
```

I(*s*) curve plot code

```
%% ACKNOWLEDGMENTS:
%%This IS plot code was modified on the data analysis code%%
%%by Mario Lemmer on the NC paper DOI: 10.1038/ncomms12922%%
%%We thank Mario Lemmer for supplying the original code%%

%% Get files to import

clear
close all
FileList_All_Files = dir('*.txt');                    % Get all the .txt files in the current folder
M = size(FileList_All_Files,1);                       % N is the number if I(s) traces in the folder
Alle_Daten = cell(M,3);                               % Preallocate cell array
Alle_Daten(:,1) = {FileList_All_Files.name}';         % Write all filenames in Alle_Daten


%% Define Parameters

nAaxis = 10; %the current, which is the y axis

d = 4; %the distance, which is the x axis

farbe_plot = [0 0 1];              % Color for I(s) trace


%% Loop imports data into "Alle_Daten" and writes new .txt files without header if needed

for m = 1:M;

    tmp_filename_import = Alle_Daten{m,1};            % get the file name of the mth file
    disp(tmp_filename_import);                        % Display filename

    % Extract Parameters and Data
    ImperialFile = fopen(tmp_filename_import);                                          % Open current file and
    setpoint = {10};                          % 2. Parameter for Parameter file is the setpoint current ('%*s' = ski
    voltage = {0.3};                                                    % 3. Parameter for Parameter file is t
    tmp_dat_mat = cell2mat(textscan(ImperialFile, '%f%f %*[^\n]', 'HeaderLines', 1));     % Data included the distance
    fclose(ImperialFile);                                                               % Closes the filehandle

    Alle_Daten(m,2) = {tmp_dat_mat};                                                    % Write distance and cur
    Alle_Daten(m,3) = {cat(2,setpoint, voltage)};

end;


%% Generate DAT.mat file that contains only the first distance vector and all current vectors (for faster

Alle_Daten = Alle_Daten';                                 % Save Alle_Daten rather as a coumn for each I(s) trace
%Alle_Daten_Mat = [Alle_Daten{2,:}];                       % Take on I and s matrices from every I(s) trace
%DAI = cat(2,Alle_Daten_Mat(:,1),Alle_Daten_Mat(:,2 : 2 : end)); % Creat DAI matrix by taking first column (Distance) an
%N = size(DAI,1);                                          % N is the number of data points per trace


%% Create Variables needed for plotting

FileList_Mat = [Alle_Daten{2,:}];                 % Save all I(s) data in "FileList_Mat"
s = FileList_Mat(:,1);                % Save the first distance vector (Should be all the same) in mm as "s"
voltage = Alle_Daten{3,1}{1,2};                   % Extract the bias voltage of the first trace
setpoint = Alle_Daten{3,1}{1,1};                  % Extract the setpoint current of the first trace
I_sign = (voltage/abs(voltage));          % Check for the sign of the tunneling current
I = 10*(I_sign)*FileList_Mat(:,2 : 2 : end);       % Save all current vectors in matrix "I"
[N, M] = size(I);                                 % M is the number of Files, N is the number of Datapoints per trace
DAI = cat(2,s,I);                                 % Save one distance vector and all current vectors in "DAI"


%% Plot I(s)

mkdir('ISplot');                      % Make the folder
cd ('ISplot')                         % Enter folder


message_1 = sprintf('FileList contains %i files.',M);       % Create message of how many I(s) traces are in FileList
disp(message_1)                                             % Display  message of how many I(s) traces are in FileList
first_plot = input('First file to be plotted? ');
last_plot = input('Last file to be plotted? ');
how_many = last_plot-first_plot+1;
```

```
77 -  for i = first_plot:last_plot  % Plot the specified number of I(s) traces
78
79        % Display progress
80 -      percent_done = 100*(i-first_plot+1)/(last_plot-first_plot+1);
81 -      message_2 = sprintf('Currently plotting graph %i of %i (%0.1f %%)',i-first_plot+1,how_many,percent_done);    % Creat
82 -      disp(message_2)                                                                                              % Display what perce
83
84        % Plot and Style
85 -      fh = figure('Visible','off');                        % Create invisible figure, so there aren't 100 windows popping u
86 -      plot(s,I(:,i),'Color',farbe_plot,'LineWidth',1);     % Plot the I(s) trace in the color specified before
87 -       hBar = findobj(gca,'Type','patch');
88 -          set(hBar,'FaceColor',[0.4 0.4 0.4],'EdgeColor',[0.4 0.4 0.4]);
89
90            % set axis limits
91 -          axis([0 d -1 nAaxis]);
92
93 -          xAxis = get(gca, 'xlim');
94 -          yAxis = get(gca, 'ylim');
95 -          numXtick = ceil(xAxis(2)/6);
96 -          numYtick = ceil(yAxis(2)/6);
97 -          set(gca,'XTick',xAxis(1):numXtick:xAxis(2), 'FontSize', 34, 'TickDir', 'out');
98 -          set(gca,'YTick',yAxis(1):numYtick:yAxis(2), 'FontSize', 34, 'TickDir', 'out');
99
100           %set and reposition xlabel and ylabel
101 -         xl = xlabel('Distance /nm', 'FontSize', 44);
102 -         set(xl, 'Units', 'Normalized');
103 -         posxl = get(xl, 'Position');
104 -         set(xl, 'Position', [0.5, -0.11, 0]);
105
106 -         yl = ylabel('Current /nA', 'FontSize', 44);
107 -         set(yl, 'Units', 'Normalized');
108 -         posyl = get(yl, 'Position');
109 -         set(yl, 'Position', [-0.11, 0.5, 0]);
110
111           %set(gca,'OuterPosition',[left bottom width height])
112 -         set(gca,'OuterPosition',[0.08 0.08 0.90 0.90])
```

```
113
114 -         set(gcf,'PaperUnits','centimeters');
115 -         set(gcf,'PaperPosition',[0 0 40 30]);
116
117 -         pic_str = strcat(Alle_Daten{1,i}(1:end-4),'.tif');     % Create a string for the savename
118 -         saveas(fh, pic_str, 'tif');                            % Save .tif under the savename
119 -         end;
120
121 -   close all
122 -   fclose all;
123 -   cd ..
```

Publications and patent

1. **Zhang, Q.**; Liu, L.; Tao, S.; Wang, C.; Zhao, C.; González, C.; Dappe, Y. J.; Nichols, R. J.; Yang, L. *Nano Lett.* **2016**, *16*, 6534-6540.

2. **Zhang, Q.**; Tao, S.; Yi, R.; He, C.; Zhao, C.; Su, W.; Smogunov, A.; Dappe, Y. J.; Nichols, R. J.; Yang, L. *J. Phys. Chem. Lett.* **2017**, *8*, 5987−5992.

3. **Zhang, Q.**; Liu, C.; Tao, S.; Yi, R.; Su, W.; Zhao, C.; Zhao, C.; Dappe, Y. J.; Nichols, R. J.; Yang, L. *Nanotechnology* **2018**, *29*, 325701.

4. **Zhang, Q.**; Tao, S.; Fan, Y.; Zhao, C.; Zhao, C.; Su, W.; Dappe, Y. J.; Nichols, R. J.; Yang, L. *J. Phys. Chem. C* **2018**, *122*, 23200–23207.

5. Tao, S.; **Zhang, Q.;** He, C.; Lin, X.; Xie, R.; Zhao, C.; Zhao, C.; Smogunov, A.; Dappe, Y. J.; Nichols, R. J.; Yang, L. *ACS Applied Nano Materials* **2019**, *2*, 12-18.

6. He, C.; **Zhang, Q.**; Tao, S.; Zhao, C.; Zhao, C.; Dappe, Y. J.; Nichols, R. J.; Yang, L. *Phys. Chem. Chem. Phys*., **2018**, *20*, 24553-24560

7. Liu, L.; **Zhang, Q.**; Tao, S.; Zhao, C.; Almutib, E.; Al-Galiby, Q.; Bailey, S. W. D.; Grace, I.; Lambert, C. J.; Du, J.; Yang, L. *Nanoscale* **2016**, *8*, 14507.

8. Yi, R.; Liu, C.; Zhao, Y.; Hardwick, L. J.; Li, Y.; Geng, X.; **Zhang, Q.**; Yang, L.; Zhao, C. *Electrochimica Acta* **2019**, *299*, 479-488.

9. Wu, J.; Zhao, Y.; Zhao, C. Z.; Yang, L.; Lu, Q.; **Zhang, Q**.; Smith, J.; Zhao, Y. *Materials* **2016**, *9*, 695.

10. Lu, Q.; Mu, Y.; Roberts, J. W.; Althobaiti, M.; Dhanak, V. R.; Wu, J.; Zhao, C.; Zhao, C. Z.; **Zhang, Q.**; Yang, L.; Mitrovic, I. Z.; Taylor, S.; Chalker, P. R. *Materials* **2015**, *8*, 8169-8182.

11. Graphene as a novel electrode for single molecule conductance measurement. Patent Number: CN201610145493.7.